University of Genoa

PhD program in Nanochemistry

Science and technology of graphene-based inks for polymer-composite applications

By
Silvia Gentiluomo

Supervisors:

Dr Francesco Bonaccorso

Dr. Vittorio Pellegrini

Prof. Daniele Marrè

Advisor:

Dr. Esau Antonio Del Rio Castillo

Acknowledgements

This period of my life as a PhD student was extremely useful to grow both professionally and personally.

Firstly, I am grateful to my supervisor, Dr. Francesco Bonaccorso, thanks to his patience and guide, I gained a lot of knowledge on a topic that I am really love.

I am grateful to Dr. Vittorio Pellegrini for giving me full access to the research facilities at Graphene Labs “Istituto Italiano di Tecnologia” that allowed me for carrying out this research work.

I would like to express my gratitude to Prof. Daniele Marrè, my academic Co-supervisor at Department of Physics “University of Genova”.

I would like to thank Dr. Peter S. Toth for his guidance during the first year and Dr. Sanjay Thorat for his continuous support during my research activities. A special thanks to Dr. Esau Antonio Del Rio Castillo for his patience and his support during the writing of the thesis, I could not made it without him.

My sincere thanks also to Dr. Costas Galiotis for his ospitality during my collaboration in the FORTH institute in Patras. I want to thank also Panagiotis Pappas and Giovanna Carbone for their guidance during my activities in Patras and Christos Kostaras and Fabrizia Cilento for their friendship and support.

I am grateful to have worked with marvellous people, like the technicians Elisa Mantero, Luigi Marasco, Manuel Crugliano and Luca Gagliani, and to learn from the wisdom and knowledge of our postdocs.

I thank all the people that have supported me during these three years, my beloved friends Lucia Dimola and Ana Tanevska. And also I thank all my friends from Torino, so far away and yet so near me.

Last but not the least, I am grateful for the support my parents and my brother gave me and for giving me the right reason to choose to be a scientist, contribute to create a better world for my niece Viola to grow in.

List of abbreviations

$\dot{\gamma}$: shear rate

μ : steady coefficient of friction

A: surface area of the flakes

Ab: Absorbance

ABS: acrylonitrile-butadiene-styrene

AFM : atomic force microscopy

AR : aspect ratio

C : concentration

CM: compression moulding

CMC: sodium carboxymethyl cellulose

CNTs : carbon nanotubes

CTAB: cetyltrimethylammonium bromide

Cu: copper

CVD: chemical vapour deposition

D : diameter of the channel inside the pressure homogenizers

d : scratch depth in wear testing

DMSO: dimethylsulfoxide

ECGQD: edge carboxylated graphene quantum dots

EVA: ethylene vinyl acetate

F : the applied load

f: friction coefficient between the solvent

F_b: buoyant force

F_c : centrifugal force

FDM: fused deposition modelling

F_f : frictional force

FLG: few-layer graphene

$FLG\text{-}PMMA_{US}$: few-layer graphene dispersion produced in acetone-PMMA through ultrasonication

FLG_{US} : few-layer graphene dispersion produced in acetone through ultrasonication

FLG_{WJM} : few-layer graphene dispersion produced in NMP through wet jet milling

FLG_{WJM} : few-layer graphene flakes produced through wet jet milling

FoM: figures of merit

FWHM(G) : full width half maximum of the G peak (Raman spectroscopy)

GBL: γ-butyrolactone

G_c : gravitational constant

GnPs: graphene nanoplatelets

HDPE: high density polyethylene

I(D)/I(G): intensity of the D peak over the intensity of the G peak (Raman spectroscopy)

IM: injection moulding

IPA: isopropanol

K: wear rate

K_σ : stress constant

l : light path length

LLPE : linear low-density polyethene

L_m : total scanned length in wear and friction testing

LPE: liquid phase exfoliation

M : torque

MC: micromechanical cleavage

M_{final} : mass of the filter is measured after the vacuum filtration of the exfoliated graphite dispersion

m_{FLG} : exfoliated graphite mass

$M_{initial}$: mass of the filter is measured before the vacuum filtration of the exfoliated graphite dispersion

MLG : multi-layer graphene

m_p : mass of the particle

m_s : mass of the displaced solvent

$m_{tot(FLG-PMMAus)}$: mass of the FLG-$PMMA_{US}$ sample after the isothermal ramp during TGA analysis

N : the number of cycles

Ni: nickel

NMP: N-methyl-2-pyrrolidone

OAS: optical absorption spectroscopy

ODMS : octadecyltrimethoxysilane

OP: oxygen permeability

OTR : oxygen transmission rate

P: pressure

PA12: polyamide 12

PA66: nylon 6,6

PBT: polybutylene terephthalate

PC: polycarbonate

P_e : the partial oxygen pressure of the external environment

PE: polyethylene

PEEK: poly (ether ether ketone)

Pi : the partial oxygen pressure of the oxygen‑free room

PLA: polylactic acid

PMMA: poly methyl methacrylate

PMMA: poly methyl methacrylate

PP: polypropylene

PS: polystyrene

PTFE: polytetrafluoroethylene

PU: polyurethane

PVA: polyvinyl alcohol

r : distance from the rotational axes

R_0 : radius of curvature at the drop apex

R_h: Hansen radius

r_{ball} : radius of the rubbing ball in wear testing

Re: Reynolds number

r_{FLG}: residue of the dispersion FLG_{US} at 800 °C after TGA

$r_{FLG\text{-}PMMAus}$: residue of the dispersion $FLG‑PMMA_{US}$ at 800 °C after TGA

rpm : rate per minute

SB: styrene-butadiene copolymer

SBS : sedimentation based separation

SC: sodium cholate

SDBS: sodium dodecylbenzene sulfonate

S-g-A: poly(styrene sulfonic acid-graft-polyaniline)

Si: silicon

SiC: silicon carbide

SLA: stereolithography

SLG: single-layer graphene

SLS: selective laser sintering

t : thickness of the flakes

T: temperature

t_{1gram} : time to produce 1 gram of graphene

T_b : boiling point

TC: thermal conductivity

TEM: Transmission electron microscopy

t_f : the thickness of the sample

TGA : thermogravimetric analysis

TPU: thermoplastic polyurethane

u : mean velocity of the fluid

v : sedimentation velocity of the particle itself

V_{1gram} : volume to produce of 1 gram of graphene

V_{FLG} : volume of the exfoliated graphite dispersion

V_{mix} : volume of solvent

WJM: wet jet milling

Y_w : exfoliation yield by weight

α : the extinction coefficient

β : shape factor

γ : surface tension

γ_E : surface energy

δ_D: Hansen parameter dispersive forces component

δ_G : square root of the surface energy of graphene

ΔG_{mix}: Gibbs free energy of mixing

δ_H: Hansen parameter hydrogen bonds component

ΔH_{mix}: Enthalpy of mixing

δ_P: Hansen parameter polar bonds component

δ_S : square root of the surface energy of the solvent

ΔS_{mix} : entropy of mixing

δT : Hildebrand parameter

η : viscosity of the solvent

η_s : the viscosity

ρ : density of the solvent

ρ_p : density of the particle

ρ_s : density of the solvent

σ: electrical conductivity

σ_S : stress

Φ : graphene volume fraction

ω : angular velocity

List of publications and contributions

Original publications on ISI Journals:

1) E. Petroni, E. Lago, S. Bellani, D. W. Boukhvalov, A. Politano, B. Gürbulak, S. Duman, M. Prato, **S. Gentiluomo**, R. Oropesa-Nuñez, J.-K. Panda, P. S. Toth, A. E. Del Rio Castillo, V. Pellegrini, F. Bonaccorso, "Liquid-Phase Exfoliated Indium–Selenide Flakes and Their Application in Hydrogen Evolution Reaction", **Small 14 (2018) 1800749**

2) A. E. Del Rio Castillo, V. Pellegrini, A. Ansaldo, F. Ricciardella, H. Sun, L. Marasco, J. Buha, Z. Dang, L. Gagliani, E. Lago, N. Curreli, **S. Gentiluomo**, F. Palazon, M. Prato, R. Oropesa-Nuñez, P. S. Toth, E. Mantero, M. Crugliano, A. Gamucci, A. Tomadin, M. Polini and F. Bonaccorso, "High-yield production of 2D crystals by wet-jet milling", **Materials Horizons 5 (2018) 890**

3) E. Lago, Peter S. Toth, **S. Gentiluomo**, S. B. Thorat, V. Pellegrini, and F. Bonaccorso, "Enhanced polycarbonate mechanical performances by the addition of few-layers boron nitride with tuneable morphology", **submitted**

4) E. Lago, F. Bonaccorso, **S. Gentiluomo**, A. E. Del Rio Castillo, N. M. Pugno, R. Cingolani, P. S. Toth, and V. Pellegrini, "Exploiting the ideal properties of two-dimensional fillers for the mechanical reinforcement of polymer nanocomposites", **submitted**

5) **S. Gentiluomo**, S. B. Thorat, E. A. Del Rio Castillo, P. S. Toth, J. K. Panda, U. C. Paul, A. Athanassiou, V. Pellegrini, and F. Bonaccorso, "Poly methyl methacrylate assisted exfoliation of graphite and its use in acrylonitrile-butadiene-styrene composites", **submitted**

Communications at Conferences

Oral communications:

1. **S. Gentiluomo**, S. B. Thorat, E. A. Del Rio Castillo, V. Pellegrini, and F. Bonaccorso, "Poly methyl methacrylate assisted exfoliation of graphite and its use in acrylonitrile butadiene styrene composites", Nanotexnology, Thessaloniki (Greece), 29/06/2019 – 06/07/2019

2. S. B. Thorat, A. E. Del Rio Castillo, S. Natalini, E. Lago, **S. Gentiluomo**, L. Marasco, S. Bortolotti, J. K. Panda, R. Oropesa, V. Pellegrini and F. Bonaccorso "*Graphene polymer composites: the effect of flakes aspect ratios on the composite properties*" Graphene week 2018, 10-14 Sept 2018, San Sebastian, Spain.

3. **S. Gentiluomo**, P. S. Toth, E. Lago, S. B. Thorat, V. Pellegrini, and F. Bonaccorso "*Use of poly (methyl methacrylate) for the graphene and polymer composites production*" Graphene 2018, 26-30 June 2018, Dresden, Germany.

4. A. Politano, S. Bellani, E. Petroni, D.W. Boukhvalov, G. Chiarello, A. E. Del Rio Castillo, S. Duman, **S. Gentiluomo**, B. Gürbulak, C.-N. Kuo, E. Lago, C.S. Lue, R. Oropesa, J. K. Panda, V. Pellegrini, and F. Bonaccorso "*Tuning the chemical reactivity of layered metal chalcogenides: the cases of $PtTe_2$ and InSe*" Graphene 2018, 26-30 June 2018, Dresden, Germany.

5. E. Lago, P.S. Toth, **S. Gentiluomo**, S. B. Thorat, V. Pellegrini and F. Bonaccorso, "*Unravelling the boron nitride flakes morphology to enhance polycarbonate performances*" ImagineNano 2018, GraphIN, 13-15 March 2018, Bilbao, Spain.

6. **S. Gentiluomo**, P. S. Toth, E. Lago, S.Thorat, M. Prato, V. Pellegrini, and F. Bonaccorso "*Application of functional polymer inks: two-dimensional crystals production and enhancement of their polymer composites properties*" MRS 2017 Fall Meeting, 26 Nov-01 Dec 2017, Boston (USA).

7. A. E. Del Rio Castillo, A. Ansaldo, F. Ricciardella, H. Sun, **S. Gentiluomo**, S. Enriquez, V. Pellegrini, and F. Bonaccorso, "*Large scale production of 2D crystals by wet jet milling*" Materials.it, 12-16 December 2016, Catania (Italy).

8. **S. Gentiluomo**, P. S. Toth, V. Pellegrini, and F. Bonaccorso "*Exfoliation of graphite in green solvents: Scalable graphene production for polymer composites*" Materials.it, 12-16 December 2016, Catania (Italy).

9. A. Ansaldo, A. E. Del Rio Castillo, F. Ricciardella, **S. Gentiluomo**, V. Pellegrini, and F. Bonaccorso, *"High yield production of large size few layer 2D crystals dispersions by wet jet milling"* Graphene 2016*,* April 19-22, 2016, Genova, Italy.

Poster Communications:

1. E. Lago, P. S. Toth, **S. Gentiluomo**, S.B. Thorat, V. Pellegrini and F. Bonaccorso, *Unravelling the boron nitride flakes morphology to enhance polycarbonate performances*, MRS 2017, 29 Nov-01Dec 2017, Boston, (USA).

2. E. Lago, P. S. Toth, **S. Gentiluomo**, S. B. Thorat, V. Pellegrini and F. Bonaccorso, "*Unravelling the boron nitride flakes morphology to enhance polycarbonate performances*" Graphene 2017, 28-31 March 2017, Barcelona, (Spain).

3. E. Lago, P. S. Toth, **S. Gentiluomo**, S. Thorat, V. Pellegrini, and F. Bonaccorso, "*Enhancing polycarbonate performances by adding environmentally friendly liquid-phase exfoliated boron nitride flakes*" Materials.it, 12-16 December 2016, Catania (Italy).

Contents

Abstract

Advanced materials characterized by a combination of properties, which are not present in conventional materials as metal alloys, ceramics and polymers, are required in technological fields, as aerospace and automotive. For example, the development of materials for structural applications is focused on achieving more than one property, as strength, stiffness and impact resistance. In particular, materials scientists have focused their research on composite materials, due to their wide combination of different properties.

Polymer-based composites are materials formed by a polymeric matrix, containing one or more fillers, which improve the physical and chemical properties of the matrix. The properties of the polymer-based composites can be tailored on-demand depending on the final applications. However, compromises need to be considered for the achievement of the targeted properties. For example, the addition of carbon fibers to a polymer matrix will improve its mechanical strength, but the resulting composite will lose the optical transparency of the pristine material. Nowadays, nanoscale fillers (< 100 nm), as graphene, carbon nanotubes, etc., are proposed as alternative fillers to overcome the limitations provided by the traditional fillers.

In detail, graphene is a nanoscale material which possesses a combo of properties, as a high thermal conductivity (5300 W m^{-1} K^{-1}), outstanding mechanical properties (Young's modulus ~ 1 TPa, tensile strength ~ 130 GPa) and a remarkable electrical conductivity (up to 10^8 S m^{-1}). In a graphene-polymer composite, the matrix benefits from the presence of graphene as filler, so that the mechanical, thermal, electrical and many other properties are enhanced compared to the bare polymer.

However, despite the recent development in the graphene-polymer composites, there are several issues that need to be solved in order to obtain the desired properties. For example, the presence

of graphene aggregates and a weak interaction between the graphene flakes and the matrix hinder the beneficial effect of graphene itself on the matrix properties.

The aim of my PhD work was to enhance the mechanical, thermal, gas barrier and tribological properties of different polymer matrices by exploiting graphene and solving the issues related to factors as the distribution of the graphene in the matrix, for example. Graphene is produced in liquid phase using ultrasonication-based exfoliation and the wet jet milling process, tuning the morphological features of graphene, as area and thickness, by means of sedimentation-based separation.

Graphene-polymer composites are produced using various techniques as solution blending and melt blending and different polymeric matrices, such as acrylonitrile butadiene styrene (ABS), polyamide 6 (PA) and styrene butadiene copolymer (SB). Moreover, the effect of the manufacturing processes on the effect of graphene addition in improving the matrix properties is analysed by using techniques such as 3D printing, injection moulding and compression moulding.

The thesis is organized as follows:

Chapter 1 summarizes the issues and the requirements related to the production of graphene, focusing on the liquid phase exfoliation processes. The main advantages and drawbacks of the production and manufacturing processes of the graphene-polymer composites are explained. Moreover, the factors influencing the mechanical, thermal, gas barrier and tribological properties of the graphene-polymer composites are presented.

Chapter 2 describes the production methods and characterization techniques of both the graphene and the graphene-polymer composites.

Chapter 3 is dedicated to an alternative approach to exfoliate graphite in liquid phase by using acetone as solvent and poly methyl methacrylate (PMMA) as stabilizer. The as-produced graphene

is used to produce ABS composites and the mechanical and gas barrier properties of the composites are tested, focusing on the effect of PMMA on the distribution of graphene in the matrix.

Chapter 4 concerns the tailoring of the morphological properties of graphene, such as lateral size and thickness, by using sedimentation-based separation. The as-produced graphene flakes are exploited to prepare ABS composites, studying the effect of the morphology on the mechanical properties of the composites.

Chapter 5 presents the use of the wet jet milling process to produce graphene, which is then used to prepare graphene-polyamide 6 (PA) composites, exploiting PMMA to improve the distribution of graphene in the matrix. The effect of the improved graphene distribution on the mechanical, thermal and tribological properties is studied.

Chapter 6 reports the effect of two manufacturing techniques, injection moulding and compression moulding, on the mechanical and thermal properties of graphene-styrene butadiene copolymer (SB) composites. The composites are prepared using the graphene obtained from the wet jet milling process.

Chapter 7 summarizes the most important results obtained in the thesis work, from the production of graphene to the improvements achieved in the properties of graphene-polymer composites. Moreover, some hints about the future exploitation of the acquired knowledge on the graphene-polymer composites will be presented.

Chapter 1: Introduction on graphene and its polymer composites

1.1 Graphene

Carbon is the atomic building block of all the organic materials, being able to form a variety of hybridization states with the neighbouring carbon atoms, such as *sp, sp^2, sp^3*. (*1*, *2*) The best-known carbon allotropes are diamond (sp^3 hybridization) and graphite (sp^2 hybridization), due to their different physical properties (*i.e.,* hardness, density, electrical and thermal conductivity and transparency). (*1*, *2*)

In the last decades, many more allotropes and forms of carbon have been discovered and investigated, such as, fullerenes, carbon nanotubes (CNTs), carbon nanohorns and graphene. (*1–4*) (**Fig. 1**)

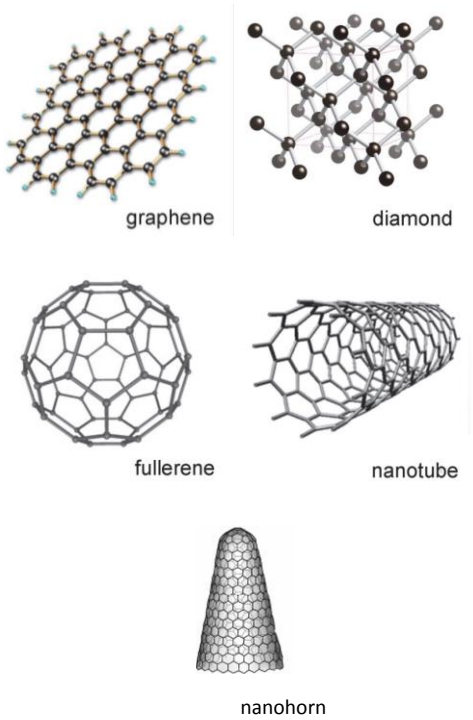

Figure 1 *- Representative allotropes of carbon* (*5*) (*3*, *4*)

These carbon allotropes are attractive for a wide range of applications, owing to their properties as surface area, electrical and thermal conductivity, mechanical strength, etc. (table 1). (*3*, *4*, *6*)

Table 1 *– Surface area, electrical and thermal conductivity and mechanical strength of carbon allotropes*

	Surface area [$m^2 g^{-1}$]	Electrical conductivity [$S m^{-1}$]	Thermal conductivity [$W m^{-1} K^{-1}$]	Mechanical strength [GPa]
Graphene	~ 2630 (*7*)	~ 10^8 (*8*)	~ 5300-6000 (*9*)	~ 130 (*10*)
Diamond	~ 300-400 (*11*)	~ 10^{-11}-10^{-18} (*12*)	~ 2200 (*13*)	~ 95 (*14*)
Fullerene	~ 1180-1360 (*15*)	~ 10^{-3} (*16*)	~ 0.4 (*16*)	~ 42 (*17*)
Carbon nanotubes	~ 50-1315 (*18*)	~ 10^6 (*19*)	~ 2000-6000 (*20*)	~ 98-110 (*21*)
Carbon nanohorns	~ 300-400 (*22*)	~ 10^2 (*23*)	N.D.	~ 20 (*24*)

For example, fullerene is exploited in organic solar cells (*25*), in hydrogen storage (*26*) and also for medical applications (*27*). Instead, carbon nanotubes (CNTs) are involved in the fabrication of solar cells (*28*), supercapacitors (*29*) and sensors (*30*). Carbon nanohorns, also known as nanocones, are closed cages of sp^2 bonded carbon atoms and they are implemented mostly for biological applications. (*4*) In fact, carbon nanohorns are exploited as drug carriers (*31*, *32*) and biosensors (*33–35*), but also as component in the anode of biofuel cells (*36*).

Graphene consists of a two-dimensional honeycomb network of sp^2-hybridized carbon, presenting a carbon-carbon bond distances of 0.142 nm. (*37*) P.R. Wallace was the first person to study graphene in 1947, describing this material as a zero gap semiconductor, owing to the absence of an electronic energy gap. (*38*) In order to synthesize graphene, various attempts were carried out including the use of similar approach for the growth of carbon nanotubes, or producing graphite nanoflakes with ≈ 100 layers of graphene. (*39*) In 2004, Andre Geim and Konstantin Novoselov isolated graphene, by means of mechanical exfoliation of graphite, *i.e.,* the "Scotch tape method". (*37*) Thanks to the exceptional charge transport (carrier mobility ~ 15000 $cm^2 V^{-1} s^{-1}$ (*40*)), electrical (conductivity ~ 10^8 $S m^{-1}$ (*40*)), optical properties (transmittance ~ 97.7 % (*41*)) of graphene (*37*), it is used in many applications regarding electronic devices (*42*), chemical sensors (*43*), nanocomposites (*44*) and energy storage (*45*), just to mention a few.

1.1.1 Mechanical properties of graphene

The mechanical properties of a free-standing single-layer of graphene (SLG) was first measured by Lee and co-workers by using nanoindentation with atomic force microscopy (AFM). (*10*) The results have shown that graphene possesses Young's modulus around 1 TPa and intrinsic strength of ~ 130 GPa. (*10*) Graphene owes these exceptional mechanical properties to the sp^2 bonds that form the hexagonal lattice. (*46*) The in-plane stiffness of graphene, *i.e.,* the ratio of in-plane stress and strain, was also measured. (*47*, *48*) But, different values ranging between 20 N m^{-1} and 100 N m^{-1} are reported, arising from the inherent crumpling of graphene in the out-of-plane direction of the monolayer. (*47*, *48*) Crumpling of graphene is caused by either out-of-plane flexural phonons or from static wrinkling. (*47*, *48*) The latter is induced by the uneven stress at the boundary of the graphene, and it is responsible for the worsening of the mechanical properties of the material. (*47*, *48*) Graphene is known as one of the strongest materials, see **Fig. 2**, and for this reason, it is widely used as a reinforcing filler in polymer composites. (*46*)

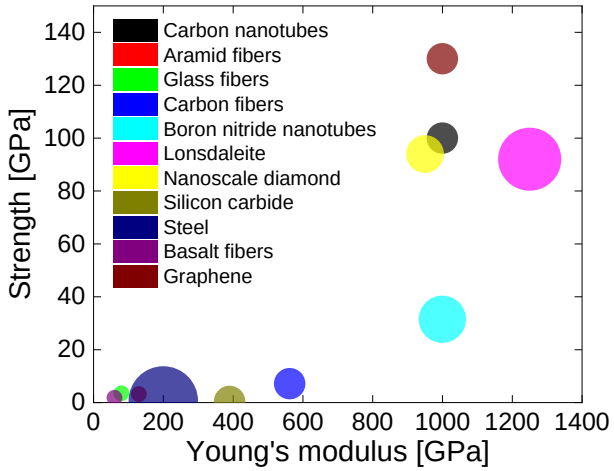

Figure 2 *- Mechanical properties of some materials compared with graphene; carbon nanotubes* (*21*)*, aramid fibers* (*49*)*, glass fibers* (*50*)*, carbon fibers* (*51*)*, boron nitride nanotubes* (*52*)*, Lonsdaleite* (*53*)*, nanoscale diamond* (*14*)*, silicon carbide* (*54*)*, steel* (*55*)*, basalt fibers* (*50*)*.*

1.1.2. Thermal properties

The thermal conductivity in the in-plane direction of graphene is high due to covalent sp^2 bonding between carbon atoms. (*56*) The predicted thermal conductivity of SLG at room temperature has an extremely high value ~ 5300-6000 W $m^{-1}K^{-1}$. (*9*) While, the thermal conductivity of a suspended SLG was measured in a range between 2000 W $m^{-1}K^{-1}$ and 4000 W $m^{-1}K^{-1}$. (*57*, *58*). Chen S. et al. (*57*), measured the thermal conductivity to be around ~ 2600-3100 W $m^{-1}K^{-1}$ in a vacuum environment at a temperature of 350 K, by using Raman measurements.

Graphene is one of the materials with the highest thermal conductivity (see **Fig. 3**).

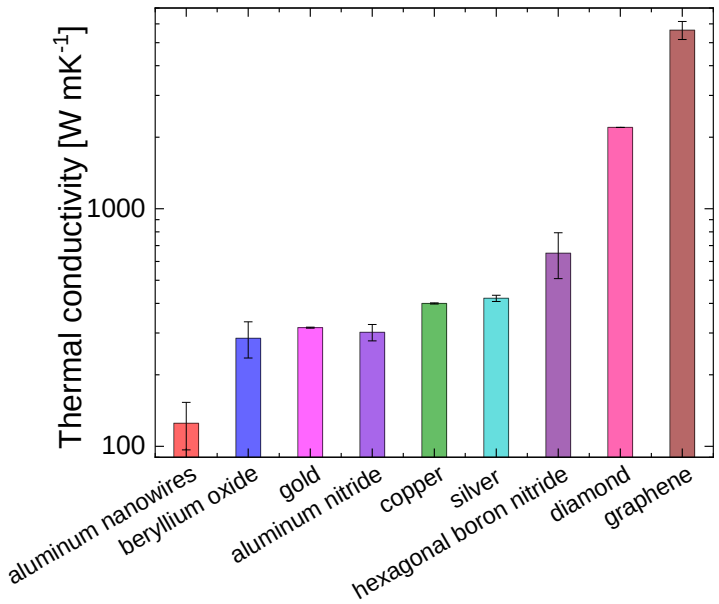

Figure 3 *- Thermal conductivity of some materials: aluminum nanowires* (*59*)*, beryllium oxide* (*60*)*, gold* (*61*)*, aluminum nitride* (*62*)*, copper* (*63*)*, silver (bulk)* (*61*)*, hexagonal boron nitride* (*64*)*, diamond* (*13*) *and graphene (9).*

1.1.3. Electrical properties

Graphene is a zero gap semiconductor, as the valence band and the conduction band are intersecting at two inequivalent points K and K' in the reciprocal space. (*65*) Near the K and K' points, the electronic dispersion resembles that of relativistic Dirac electrons, so that these points are called the "Dirac points" (see **Fig. 4**). (*65*) Therefore, the Dirac points define the Fermi level as the zero energy reference and the Fermi surface. (*65*)

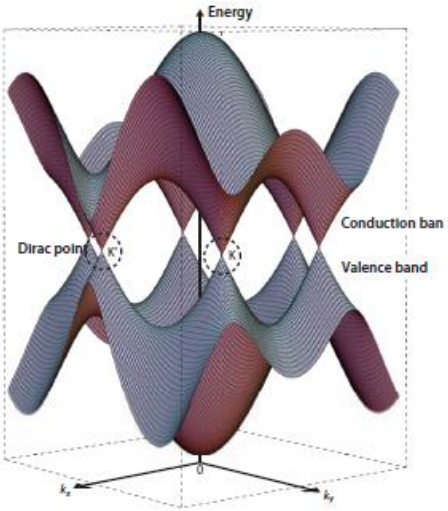

Figure 4 *- Schematic diagram of the linear energy band dispersion in graphene at the Dirac points* (*66*)

The carriers mobility is inversely proportional to the carrier effective mass (*67*) and an extremely high carrier mobility is expected for electrons in graphene, as they behave as massless Dirac fermions, being free to move for micrometers, at room temperature, without scattering. (*68*) Experimental results have shown that the carrier mobility values of SLG to be around 15000 $cm^2\ V^{-1}\ s^{-1}$ and an electrical conductivity (σ_{el}) around 10^8 S m^{-1}. (*8*)

Graphene is known as one of the best electrically conductive material in the world, in fact its electrical conductivity is higher compared to silver ($\sigma_{el\text{-}silver}$ = 66.7 10^6 S m^{-1} (*69*)) and copper ($\sigma_{el\text{-}copper}$ = 64 10^6 S m^{-1} (*69*)), for example (see **Fig. 5**).

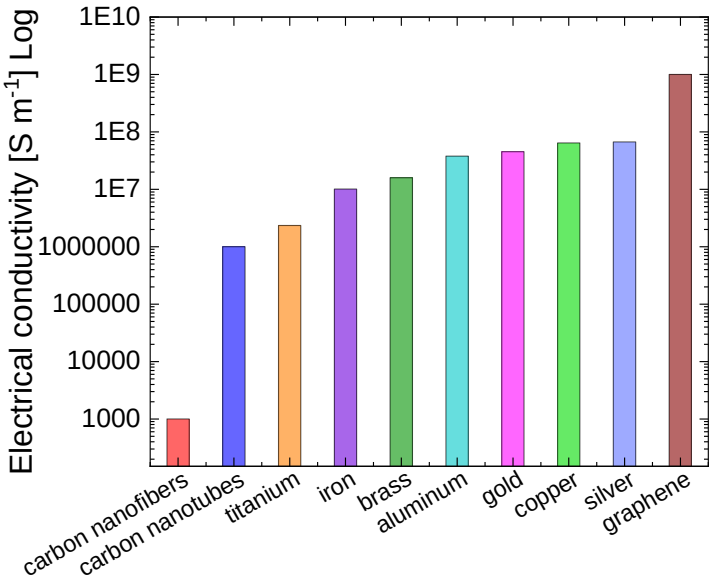

Figure 5 *– Electrical conductivity of graphene compared with other materials; carbon nanofibers* (*19*)*, carbon nanotubes* (*19*)*, titanium* (*70*)*, iron* (*71*)*, brass* (*71*)*, aluminum* (*70*)*, gold* (*70*)*, copper* (*70*)*, silver* (*70*)*.*

1.2 Production of graphene

The production routes of graphene are divided into two main approaches, *i.e.,* bottom-up, which consists in building up the lattice of the graphene flake atom by atom, and top-down, in which the flakes are obtained from stripping the layers of graphite. (*72*, *73*)

The main bottom-up processes are the growth of graphene on a silicon carbide substrate (SiC), the precipitation from metal and the chemical vapour deposition (CVD), as shown in **Fig. 6**. (*72*, *73*)

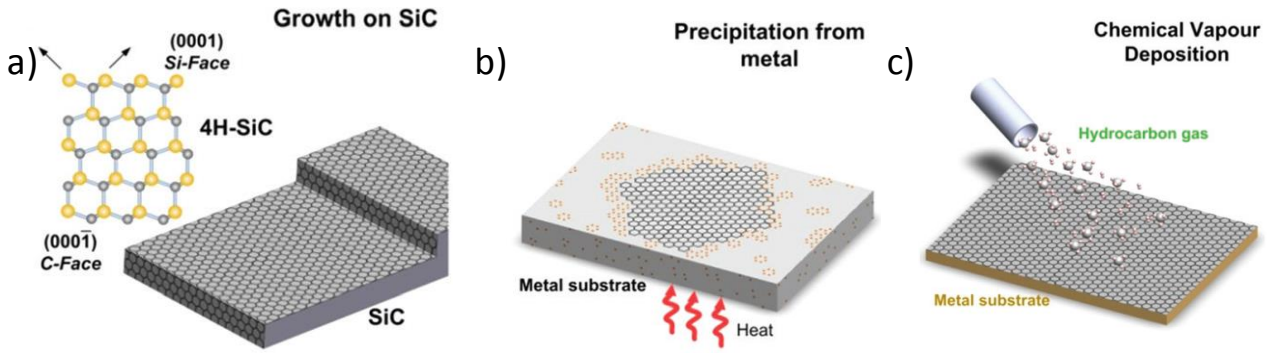

Figure 6 *– Main bottom-up process: a) Growth on SiC, b) Precipitation from metal, c) Chemical vapour deposition* (*73*)

The thermal decomposition of SiC is a method known since 1896, for the production of graphite from SiC, as reported by Acheson. (*74*) The annealing at high T, *e.g.,* 1080 °C-1320 °C, under ultra-high vacuum of both the polar faces, *i.e.,* the Si-terminated (0001) and the C-terminated (000 -1), leads to the graphitization of SiC, because of Si evaporation. (*75*)

The graphene layer is not grown directly on the surface of the SiC substrate, but on a carbon rich interfacial layer (6√3×6√3)R30° with respect to the (0001) surface, called "buffer layer". (*73*, *76*) The buffer layer presents the carbon atoms arranged in a hexagonal structure, but it does not possess the same properties of graphene, because ~ 30 % of the carbon atoms are covalently bonded to Si atoms. (*73*, *76*) During the growth of graphene, the Si undergoes sublimation during the annealing, and the buffer layer provides a template for the re-arranging of the carbon atoms. (*73*, *76*)

Although there is a considerable lattice mismatch between SiC (3.073 Å) and graphene (2.46 Å), this process is usually referred to as "epitaxial growth". The usual range of annealing temperatures goes from 1300 °C to 2000 °C, while the typical heating and cooling rates are 2-3°C s^{-1}. (*76*, *77*) However, the thermal decomposition is not a self-limiting process, so that areas of different film thicknesses may exist on the same SiC crystal. (*73*, *76*) Moreover, the cost of the SiC wafers blocks up the breakthrough of this method. (*73*, *76*) The main advantage regards the fact that the graphene layer does not need to be transferred to another insulator substrate, as SiC is already insulating. (*73*, *76*) In fact, SiC is commonly used in power electronics as substrate (*78*), graphene grown on SiC is particularly suitable for applications in this field (*79*), as field-effect transistors (*80*) and integrated circuits (*81*). Therefore, all the drawbacks due to the transferring process can be avoided, as will be discussed later, for example, for the CVD technique. (*82*)

The growth of graphene on metal by precipitation is performed on a metallic substrate containing carbon atoms. The solubility of the carbon atoms increases when the metal is annealed at high temperature, *i.e.,* > 1000 °C, in ultra-high vacuum. (*72*, *73*) Then, the system is cooled down, so that

the solubility of carbon atoms is decreased, leading to precipitation to form a graphene film. (*72*, *73*) The metals suitable for the precipitation process are those, which do not form stable carbides, so that there is no competition between the synthesis of carbide and the formation of graphene. (*72*, *73*) Moreover, there should not be a large mismatch, *i.e.*, > 20 %, between the lattices parameters of the metal and of the graphene. (*83*) As an example, the metals as titanium, tantalium and silicon form thermally stable carbides, so they are not suitable for growing graphene. (*83*) While, nickel (*84*, *85*), platinum (*86*) and copper (*84*, *85*) are proper substrates. The graphene flakes produced by this process are few-layer graphene (FLG) from micrometre (*85*) to centimetre size (*84*). The as-produced graphene-metal composite can be used as thermal interface materials for heat dissipation in electronic devices. (*85*) However, the transfer of the graphene flakes onto arbitrary substrates is problematic, as it is difficult to separate the graphene layer from the metal substrate. (*72*, *73*)

Chemical vapour deposition is based on the decomposition of hydrocarbon precursors, *e.g.,* methane (*87*), acetylene (*87*) and ethylene (*87*), into carbon radicals, which are deposited onto a metal substrate, *e.g.,* copper (Cu) (*88*), starting the nucleation of graphene.

In 2009, polycrystalline Cu was used to grow the first uniform, large area (~ cm^2) graphene on a metal surface, exploiting methane as precursor. (*89*) The growth of graphene on this substrate is almost self-limited, as it stops as soon as the surface of the Cu is fully covered, producing bi-layer and tri-layer graphene. (*89*) Copper is suitable as substrate due to the low solubility of carbon atoms in it (*90*) and its mild catalytic activity (*91*). One of the main issues is the mismatch in the thermal expansion coefficient between the Cu substrate and the growing graphene. (*88*) This difference leads to the formation of wrinkles on the produced graphene, which damage the electronic properties of graphene. (*92*)

Graphene films synthesized on a metal substrate have to be transferred to the substrate of interest for the desired application. (*82*) A graphene transfer technique has to solve two issues, the separation of the graphene from the metal substrate and the protection of graphene integrity after the separation. (*82*) A conventional way to protect the integrity of graphene, during the transfer process, is the use of a support layer coated on top of the graphene surface, *e.g.,* poly methyl methacrylate (PMMA) (*93*), and the metal substrate can be removed by etching, for example. (*82*)

After the removal of the support, the so obtained graphene is exploited for applications in photonics and optoelectronics(*94*), *e.g.,* photodetectors (*95*), light-emitting diodes (*96*), transparent conductors (*97*), and flexible electronics (*98*, *99*)

The main top-down processes are micromechanical cleavage (MC) and liquid phase exfoliation (LPE). (*72*, *73*) (**Fig. 7**)

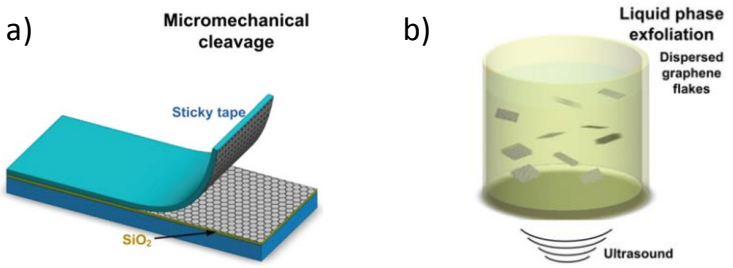

Figure 7 *- Top-down process: a) micromechanical cleavage, b) liquid-phase exfoliation* (*73*)

Micromechanical cleavage was used in 1999 to cleave graphite, yielding films consisting of several layers of graphene. (*100*) This study suggested that multiple or even single atomic layers of graphite layers could be obtained through more extensive rubbing of the graphite surface against other flat surfaces. (*100*) Then, in 2004, Novoselov and Geim managed to isolate SLG, by peeling-off the layers of graphite using adhesive tape. (*101*) This process consists in cleaving repeatedly the first piece of graphite with scotch tape, to obtain an almost invisible powder on the starting tape. (*102*)

The graphene produced using this procedure possesses high quality in terms of morphology and crystallinity, *i.e.,* SLG with a lateral size in the order of millimetres. (*101*, *103*) Micromechanical cleavage can be used to produce graphene for fundamental research, but, due to its lack of scalability, it is impractical for industrial applications. (*10*, *37*, *104*)

Liquid phase exfoliation relies on the exfoliation of graphite in liquid environments, starting with the dispersion of graphite into a solvent, followed by the exfoliation and "purification" of the obtained dispersion from the thickest and un-exfoliated flakes. (*72*, *73*, *105*) This process allows obtaining dispersions containing both SLG and FLG with a size in the order of nanometres. (*72*, *73*, *105*) The LPE is cheap, easily scalable and versatile. (*72*, *73*, *105*) In fact, the as-produced graphene dispersions can be exploited, for example, in a wide range of applications, as conductive inks (*106*, *107*) and to produce fillers for polymer composites.(*44*) Moreover, the LPE graphene dispersion can be deposited onto both flexible and rigid substrates, through various techniques such as dip coating (*108*, *109*), inkjet printing (*110*–*112*) and spray coating (*113*).

1.3 Liquid-phase exfoliation process

In the following paragraphs, the three steps of the LPE process will be discussed in detail. As stated few lines above, the liquid phase exfoliation process is divided into three steps, the dispersion of graphite into a proper solvent, the exfoliation of graphite and the "purification" of the obtained graphene dispersion from the thickest and un-exfoliated flakes. (*72*, *73*)

1.3.1 Dispersion of graphite into the solvent

The solvent for the dispersion of graphite and stabilization of the exfoliated flakes is selected following two different approaches, considering the Hansen parameters or the surface tension of the solvent. (*72*, *73*)

1.3.1.1 The Hansen parameters

In a solvent-solute system, the solvent and the solute molecules interact mainly through three kind of interactions, dispersive interactions, polar interactions and hydrogen bonding. (*114*) Dispersive interactions results from the temporary formation of dipoles on the adjacent molecules of solvent and solute. (*114*) While, polar interactions are created between the molecules having a dipole, due to the presence of an electronegative atom, *e.g.,* oxygen. (*114*) Instead, hydrogen bonding is a dipole-dipole interaction, where the hydrogen atom present on one molecule is non-covalently attracted to an electronegative atom belonging to another molecule. (*114*)

The Hansen solubility parameters are the square roots of the dispersive, polar, and hydrogen bonding components of the cohesive energy density of the solvent/solute. (*115*) Those parameters are denoted as δ_D, δ_P and δ_H for the dispersive, polar and hydrogen bonding interactions, respectively. (*115*)

In order to promote the dispersion of graphene into a solvent, the enthalpy of mixing, *i.e.,* ΔH_{mix}, has to be minimized and it is defined in equation 1: (*115*)

$$\frac{\Delta H_{mix}}{V} \approx \frac{\left[\left(\delta_{D,S}-\delta_{D,G}\right)^2 + \frac{\left(\delta_{P,S}-\delta_{P,G}\right)^2}{4} + \frac{\left(\delta_{H,S}-\delta_{H,G}\right)^2}{4}\right]}{\Phi} \quad \textit{Equation 1}$$

Where $\delta_{D,S}$, $\delta_{P,S}$ and $\delta_{H,S}$ are the Hansen parameters of the solvent, $\delta_{D,G}$, $\delta_{P,G}$ and $\delta_{H,G}$ are the Hansen parameters of graphene and Φ is the dispersed graphene volume fraction. (*115–117*) Therefore, a solvent is suitable for the dispersion of graphene when its Hansen parameters are similar to the ones of graphene. (*115–117*) Hernandez et al. found out that the best solvents present δ_d in a range between 15 $MPa^{1/2}$ and 21 $MPa^{1/2}$, δ_P around 12 $MPa^{1/2}$ and δ_H around 9 $MPa^{1/2}$. (*116*, *117*)

1.3.1.2 The surface tension

The dispersion of a solute into a solvent depends on the Gibbs free energy of mixing (ΔG_{mix}), which has to be zero or negative and it is expressed in equation 2: (*115*)

$$\Delta G_{mix} = \Delta H_{mix} - T\Delta S_{mix} \quad \textit{Equation 2}$$

In equation 2, ΔH_{mix} is the enthalpy of mixing, T is the temperature and ΔS_{mix} is the entropy of mixing. (*115*) ΔS_{mix} is small for large-sized particles like graphene, so for the stabilization and the dispersion of graphene flakes in the solvent ΔH_{mix} has to be minimized. (*117*, *118*)

ΔH_{mix} is defined by using equation 3: (*117*, *118*)

$$\frac{\Delta H_{mix}}{V_{mix}} = \frac{2}{t}(\delta_G - \delta_{sol})^2 \Phi \quad \textit{Equation 3}$$

in which V_{mix} is the volume of solvent, t is the thickness of the flakes, δ_G and δ_{sol} are the square roots of the surface energy (γ_E) of graphene and the surface tension of the solvent (γ). (*117*, *118*)
The solvents that are suitable for the exfoliation of graphite possess a surface tension between ~ 40 mN m^{-1} and ~ 50 mN m^{-1}(*118*). The surface tension is the most common property used for the choice of the solvent to disperse the graphite in the LPE process. (*117–140*)

1.3.1.3. Solvents and systems for the dispersion of graphite

In literature (*117*, *118*, *129*, *134–137*, *141*), the solvents chosen for the dispersion of graphite, on the basis of their surface tension, are, for example, N-methyl-2-pyrrolidone (NMP) (γ_{NMP} = 40.21 mN m^{-1} (*142*)), γ-butyrolactone (GBL) (γ_{GBL} = 46.5 mN m^{-1} (*142*)) and dimethylsulfoxide (DMSO) (γ_{DMSO} = 42.9 mN m^{-1}.(*142*)). However, these solvents are toxic, *e.g.,* NMP is suspected to be teratogenic (*143*), and possess a high boiling point (T_b), *e.g.,* T_b(NMP) = 202 °C (*144*). The removal of these solvents is an issue for the subsequent processing of

the graphene dispersions. (*72*, *73*) For example, when graphene dispersions are used in processing techniques as inkjet printing (*112*, *145*), flexography (*146*) and spray coating (*147*), the evaporation of the solvent is fundamental for the preparation of devices. Moreover, it is necessary to remove the residues of solvents in the production of graphene-polymer composites, as they affect the physical and chemical properties of the composite. For example, the presence of solvent residual, as it forms bubbles that damage the mechanical properties of the composites. (*148*, *149*) An alternative could be to use low boiling point solvents, i.e., $T_b \leq 100$ °C, but their surface tension does not match the required values (40-50 mN m^{-1}) to disperse the graphite and stabilize the graphene flakes. (*119*, *138–140*) For example, water, isopropanol (IPA) and acetone are not ideal, as their surface tension is around 70 mN m^{-1}, 23 mN m^{-1} and 25.2 mN m^{-1}. (*142*) Therefore, the presence of molecules, as surfactants (*120–124*, *132*, *133*) or polymers (*125–128*, *130*, *131*), is needed to stabilize the graphitic flakes. Ionic and non-ionic surfactants are exploited to disperse graphite in low boiling point solvents, *e.g.,* water (*120*, *123*, *132*), acetic acid (*124*), methanol (*150*), IPA (*150*), ethanol (*150*), acetone (*150*). Surfactants stabilize the graphene flakes hindering the re-aggregation after the exfoliation step by repulsive interactions between the surfactant-coated graphene flakes (**Fig 8**). (*122*) Surfactants are formed by a hydrophobic head, which usually interacts with graphene and a hydrophilic tail, protruding into the solvent. (*122–124*) In literature, the surfactants used in the production of graphene can be divided in non-ionic surfactants and ionic surfactants. (*122–124*) Non-ionic surfactants stabilize the flakes by means of steric repulsion between the hydrophilic tails, a few examples of this kind of surfactants are TritonX100 (*120*), Tween 80 (*121*), Pluronic P123 (*132*) (*120–122*). While, in ionic surfactants, the hydrophobic tail group adsorb by van der Waals or π-π interactions to the graphene flakes and the stabilization occurs by means of electrostatic repulsion. (*122–124*) In literature, examples of ionic surfactants used in LPE are edge carboxylated graphene quantum dots (ECGQD) (*150*), sodium cholate (SC) (*123*),

cetyltrimethylammonium bromide (CTAB) (*124*), sodium dodecylbenzene sulfonate (SDBS) (*123*), sodium carboxymethyl cellulose (CMC) (*133*).

But, the use of surfactants has some drawbacks, as they affect the physical and chemical properties of the flakes. (*151*, *152*)

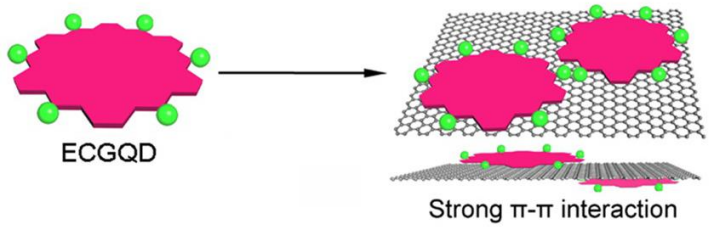

Figure 8 – Example of interaction between graphene and edge carboxylated graphene quantum dots used as surfactant (*150*)

Polymers "assist" the dispersion of graphite and the stabilization of the exfoliated flakes by both steric and electrostatic repulsion in the solvent. (*125–128*, *130*, *131*) In literature, conductive polymers (*128*, *130*), *e.g.,* Nafion (*130*), block copolymers (*126*, *131*), *e.g.,* poly(styrene sulfonic acid-graft-polyaniline) (S-g-A) (*128*), or acrylate polymers (*125*) are exploited in the LPE process with various low boiling point solvents, as ethanol (*125–128*), isooctane (*131*) and mixtures of water-ethanol (*130*). The as-produced graphene dispersions are involved in coolant applications (*125*), in the preparation of supercapacitors (*128*) or used as electrically conductive inks (*130*, *131*), just to mention a few.

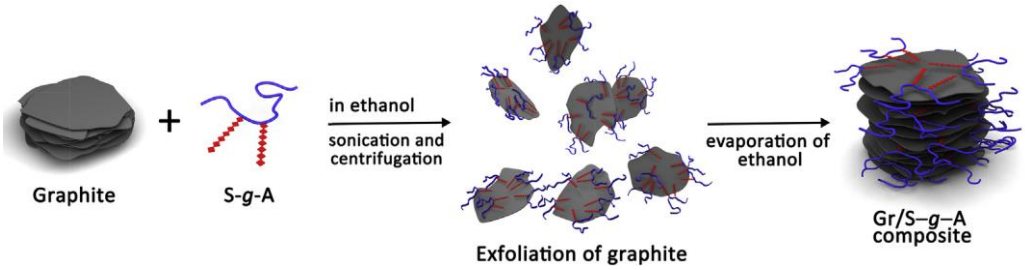

Figure 9 *– Exfoliation of graphite in ethanol using poly(styrene sulfonic acid-graft-polyaniline) (S-g-A) as a stabilizing agent in ethanol* (*128*).

1.3.2 The exfoliation of graphite

The exfoliation of graphite is carried out by means of different techniques, involving physical-chemical phenomena as cavitation (*133*, *153*), shear forces (*135*, *154*, *155*), intercalation (*156–158*) and functionalization (*159*, *160*). The thesis will be focused on the exfoliation of graphite induced by cavitation and shear forces, as intercalation and functionalization compromise the crystalline structure and change the graphene flakes properties. (*156–160*)

1.3.2.1 Cavitation

The cavitation is generated by the ultrasonic waves travelling through the solvent, which generate pulsed pressure waves. (*161–165*) These waves are concentrated both in low-density elastic waves and high-density elastic waves, leading to the production, growth and collapse of micrometre-sized bubbles. (*161–165*) (**Fig. 10a**) The bubble implosion creates micro-jets of the solvent, which leads to the formation of a shock-wave, peeling-off the layers of graphite. (*161–165*) (**Fig. 10b**)

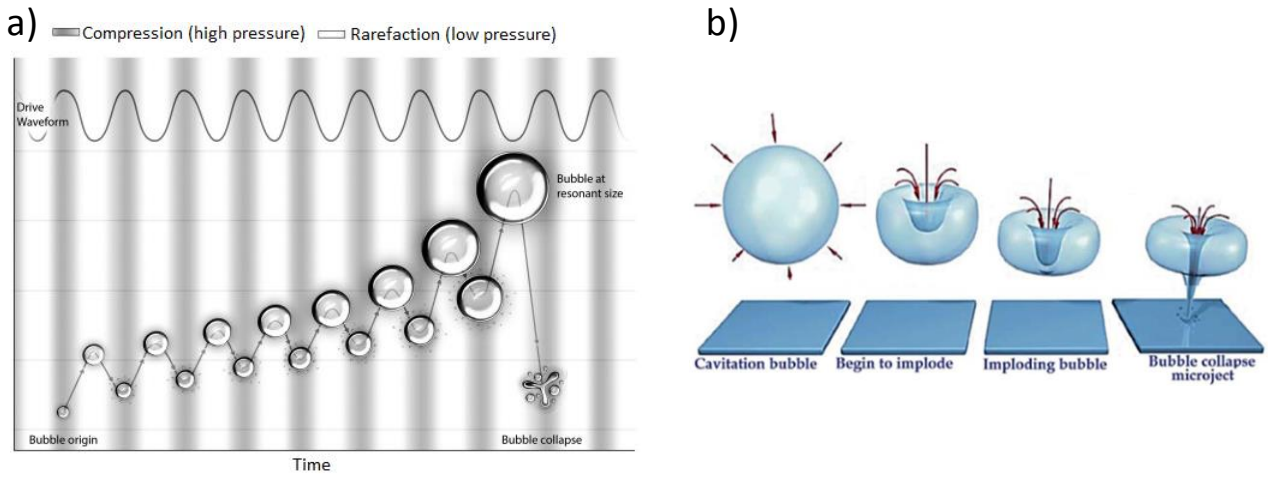

Figure 10 *– a) Mechanism of cavitation* (*166*) *and b) Implosion of the bubble to form micro-jet* (*167*)*.*

Ultrasonication can be performed using either sonic baths (*118*, *168–170*) or tip sonicators (*171*, *172*). In low-intensity bath sonication, an ultrasonic wave is created propagating through both tank and reaction container. (*118*, *168–170*) In tip ultrasonicators, the sonication zone is located directly

under the sonotrode and the exfoliation depends on factors, as sonic power, amplitude and frequency, for example. (*171*, *172*) The main issues of ultrasonication regard the poor reproducibility of the process, due to the non-uniform distribution of the waves in the tank, (*173*) and the fragmentation of the flakes (*174*).

1.3.2.2 Shear forces

The minimum shear rate required to overcome the van der Waals interaction and peel-off the layers of graphite is 10^4 s^{-1}. (*135*) In order to obtain the shear rate necessary for the exfoliation, a turbulent flow, *i.e.,* flow in which a fluid undergoes irregular fluctuations, is needed. (*175*) The flow behaviour is defined by the Reynolds number (*Re*), a dimensionless parameter, which is the ratio among the inertial and viscous forces within a fluid. (*176*, *177*) Inertial forces are the force due to the momentum of the fluid, while the viscous forces are due to the friction generated in the flow of a fluid. (*176*, *177*) *Re* is expressed in equation 4: (*176*, *177*)

$$Re = \frac{\rho u D}{\eta} \quad \textit{Equation 4}$$

Where ρ is the solvent density, u is the mean velocity of the fluid inside the channel with diameter D and η is the viscosity of the solvent. (*176*, *177*) In a system formed by mini channels (3 mm > diameter > 200 µm) and micro channels (200 µm > diameter > 10 µm), a turbulent flow is achieved when the Re number is larger than ~ 3000. (*176*, *177*)

1.3.2.3 Ultrasonication-based exfoliation and high-pressure homogenizers

The exfoliation process of graphite is performed by ultrasonication based methods. (*117–132*, *134–140*) Moreover, instruments called “high-pressure homogenizers” are used to exfoliate graphite, examples of techniques involved in this method are jet-cavitation (*133*, *178*), microfluidisation (*107*, *179–181*) and wet jet milling (WJM) (*154*, *165*).

In ultrasonication (*182*, *183*), the main driving force of the exfoliation of graphite is the cavitation, which is caused by ultrasounds. While in jet-cavitation (*133*, *178*), the graphite is exfoliated by the hydrodynamic-induced cavitation by pressure difference. In high-pressure homogenizers, the shear forces may be the principal cause of exfoliation. (*165*) In detail, the solvent-graphite mixture is passed through a narrow pipe, channels or small nozzles (0.08 – 2 mm), using pressures ranging from 10 to 250 MPa. (*107*, *133*, *154*, *165*, *178–181*) The flow velocity of the graphite-solvent mixture increases (or decreases) with the tightening (or widening) of the channels, leading to the creation of turbulent flows. (*107*, *133*, *154*, *165*, *178–181*) Turbulent flows induce an increase (or decrease) in the shear rate. (*107*, *133*, *154*, *165*, *178–181*)

1.3.2.4 Figures of merit

The evaluation of the effectiveness of the LPE techniques, in terms of production rate and time required for the exfoliation, is carried out by considering a set of figures of merit (*FoM*). The most commonly used *FoM's* are the concentration ($C\ [g\ L^{-1}]$), the exfoliation yield by weight ($Y_w\ [\%]$), which is defined as the ratio of the weight of the exfoliated flakes divided by the initial weight of the graphite. (*154*) In order to assess if the exfoliation techniques are potentially suitable for the industrial scale, the time ($t_{1gram}\ [hours]$) and the volume ($V_{1gram}\ [L]$) needed to produce 1 gram of exfoliated flakes are also considered as *FoM*. (*154*)

1.3.2.5 Comparison between ultrasonication and high-pressure homogenizers

The FoM's of the different exfoliation techniques are presented in table 2. Due to the high values of t_{1gram} and V_{1gram}, the ultrasonication method is not suitable for the large scale production, different from the high-pressure homogenizers.

Among the high-pressure homogenizers techniques, the WJM stands out as a potentially industrial-scale processes, as it presents a 100 % of exfoliation yield. Although the microfluidification present

an exfoliation yield of 100 % as well, the WJM process is more advantageous as it has lower t_{1gram} and V_{1gram} compared to the microfluidification. Moreover, WJM allows producing thinner flakes (FLG) compared to microfluidification, whose dispersions contain mainly MLG flakes.

Table 2 *– Exfoliation methods showing the FoM calculated within the information supplied in the respective papers. Acronyms: edge carboxylated graphene quantum dots (ECGQD), dimethylformamide (DMF), multi-layer graphene (MLG), no data supplied (n.d.).*

Process	Solvent-stabilizer	C [g L^{-1}]	Graphene flakes	Y_w [%]	t_{1gram} [hours]	V_{1gram} [L]	Ref.
Sonic bath	IPA-ECGQD	0.25	FLG	0.5	360	20	(*150*)
	Water-Pluronic P123	1	FLG	1	2.5	0.01	(*132*)
	Ethanol-block copolymer	1.7	FLG	68	2	2.3	(*126*)
	NMP	2	FLG	19	30	0.53	(*141*)
Jet-cavitation	Water-CMC	11	FLG	4	0.5	30	(*133*)
	Acetone-water	0.1	FLG	12	8	10	(*178*)
Microfluidisation	Water-TritonX	7.2	FLG	18	0.3	0.5	(*179*)
	Water-SC	0.31	FLG	3	14	3.2	(*180*)
	Water-CMC	80	MLG	100	4	0.36	(*107*)
	Water-Tween	0.25	FLG	2.23	0.1	4	(*181*)
WJM	NMP	10	FLG	100	0.04	0.1	(*154*)
	Water-SC	10	MLG	100	0.04	0.1	(*154*)
	DMF	0.1	FLG	n.d.	1	10	(*165*)

1.3.2.6 The WJM process

The wet-jet mill instrument has a hydraulic mechanism and a piston supply the pressure (up to 250 MPa), which pushes the graphite-solvent mixture into a processor. The processor consists in a

set of 5 different perforated and interconnected disks (**Fig. 11**). (*154*) The process is performed as follows, firstly the graphite-solvent mixture is passed through the two channels of disk A (**Fig. 11**), forming jet streams due to the pressure applied by the piston. Then, the formed jet streams collide in the junction between disk A and B (**Fig. 11**), where a turbulent flow is created. The turbulent flow induces a high-shear rate (~ 10^8-10^9 s^{-1}) promoting the graphite exfoliation, as the mixture passes through disk B. (**Fig. 11**) Finally, the mixture passes through the disk A' (**Fig. 11**) being separated in two channels and exiting the processor. The diameter of the nozzle can be adjusted from 0.3 mm to 0.1 mm, in order to enhance the effectiveness of the shear forces. (*154*)

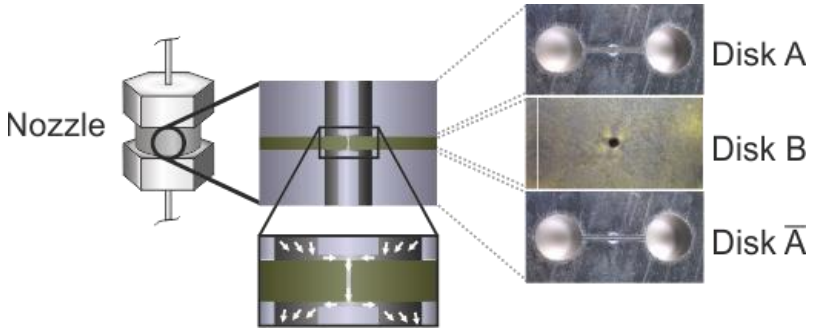

Figure 11 *- Scheme of the processor of the WJM process.*

1.3.3 "Purification" step: sedimentation based separation (SBS)

After the exfoliation, the graphene dispersion needs to be "purified" from thick (> 10 layers) and un-exfoliated flakes. (*102*) The strategies used for the "purification" are sedimentation based separation (SBS), in a uniform medium, (*184*) and density gradient ultracentrifugation (DGU), in a density gradient medium (*185*). The SBS is the most common technique used and it separates the particles on the basis of their sedimentation rate. (*184*)

The SBS is based on applying a centrifugal force field on particles dispersed in a solvent (**Fig 12**). (*184*, *186*) In the SBS there are various forces which apply to the particle dispersed into a solvent, the centrifugal force can be expressed as $F_c = m_p \omega^2 r$, where m_p is the mass of the particle,

r is the distance from the rotational axes and ω is the angular velocity. (*184*) Instead, the buoyant force $F_b = -m_s \omega^2 r$, is proportional to the mass of the displaced solvent (m_s), and the frictional force $F_f = -fv$, which depends on the friction coefficient between the solvent and the particle (f) and the sedimentation velocity of the particle itself (v). (*184*) The sedimentation coefficient is defined as (*184*):

$$S = \frac{v}{\omega^2 r} = \frac{m_p\left(1-\frac{\rho_s}{\rho_p}\right)}{f} \quad \textit{Equation 5}$$

Where ρ_s and ρ_p are the density of the solvent and of the particle, respectively. The sedimentation coefficients of thick and large flakes are higher compared to the small flakes. (*184*, *187*, *188*) It is possible to tune the lateral size of the flakes contained in the dispersions, by modifying the parameters of the centrifugation. (*188*, *189*)

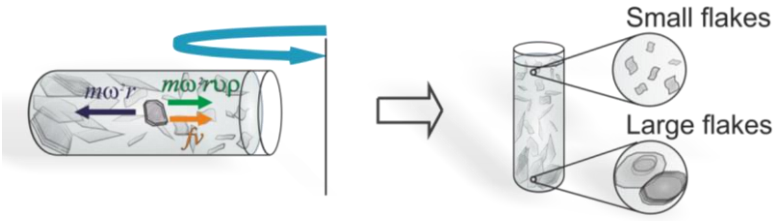

***Figure 12** – Scheme representing the sedimentation based separation mechanism.*

The sedimentation coefficient depends also on the properties of the solvent, as the density ρ_s and the viscosity η_s. The viscosity of the solvent is present in the definition of the friction coefficient, which is expressed by the equation 6.

$$f = 6\pi\, \eta_s r \quad \textit{Equation 6}$$

1.4 Applications of graphene-polymer composites

Graphene is used as a reinforcing filler in the polymer composites (*44*), due to its mechanical properties, *i.e.*, it has a Young's modulus of ~ 1TPa and tensile strength of 130 GPa (*190*). Graphene

nanoplatelets (GnPs) are widely used in industry, due to their commercial availability, and they are a mixture of SLG, FLG, and nanostructured graphite. (*191*)

The graphene-polymer composites are exploited for applications regarding the production of sporting goods (*192*), aerospace (*193*) and automotive fields (*194*). For example, the Company "Head" produce the tennis racket "Graphenext®", which shows superior mechanical properties of and reduced weight of 20 % compared to the conventional tennis racket (**Fig 13a**). (*195*) Instead, the company "Vittoria" produced tires for bicycles containing GnPs, in order to enhance the wet grip and the durability of the product. (*196*) Another market area for the graphene-polymer composites is the the aerospace. In this field, a graphene-polymer composite has been developed for the leading edge in the Airbus 350 in the horizontal tailplane, by a collaboration between Aernnova, Grupo Antolin-Ingegneria and Airbus (**Fig. 13b**). (*197*)

The graphene-polymer composites are also used in applications in which thermal management is needed, *e.g.,* automotive (*194*, *198*) and wearable (*199*, *200*) fields, due to the enhancement of thermal conductivity given by graphene. (*201*) For example, the Ford company is planning to use graphene-based foams for the thermal management in the noisy components of the car, as the fuel rail. (*198*) The thermal conductivity of the graphene-polymer composites have been also exploited to create shoes (Fadel) (**Fig. 13c**) (*199*, *202*) and helmets (Momo design) (**Fig. 13d**) (*200*), based on improving the comfort of the consumer due to the thermoregulation of the composites.

Moreover, due to the lack of permeability of graphene to all the gases, *e.g.,* oxygen (*203*, *204*), the graphene-polymer composites can be potentially used in food (**Fig. 13e**) (*205*) and electronics (**Fig. 13f**) (*206*) packaging.

Other than having excellent mechanical, thermal and gas barrier properties, graphene is an emerging lubricant (*207*), so that it enhances the tribological properties of the matrix (*208*) and it

can be potentially exploited in applications regarding the automotive field, *e.g.,* transmission gears (**Fig. 13g-h**) (*209*, *210*).

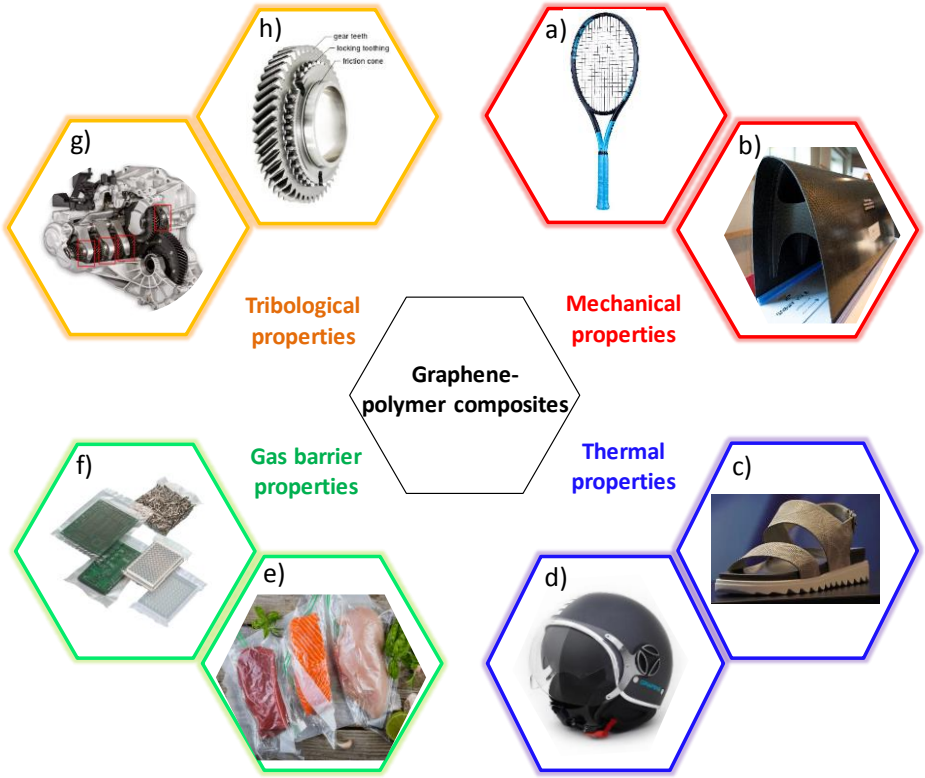

Figure 13 *– Representation of the industrial applications of graphene-polymer composites depending on their properties: a) Graphenext(r) Head tennis racket* (*195*)*, b) leading edge of Airbus350* (*197*)*, c) Fadel shoes* (*199*)*, d) Momo design helmet* (*200*)*, e) food packaging* (*211*)*, f) electronics packaging* (*211*)*, g) example of car engine transmission and h) its gear* (*212*)*.*

1.5 Graphene-polymer composites

The following subchapters describe the graphene-polymer composites features, from the production and the manufacturing methods to the factors influencing the mechanical, thermal, gas barrier and tribological properties.

1.5.1 Production methods

The main production methods of graphene-polymer composites are in-situ polymerization, solution blending and melt blending. (*44*, *213*)

In the *in-situ polymerization* technique, graphene is mixed with the monomer solution in the presence of a catalyst, then the polymerization reaction is started by means of heat (*214–217*) or radiation (**Fig. 14**) (*218–220*). Some examples of graphene-polymer composites fabricated through this method are graphene-polyurethane (PU) (*220*), graphene-polybutylene terephthalate (PBT), graphene-polyethylene (PE) (*215*), graphene-polystyrene (PS) (*216*) and graphene-polypropylene (PP) (*217*). The main advantages of this method are a homogeneous distribution of the filler and the strong interaction formed among the filler and the matrix. (*44*, *213*) These two parameters are important in order to achieve an improvement in the graphene-polymer composite, *e.g.,* thermal properties (*221–223*). The use of solvents is a feature of this method, so that further purification steps are needed for solvent removal. (*44*, *213*)

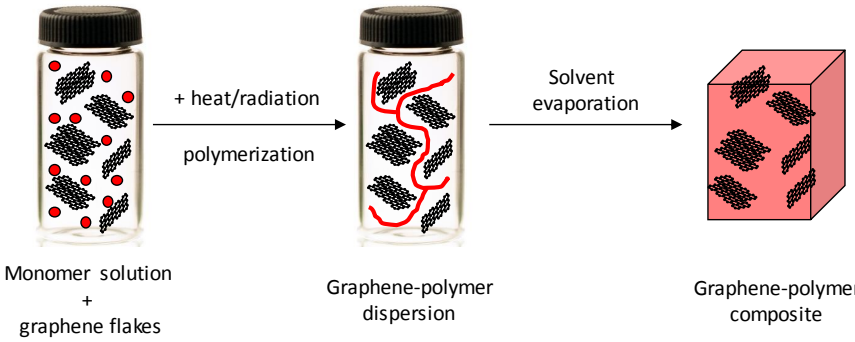

Figure 14 *- Scheme representing the in-situ polymerization process.*

Solution blending is based on mixing the solution of the polymeric matrix with the graphene flakes, in powder form or dispersed in a mutual solvent (**Fig 15**). (*44*, *213*) Subsequently, the solvent is evaporated to obtain the composite. (*44*, *213*) (**Fig 15**). Various polymer matrices have been used to prepare the graphene composites by means of this technique, for example polycarbonate (PC) (*224*), high density PE-ethylene vinyl acetate (HDPE-EVA) (*225*), nylon 6,6 (PA66) (*226*), polyvinyl alcohol (PVA) (*227*), thermoplastic PU (*228*) and PMMA (*229*). Although this technique provides a homogeneous distribution of the filler in the polymeric matrix,

functionalization of the graphene flakes is needed (*225*, *227*). In fact, without functionalization the graphene tend to re-aggregate due to the Van der Waals forces present among the flakes. (*44*, *213*)

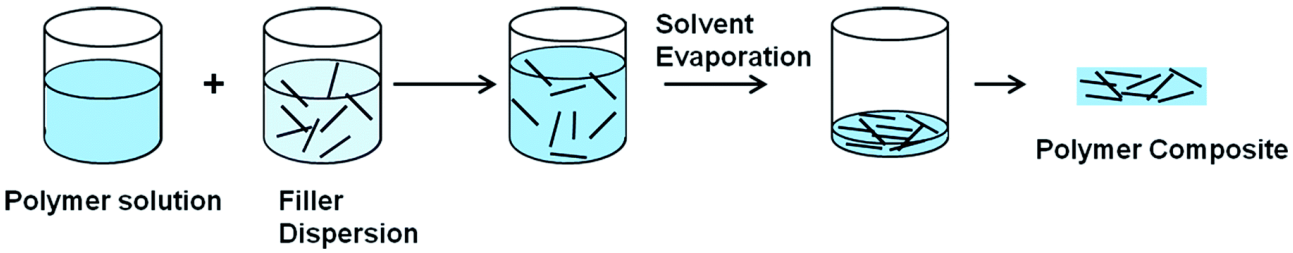

Figure 15 *- Scheme representing the solution blending method* (*230*).

Melt blending is focused on mixing the graphene flakes and the polymer matrix in the molten state (**Fig. 16**). (*44*, *213*) This approach involves the use of instruments that induce shear forces to disperse the filler, *e.g.,* extrusion. (*44*, *213*) For example, the polymer matrices used to prepare the graphene—polymer composites prepared by this process are polylactic acid (PLA) (*231*), poly (ether ether ketone) (PEEK) (*232*), PP (*233*), acrylonitrile-butadiene-styrene (ABS) (*234*) and PE (*235*). However, the shear forces applied during the melt blending, cause the aggregation of the filler and also the reduction of the lateral size (*235–237*), which are detrimental for the properties of the composites, *e.g.,* mechanical (*238–242*). Melt blending does not need the involvement of solvents (*243*) and it is compatible with other industrial processes, *e.g.,* injection moulding (*244*).

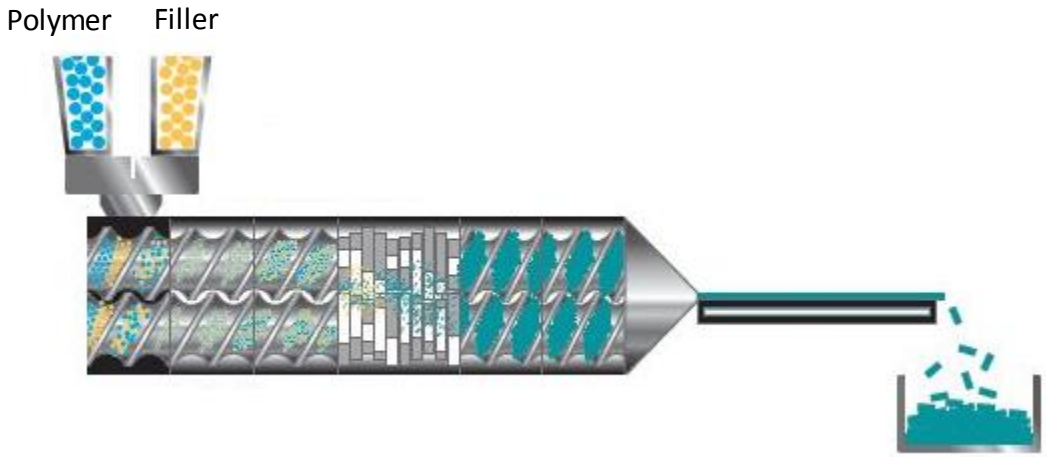

Figure 16 *- Scheme representing melt blending process (extrusion)* (*245*).

1.5.2 Manufacturing methods

Subsequently to the preparation of the graphene-polymer composites, samples are prepared in the desired shape and dimension through manufacturing techniques, *e.g.,* injection moulding, compression moulding and 3D printing.

The *injection moulding* process starts with the melting of the composite, which is then pushed into a mould (**Fig. 17**). (*246*) This technique is used to create a great variety of objects, from bottle caps to automotive dashboards. (*247*) The advantages of injection moulding with respect to the other industrial manufacturing methods are related to its repeatability and its high production rates. (*246*) While, the main drawbacks regards the mould, as every new object to be manufactured needs a new design mould. (*246*) In literature (*232*, *236*, *248*–*252*), there are various graphene-polymer composites manufactured using this process, *e.g.,* graphene-PA6 (*236*), graphene-PP (*248*), graphene-PEEK (*232*), etc. The orientation of the graphene flakes in the matrix is affected by this method, as the filler aligns along the flow direction during the injection of the molten composite into the mould, influencing the properties of the final composites, *e.g.,* mechanical. (*248*, *249*)

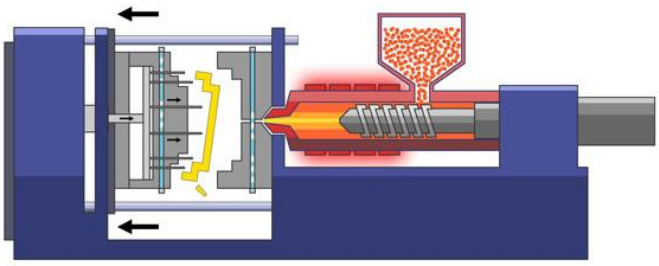

Figure 17 *– Scheme of the injection moulding process* (*253*)*.*

The *compression moulding* method consists in placing the composites pellets in a preheated mould, at a temperature between the glass transition temperature and the melting temperature of the matrix (**Fig. 18**). (*254*) Then, a high-pressure is applied through a hydraulic press, squeezing the

molten composite, until it fills the whole volume of the mould (**Fig. 18**). (*254*) This technique is used to produce components in the automotive field, *e.g.,* body panels and automatic transmission components. (*254*) However, the compression moulding has some issues linked with the lack of homogeneity and pitting, compared to the injection moulding. (*254*) Examples of graphene-polymer composites prepared using this technique are graphene-linear low-density polyethene (LLPE) (*255*) and graphene-polyamide 12 (PA12) (*256*). Moreover, contrary to injection moulding technique, the graphene flakes do not follow a particular alignment, being randomly oriented. (*248*, *249*) The random alignment of the graphene flakes can affect the final properties of the graphene-polymer composite, e.g. thermal properties. (*257*)

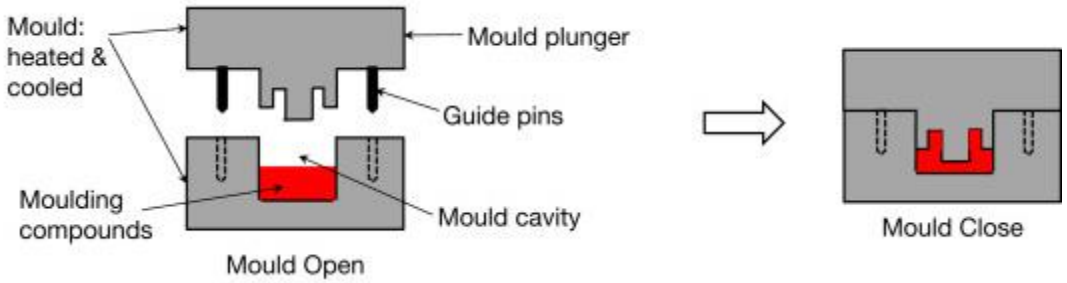

Figure 18 *- Scheme of the compression moulding process* (*258*).

3D printing is a class of techniques based on the building of an object layer by layer, and for this peculiarity it is called additive manufacturing. (*259*) Unlike traditional manufacturing processes, *e.g.,* injection moulding, 3D printing does not need additional tools, *e.g.,* moulds, for the creation of a new design. (*260–262*) This manufacturing technique is able to produce complex structures formed by different components in one step, without any further assembly processes. (*260–262*) Moreover, 3D printing uses just the precise amount of material needed to create the final product, reducing the production waste. (*260–262*) Among all the 3D printing techniques (*259*), as selective laser sintering (SLS), stereolithography (SLA), etc., fused deposition modelling (FDM) is used for

thermoplastics and it is compatible with the extrusion method, since the material must be in a filament shape to be printed. (*263*) In FDM, the sample is formed by depositing "roads" of molten polymer on a support along the x-y plane, while the support lowers on the z direction (**Fig. 19a**). (*263*) The "roads" can be printed in the desired direction, following a defined raster orientation (**Fig. 19b**). (*263*) 3D printed graphene-polymer composites have been manufacturing using as polymer matrices ABS (*264*, *265*), PA12 (*257*), PBT (*266*) and PLA (*267*). Furthermore, as the graphene flakes tend to align along the extrusion direction (**Fig. 19c**), the properties of the composites tend to be anisotropic, depending on the raster orientation of the printed roads. (*257*, *264–267*)

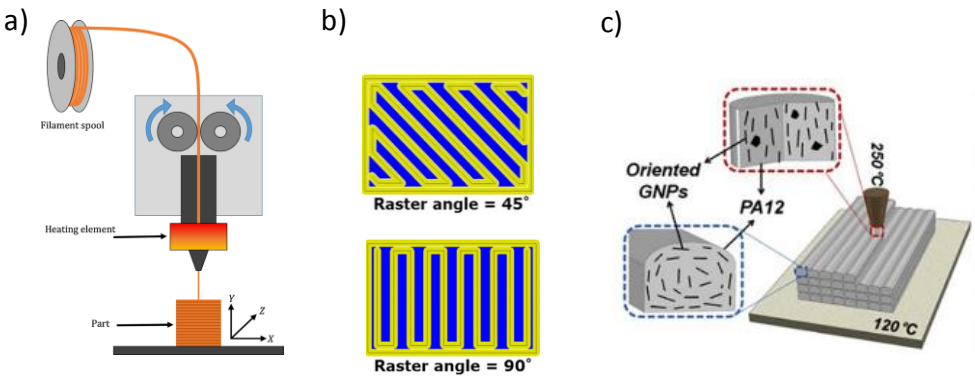

Figure 19 *- a) Scheme of the FDM process* (*268*)*, b) Two possible printing direction with raster angle at 45° and 90°* (*269*)*, b) alignment of the graphene flakes (GNPs) along the printing direction in polyamide 12 (PA12)* (*257*)*.*

1.5.3 Mechanical properties

The improvement of mechanical properties in graphene-polymer composites with respect to the pristine polymer is based on the stress transfer from the matrix to the filler, during the application of the tensile load on the composite. (*44*, *270*) The effectiveness of the stress transfer is influenced by factors as i) the aspect ratio (AR) of the flakes, defined as the length over thickness of the filler, ii) the orientation of the filler with respect to the applied stress, iii) the distribution in the matrix of the flakes and iv) the interface between the matrix and the filler (**Fig. 20**). (*44*, *270*)

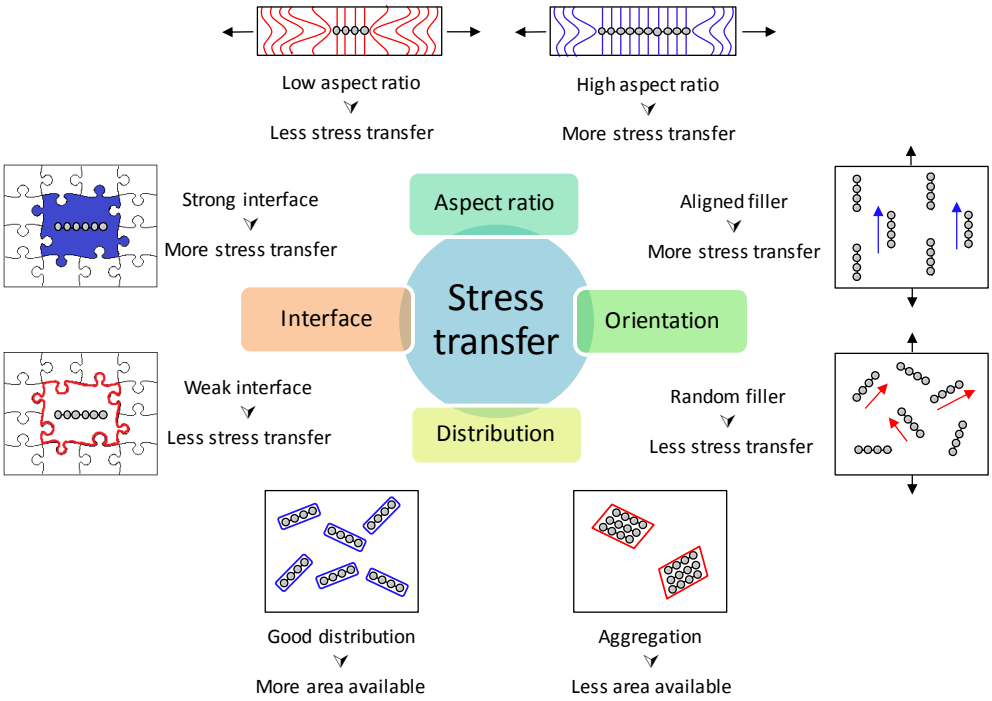

Figure 20 *- Scheme of the main factors influencing the stress transfer from the matrix to the filler for the improvement of the mechanical properties.*

In literature (*238–242*), the AR of the flakes influences the reinforcing effect of the filler. For example, Gao et al. (*240*) prepared PLA composites with two different types of GnPs, GnPs-C750 and GnPs-M15 having an AR of 750 and 2000, respectively. The tensile test shows that Young's modulus has an increase of 30 % and 56 %, compared to the pristine PLA, for the flakes GnPs-C750 and GnPs-M15, accordingly, at the same loading of filler. (*240*) The flakes GnPs-M15, AR = 2000, have a higher reinforcing effect compared to the one achieved with the use of the flakes GnPs-C750, AR = 750. This phenomenon is due to the fact that if there is a larger area of the filler available for the stress transfer, then the stress is transferred more efficiently from the polymer matrix to the filler. (*240*)

The orientation of the graphene flakes with respect to the applied stress plays a crucial role in improving the mechanical properties. (*249*, *257*, *270*, *271*) The effect of the orientation on the mechanical properties is highlighted in a study, where graphene-PA12 composites is prepared by using compression moulding and FDM. (*257*) The 3D printed sample has a raster angle of 0°, having

the printed roads parallel to the direction of the applied tensile stress. (*257*) The compression moulded and FDM samples have an improvement in the Young's modulus of 40 % and 50 %, respectively, compared to the pristine PA12. (*257*) The FDM samples present a better mechanical performance compared to the compression moulded samples, due to the graphene flakes orientation. (*257*) In fact, the graphene flakes are randomly oriented in the compression moulded samples, while they are aligned along the testing direction in the FDM samples, maximizing the stress transfer. (*257*)

The distribution of the graphene flakes is fundamental to achieve an enhancement in the mechanical properties, as agglomerates decrease the available area for the stress transfer. (*255*, *272*, *273*) The effect of distribution on the mechanical properties of the graphene-LLPE composites is analysed, by producing the composite through extrusion but using two different mixing velocities, 100 rpm and 150 rpm. (*255*) The mechanical characterization of the composites shows that the tensile strength presents an improvement of 47 %, with respect to the polymer matrix, in the composite prepared using 150 rpm (4 wt % of loading). (*255*) Instead, the composite, containing the same amount of filler but produced at 100 rpm, shows no changes for the mechanical properties. (*255*) The different mechanical performance is attributed to the flakes distribution achieved by using a higher mixing speed, *i.e.,* 150 rpm, which allows to break down the agglomerates of the graphene flakes. (*255*)

Moreover, the stress transfer is promoted by a strong interface between the matrix and the filler. (*274–276*) The strong interface is provided by the surface modification of the graphene flakes, *e.g.,* introduction of carbonyl, hydroxyl and carboxyl groups on the surface of graphene (*274–276*), which allows the flakes to bind with the polymer. (*274–276*) The functionalization of the graphene flakes also allows achieving a homogeneous distribution of the flakes. (*277*)

For examples, in order to produce GnPs-PU composites, GnPs are functionalized with hydroxyl and carbonyl groups, *i.e.,* f-GnPs-PU, so that a covalent bond is formed with the PU matrix. (*274*) The prepared composites were then compared with GnPs-PU samples produced with un-treated GnPs, *i.e.,* GnPs-PU, presenting a weak bond with the polymer matrix. (*274*) The Young's modulus presented enhancements of 840 % and 660 % for the composites f-GnPs-PU and GnPs-PU, accordingly, compared with the pristine matrix. (*274*) The f-GnPs-PU had a better mechanical performance due to the strong interface between the filler and the polymer. (*274*)

1.5.4 Thermal properties

The high thermal conductivity of graphene, *i.e.,* 2000-4000 W $m^{-1}K^{-1}$ (*57*, *58*), is due to its crystalline and ordered structure, as the heat propagates quickly through the lattice. (*278*, *279*) In the case of polymers, the transfer of the heat through the atoms is slower compared to graphene, as the amorphous or semi-crystalline structure of the polymers causes phonon scattering. (*280*) In the graphene-polymer composites, the main factors affecting the heat transfer are: i) the AR of the graphene flakes, ii) the orientation of the flakes, iii) the thermal path among the flakes and iv) the interface between the filler and the matrix (**Fig. 21**). (*281*)

The AR of the flakes is important, as, at the same loading, flakes which present a higher AR can cover a longer distance in the polymer matrix, compared to low AR flakes, so that the heat can transfer more easily. (*282–284*) The influence of the AR on the heat transfer is clearly observed in the GnPs-PP composites prepared by Ajorloo et al. (*283*). Two different types of GnPs, EC1500 and EC100, having an AR of 700 and 100000, respectively, are used. The thermal conductivity increases of 17 % and 120 % for the composites produced with EC1500 and EC100, accordingly, with respect to the pristine PP. (*283*) These results highlight that using GnPs with a high AR is helpful to promote heat transfer. (*283*)

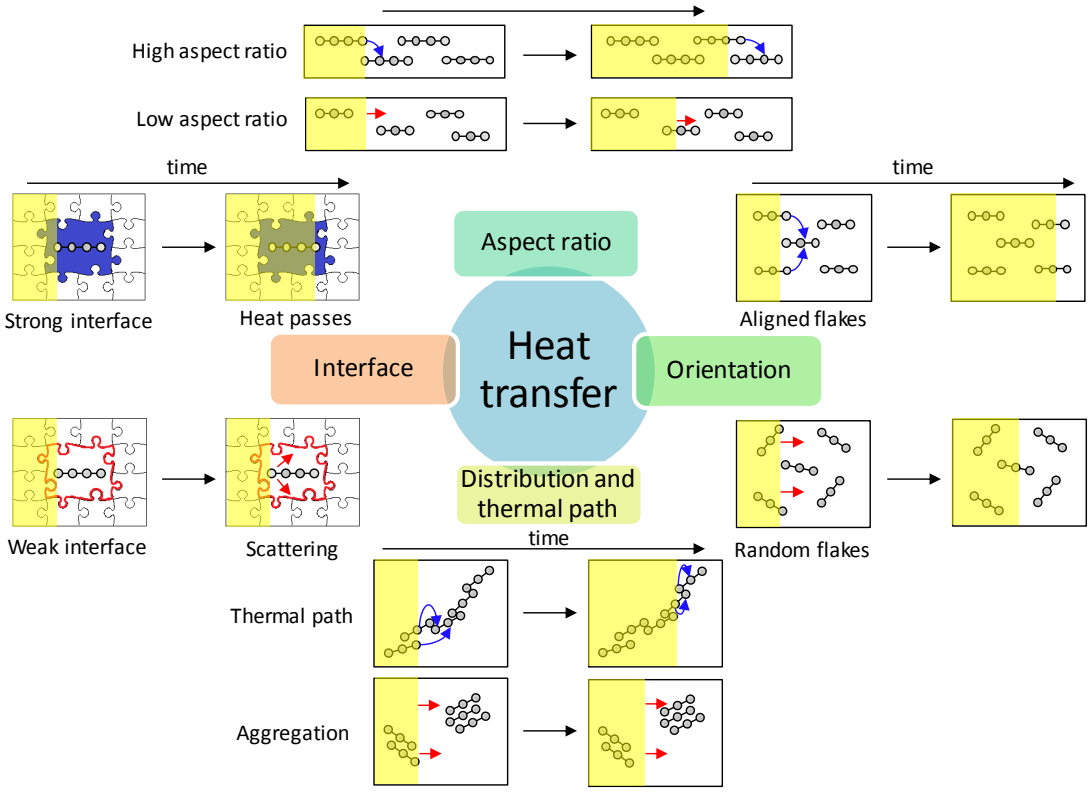

Figure 21 *- Scheme of the factors influencing the heat transfer in the graphene-polymer composites.*

The orientation of the filler inside the polymer composite is affecting the direction and the efficiency of the thermal propagation. (*257*, *285*, *286*) The heat propagates into the matrix following the orientation of the filler. (*257*, *285*, *286*) Therefore, if the filler is oriented along the direction of the heat propagation, the heat transfer is more efficient than when the filler is randomly oriented. (*257*, *285*, *286*)

The effect of orientation on the heat transfer is tested on graphene-PA12 composites manufactured using compression moulding and FDM, using a printing direction parallel to the testing direction used to measure the thermal conductivity. (*257*) The compression moulded sample and the FDM sample show an increase of 50 % and 250 %, respectively, in the thermal conductivity compared to the bare polymer.(*257*) The difference of the thermal performance is due to the graphene flakes orientation in the matrix. (*257*) In fact, graphene flakes are randomly oriented in the compression

moulded sample, while in the FDM sample, the flakes are aligned along the direction used to test the thermal conductivity, allowing the thermal transfer to be optimised. (*257*)

A homogeneous distribution of the flakes in the matrix and a thermal path, formed by graphene flakes, are necessary to reduce the phonon scattering at the interface between the filler and the matrix, promoting the passage of the heat through the polymer. (*223*, *255*, *287*)

Graphene-PP composites are produced by Xu et al. (*287*) to test the effect of the size of the graphene flakes on the thermal conductivity. They used as fillers the flakes "KNG180", with an AR of 500, and the flakes "G5", having an AR of 1000. (*287*) The thermal conductivity measurements reveal that the composites made with G5 have an increment, which is 100 % larger with respect to the composites prepared with KNG180. (*287*) Apart from the AR effect, the authors observed a less homogeneous distribution of the KNG180 flakes compared to the G5 flakes, creating polymer-filler interfaces, thus hindering the heat transfer. (*287*)

A weak interface between the polymer and the graphene flakes, *i.e.,* no bonding, causes phonon scattering, introducing thermal resistance and hindering the heat transfer. (*221*, *222*, *274*, *288*) Instead, a strong interface promotes the propagation of the heat and it can be achieved by functionalizing the graphene flakes. (*221*, *222*, *274*, *288*)

The importance of the interface in achieving an improvement in the thermal conductivity is shown in a study where ABS composites are prepared with different carbonaceous fillers, as micronised graphite (G-1.5 μm) and carboxylated functionalized MLG. (*288*) The best results in terms of thermal conductivity are obtained using 15 wt% in the loading of MLG, achieving an increment of 200 % compared to the pristine ABS. (*288*) This improvement is attributed to the functionalization of the filler, which enhances both the interaction between the filler and the matrix and its distribution. (*288*)

1.5.5 Gas barrier properties

Graphene is used in polymer composites to enhance the gas barrier properties, due to its lack of permeability to the gases, *e.g.,* oxygen, carbon dioxide (*203*). In polymer composites, graphene makes the gas molecules following a longer and more tortuous pathway to cross the matrix. (*289*) The factors which play an important role in the improvement of the gas barrier properties are i) the AR, ii) the distribution and iii) the orientation of the filler (**Fig. 22**). (*289*)

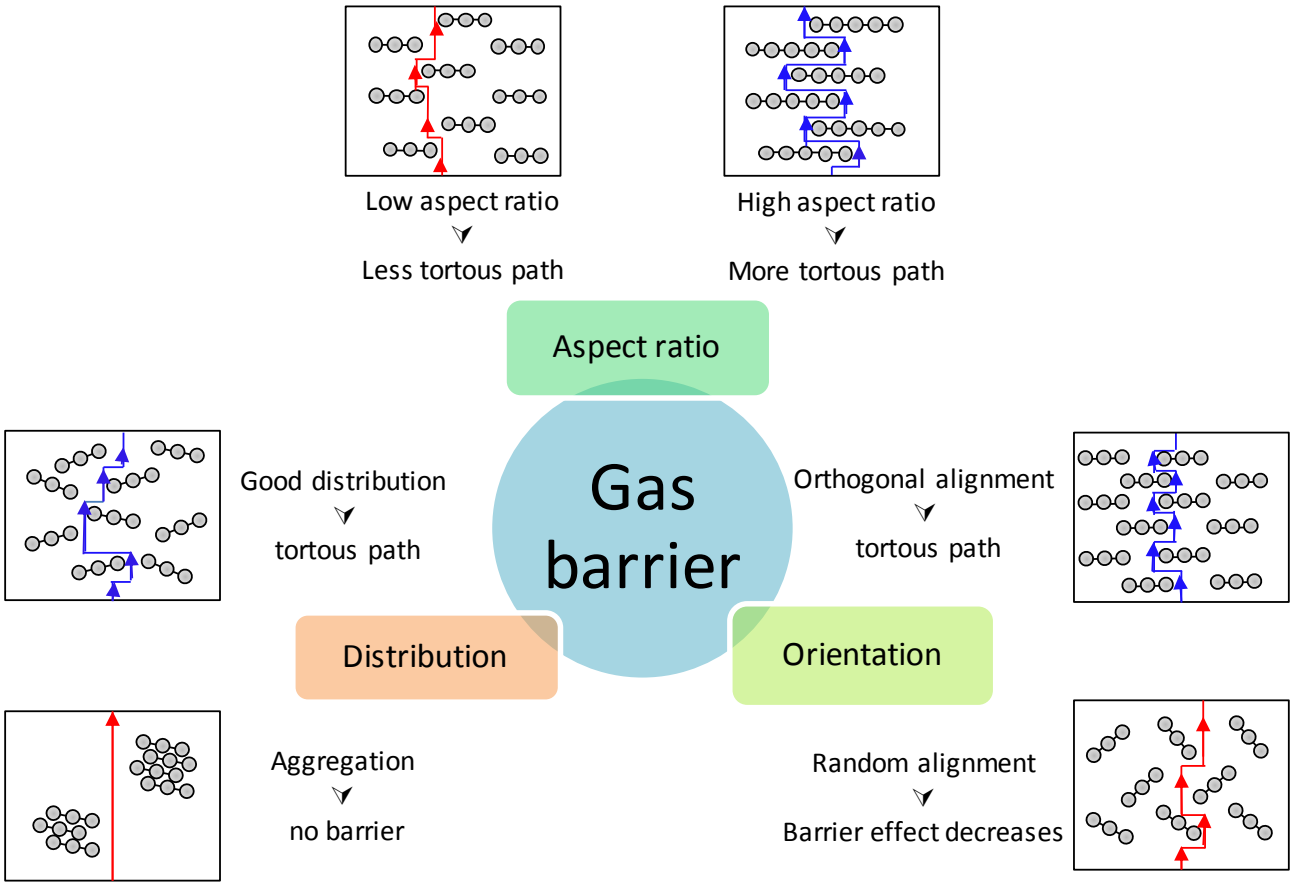

Figure 22 *- Scheme presenting the factors influencing the gas barrier properties of the graphene-polymer composites*

An AR as high as possible is desirable to increase the gas path through the matrix. (*250*, *290*, *291*) In fact, a study on graphene-PC composites prepared with fillers having different AR shows a marked difference on the results of the oxygen permeability. (*290*) The used fillers are "Single-layer

graphene-ACS material®" (SLG-ACS) with AR equal to 16500 and "GNPs grade 3 cheap tubes®" (GNPs3) with AR around 250. At equal loading of filler, the oxygen permeability decreases of 41 % and 10 % in the composites prepared with SLG-ACS and GNPs3, respectively, compared to the pristine PC. (*290*) This result indicates that the gas permeability depends on the length of the tortuous diffusion paths, which increases with the AR of the filler. (*290*)

If the orientation of the filler is orthogonal to the direction used to test the gas permeability, the efficiency of the graphene flakes as a gas barrier is improved, while it decreases if the flakes present a random alignment. (*271*, *289*, *292*) A fitting example of the influence of the filler orientation on the gas permeability is shown in a study of the water vapour permeability of graphene-PLA composites produced through a technique called "co-extrusion". (*271*) Co-extrusion allows the fabrication of samples having alternating layers of pristine polymer with layers of graphene-polymer composites. (*271*) The authors prepared samples with a ratio of pristine polymer layers over composite layers of 50:50 and 90:10, *i.e.,* 90 % of pristine polymer layers and 10 % of composite layers. (*271*) The morphological analysis of these samples has shown that the graphene flakes increase their alignment along the extrusion direction, due to geometric constraints, as the thickness of the composite layers decreases passing from 50:50 to 90:10 (Fig. 23). (*271*) The alignment of the filler causes a better gas barrier performance, as the water vapour permeability decreases of 45 % in the 50:50 sample and 53 % in the 90:10 sample compared to the unloaded PLA. (*271*)

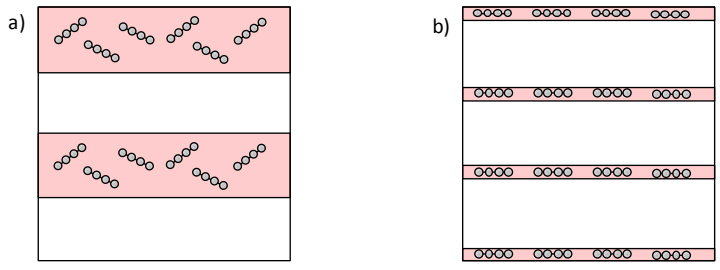

Figure 23 *- Scheme of the composites a) 50:50 and b) 90:10.*

Moreover, the aggregation of the filler is detrimental for the formation of a tortuous path, as the amount of flakes per unit volume decreases. (*293*, *294*) The effect of aggregation on the oxygen permeability is shown in graphene-PA12 composites using a loading of graphene flakes of 0.1, 0.3, 0.6, 1.0 and 3.0 wt %. (*294*) The graphene-PA12 composites have a decrease in the oxygen permeability of 32 % at a loading of 0.6 wt %, compared to the pristine matrix. But, when the loading reaches 3.0 wt %, the oxygen permeability has a drop of only 11 % with respect to the PA12. This result is attributed to the aggregation of the filler, occurring as the loading overcomes the 0.6 wt %.

1.5.6 Tribological properties

The two main tribological phenomena of polymers and polymer composites are friction and wear (*295*). Friction is defined as the resistance of the polymer surface to the sliding motion of a rubbing counterpart (*296*). In the case of graphene-polymer composites, it decreases with loading due to the lubricant action of the graphene flakes (*232*, *297–299*). Wear is defined as the volume loss of a sample, due to the extensive sliding by a second surface and it is measured by scratching the surface of a sample on a defined length with a metal counterpart, over an arbitrary number of cycles. (*300*, *301*) The main wear mechanism occurring in polymers consists of the transfer of a polymer film from the surface of the sample to the rubbing counterpart. (*300*, *301*) The surface of the polymer gets consumed producing debris along the sliding path. (*300*, *301*) In graphene-polymer composites, the graphene flakes form a protective layer both on the surface of the rubbing counterpart and of the sample, hindering the wear. (*232*, *297–299*) One of the main factor influencing the formation of the protective layer is the distribution of the graphene flakes in the matrix. (*298*, *302*) A homogeneous distribution of the flakes in the matrix is necessary to form the protective layer (**Fig. 24**). (*298*, *302*) Aggregates are pulled out from the surface of the composite during the sliding and act as an abrasive body against both the sample and the rubbing counterpart (**Fig. 24**). (*298*, *302*) For example, graphene-HDPE composites using GnPs and GnPs functionalized

with octadecyltrimethoxysilane (ODMS) (fGNPs). (*302*) The authors measured the wear rate of the composites, which gives an indication of the consumed volume of the surface of the sample over time, during the wear testing. (*302*) The composite containing fGnPs have a decrease of 60 % in the wear rate compared to the pristine HDPE. (*302*) While, the wear rate increases of 170 %, with respect to the unloaded matrix, in the case of the composite with the GnP's filler. (*302*) These results are due to the different distribution of the graphene flakes, as fGnPs are homogeneously distributed thanks to the functionalization, allowing the formation of the protective layer. (*302*)

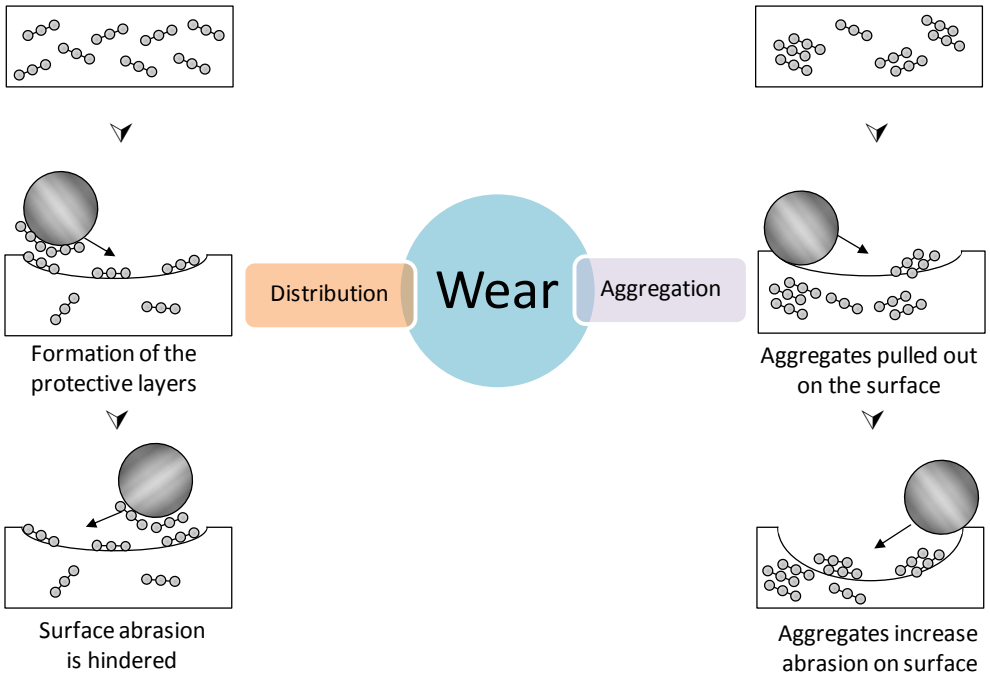

Figure 24 *- Schemes representing the wear of graphene-polymer composites in case the filler is homogenously distributed (distribution) or there are aggregates (aggregation).*

1.6 Conclusions

Graphene is exploited as filler to produce graphene-polymer composites, in order to improve the mechanical, thermal, gas barrier and tribological properties of the polymer matrix (*44*). These properties can be obtained by considering factors as the aspect ratio and the distribution of the graphene flakes in the matrix. (*223*, *238–242*, *250*, *255*, *272*, *273*, *282–284*, *287*, *290*, *291*, *293*, *294*) Plus it is possible to tune the properties, *e.g.,* mechanical, thermal and gas barrier, by changing the

orientation of the filler in the matrix, through the different manufacturing methods. (*249*, *257*, *270*, *271*, *285*, *286*, *289*, *292*) The advantage of using graphene-polymer composites regards the ability of graphene to enhance more than one property simultaneously, giving rise to multifunctional materials (*44*). For example, a graphene-polymer composite, that possesses mechanical strength and dissipates heat, can be used for many applications in wearables, *e.g.,* Momo design helmet (*200*) and Fadel shoes (*199*), and in automotive, *e.g.,* Ford is developing graphene-based foams for thermal management of noisy components (*198*).

Chapter 2: Experimental methods and characterisation techniques

In the following paragraphs, the basic concepts and the experimental procedures concerning the solution processing of graphene by means of the ultra-sonication and WJM approaches will be introduced.

Firstly, the experimental details regarding the characterization techniques used to analyse the as-produced graphene dispersions are presented. In detail, the number of layers, the doping and the defects of the graphene-based flakes present in the as-produced dispersions are studied by using Raman spectroscopy. Instead, the thickness of the graphene-based flakes is evaluated by AFM. Transmission electron microscopy (TEM) is used to measure the lateral size of the graphene-based flakes. Three different techniques are used to obtain the concentration of the graphene dispersions, vacuum filtration, optical absorption spectroscopy (OAS) and thermogravimetric analysis (TGA). Finally, the viscosity and the surface tension of the graphene dispersions are evaluated using rheological measurements and the contact angle technique, accordingly.

2.1 Materials

Natural graphite flakes (+100 mesh) and acetone (ACS reagent, ≥99.5 %) are purchased from Merck, PMMA powder (molecular weight 550000) from Alfa Aesar, ABS pellets (Terluran® GP22) from Ineos Styrosolution. The solvents NMP (Reagent Plus, purity ≥ 99 %), acetone (ACS Reagent, purity ≥ 99.5 %), DMSO (ACS Reagent, purity ≥ 99.9 %) are purchased from Sigma Aldrich. Polyamide 6 (PA, Akulon F223-D) is received by DSM. The styrene-butadiene copolymer (SB) (Sofprene T 5402.A63) is purchased from the So.F.teR. company. All these materials are used without any further purification.

2.2 Production of graphene dispersions by liquid-phase exfoliation

The graphene dispersions are produced by using two techniques: ultrasonication based liquid-phase exfoliation and WJM.

2.2.1 Ultrasonication based liquid phase exfoliation

2.2.1.1 Exfoliation of graphite in acetone and acetone-poly methyl methacrylate (PMMA) mixture

The use of solvents with low boiling point and the use of stabilisers with a polymeric nature are preferred, as stated in Chapter 1, for the development of the first part of the Thesis work. In this regard, graphite (0.50 g) is dispersed in i) acetone (0.05 L) and ii) in an acetone-PMMA mixture (0.05 L) containing 1 wt % of PMMA with respect to acetone, in glass vials. The graphite flakes are then exfoliated using an ultrasonic bath (VWR-Ultrasonic cleaner USC-THD) for 6 hours at a temperature in a range between 25 °C and 35 °C. The exfoliated graphite dispersions are labelled FLG_{US} (samples in acetone without PMMA). The dispersions containing 1 wt % PMMA are labelled FLG-$PMMA_{US}$. The dispersions FLG_{US} and FLG-$PMMA_{US}$ are both centrifuged using a Beckman Coulter Optima XE-90 Ultracentrifuge (SW32Ti rotor). Three centrifugal accelerations are chosen, *i.e.* ~200 *g* (gravitational acceleration corresponding to 1000 rpm), 4300 *g* (5000 rpm) and 17000 *g* (10000 rpm) for 30 min. Then, 80 % of the supernatant is collected after the centrifugation, discarding the precipitate.

2.2.1.2 Exfoliation of graphite in N-methyl pyrrolidone (NMP)

Graphite (0.50 g) is dispersed in 50 mL of NMP and exfoliated by ultra-sonication (sonic bath VWR-Ultrasonic cleaner USC-THD) for 6 hours, using a temperature range of 25 °C - 35 °C. The SBS process is performed on the so-produced dispersion using different centrifugal accelerations, *i.e.,* 170 g, 1000 g, 4250 g, 9500 g, 17000 g. Moreover, cascade ultra-centrifugations are carried out, in

order to further tune the morphology of the exfoliated graphite flakes. (*303*) The exfoliated graphite dispersion, obtained from the centrifugation at 170 g, is centrifuged at 4250 g and the supernatant is collected. Afterwards, the supernatant is centrifuged at 170 g, and then a second, and a third 170g centrifugation steps are added, collecting supernatant at each step. **Table** 2 reports the nomenclature used for the exfoliated dispersions produced using different ultracentrifugation steps.

Table 2 *- Name of the dispersions with the corresponding ultracentrifugation parameters.*

Name	Centrifugation treatment
FLG-1	170 g (one step)
FLG-2	1000 g (one step)
FLG-3	4250 g (one step)
FLG-4	9500 g (one step)
FLG-5	17000 g (one step)
FLG-6	170 g-4250 g-170 g (three steps)
FLG-7	170 g-4250 g-170 g-170 g (four steps)
FLG-8	170 g-4250 g-170 g-170 g-170 g (five steps)

2.2.2 Wet jet milling based exfoliation

A dispersion of NMP (20 L) and natural graphite flakes (200 gr) is prepared by mixing them with a mechanical stirrer (Eurostar digital Ika Werke). Subsequently, a wet jet mill instrument (Jokoh JN100) is used to process the dispersion, a description of the WJM set up and the overall process are described in Chapter 1. During the processing step, the NMP-graphite dispersion is passed through a nozzle, whose diameter is reduced from 0.3 mm to 0.1 mm at each cycle. The obtained dispersion, named "FLG_{WJM}", is then transferred to a rotary evaporator (Hei-Vap industrial, Heidolph at a temperature, *T*, around 80 °C and a pressure, *P*, of ~ 5 mbar) to remove the NMP. Subsequently, DMSO is added to the dry powder previously dispersed in acetone and the solvent is removed using freeze-drying (Alpha 2-4 LSC, Martin Christ).

2.3 Characterization of the graphene dispersions

The as-produced graphene dispersions are characterized by means of Raman spectroscopy, AFM and TEM. The concentration of the graphene dispersions is evaluated by vacuum filtration, TGA and OAS.

2.3.1 Raman spectroscopy

Raman spectroscopy is a useful tool for the characterization of the graphene flakes, it allows to obtain information about defects, doping, strain of the flakes and get an indication of the number of layers. (*304*, *305*) The Raman spectra of the graphene dispersions are collected using a Renishaw inVia confocal Raman microscope using an excitation line of 514.5 nm (2.41 eV) with a 100× objective lens, and an incident power of 1 mW on the samples. The peaks are fitted with Lorentzian functions and 15 spectra are analysed for each sample. The as-prepared exfoliated graphite dispersions are drop-cast onto a Si/SiO_2 wafer (LDB Technologies Ltd.) and dried under vacuum.

2.3.1.1 Description of the graphene spectrum

The characteristic peaks of the Raman spectrum of graphene are G, D and the 2D (**Fig. 25**). (*304*, *305*) The G peak corresponds to the E_{2g} phonon at the Brillouin zone centre and it is located at ~ 1585 cm^{-1} for excitation energy of 2.41 eV. (*304*, *305*) The D peak is due to the breathing modes of the sp^2 hybridized carbon rings and it requires the breaking on the carbon-ring symmetry for its activation by double resonance. (*306*) The 2D peak is centred at ~ 2680 cm^{-1} for an excitation energy of 2.41 eV in case of single-layer graphene and it is an overtone of the D band. (*304*, *305*)

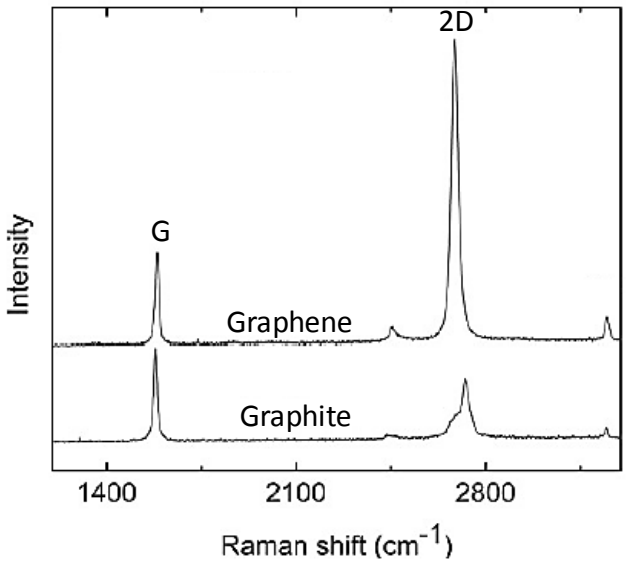

Figure 25 *- Raman spectra of graphene and graphite* (*307*)*.*

2.3.1.2 Defects

Graphene has mainly two types of defects, the zero-dimensional defects, *e.g.,* vacancies, interstitial atoms, etc., and one-dimensional defects, *e.g.,* tilt boundaries separating two domains of different lattice orientations. (*308*) Raman spectroscopy allows recognizing if the defects of graphene flakes are mainly located on the edges or on the basal plane. (*306*) Basal plane defects negatively affect the properties of graphene, *e.g.* mechanical properties (*309*, *310*). The intensity ratio of the D peak over the G peak, (I(D)/I(G)), increases with the quantity of defects, (*311*, *312*) but the latter parameter alone cannot discriminate between edge and basal plane defects. (*313*) The full-width half maximum of the G peak, (FWHM(G)), is shown to raise with bulk disorder, while it does not change when the defects are located on the edges (*313*, *314*). Therefore, bulk defects are present when there is a correlation between I(D)/I(G) and FWHM(G) (**Fig. 26a**). (*313*) On the contrary, if these two parameters do not show any correlation, the defects are mainly located at the edges of the flakes (**Fig. 26b**). (*313*) The same trend is occurring between the area ratio of the D peak over the G peak (A(D)/A(G)) and FWHM(G). (*313*)

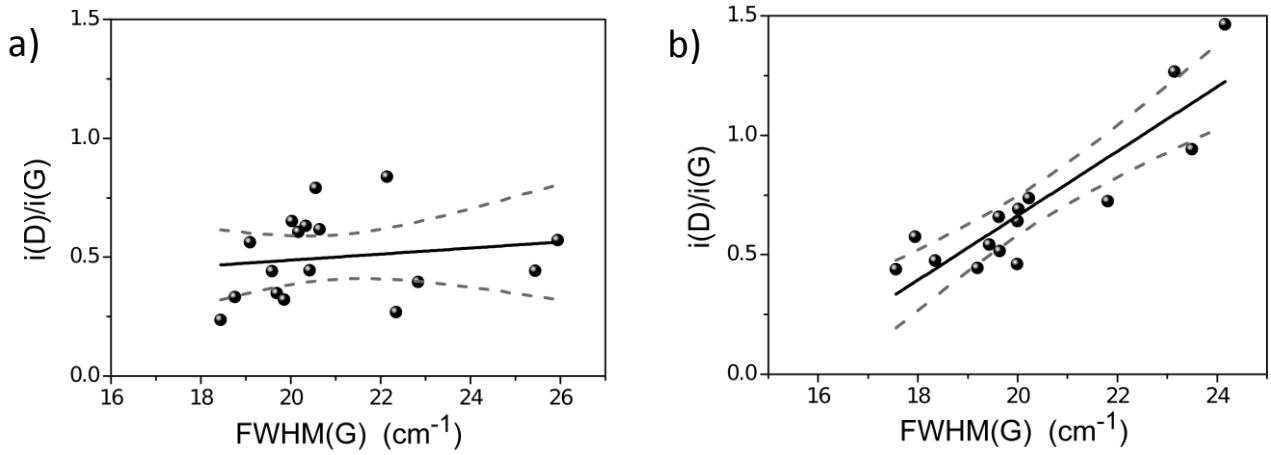

Figure 26 *- Examples of samples where the defects are mainly concentrated a) on the edges (no correlation), b) on the basal plane (linear correlation).* (*313*)

2.3.1.3 Doping

The liquid phase exfoliation of graphite carried out with the aid of surfactants or polymers may lead to the doping of the graphene flakes. (*315–317*) Doping affects the charge carriers concentration, *i.e.,* holes and electrons, and, as a consequence, also the Fermi level of graphene. (*306*) In pristine graphene, the Fermi level is located at the Dirac point (**Fig. 27a**). (*306*) A p-doping causes an increase in the concentration of holes so that the Fermi level shifts below the Dirac point (**Fig. 27a**). (*306*) Instead, an n-doping brings to a rise in the concentration of electrons and the Fermi level is pushed above the Dirac point (**Fig. 27a**). (*306*) The G and 2D peaks are influenced by the changes in the carrier concentration. (*306*) The position of the G peak (Pos(G)) increases (**Fig. 27b**) and the FWHM(G) decreases (**Fig. 27c**), when there is n- and p-doping. (*306*) The position of the 2D peak (Pos(2D)) up-shifts (**Fig. 27d**) when the flakes have a p-doping and it down-shifts when the flakes are n-doped, compared to un-doped graphene flakes. (*306*)

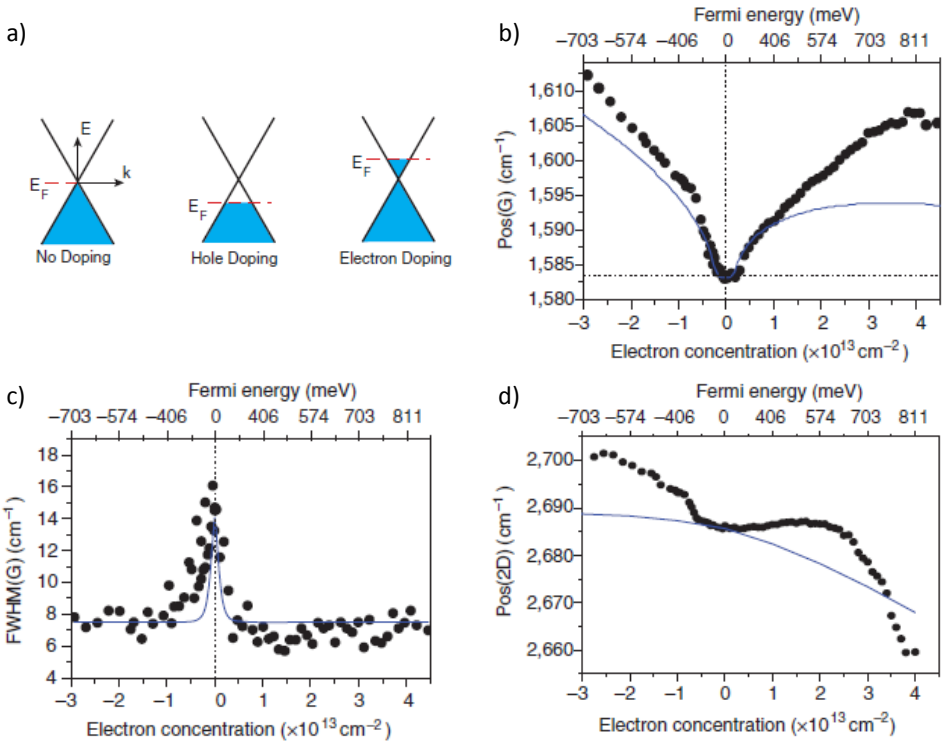

Figure 27 *- a) Scheme of the Fermi level position for no doping, p-doping (hole) and n-doping (electron), the effect of doping on b)Pos(G), c) FWHM(G) and d) Pos(2D).* (*306*)

2.3.1.4 Number of layers

The number of layers of the graphene flakes affects the 2D peak, which is a superposition of multiple components, the main being $2D_1$ and $2D_2$. In graphite, the intensity of the component $2D_1$, -$I(2D_1)$-, is roughly half of the intensity of component $2D_2$, -$I(2D_2)$-. (*305*, *318*) The $I(2D_1)$ increases and the $I(2D_2)$ decreases, with the thickness reduction, *i.e.*, passing from graphitic flakes (number of layers > 10) to MLG (number of layers between 5 and 9) and FLG (number of layers < 5) flakes (**Fig. 28a**). It is possible to discriminate between FLG flakes or SLG by expressing the normalized intensity ratio $I(2D_1)/I(G)$ as function of $I(2D_2)/I(G)$ (**Fig. 28b**). The dashed line represents the condition corresponding to the MLG [$I(2D_1)/I(G) = I(2D_2)/I(G)$], while the points positioned below the line [$I(2D_1)/I(G) < I(2D_2)/I(G)$] represent the graphitic flakes (**Fig. 28b**). (*318–320*) The FLG flakes are above the dashed line, [$I(2D_1)/I(G) > I(2D_2)/I(G)$] (**Fig. 28b**), while SLGs are located on the Y axis, representing the condition where no $I(2D_2)$ is present. (*318–320*)

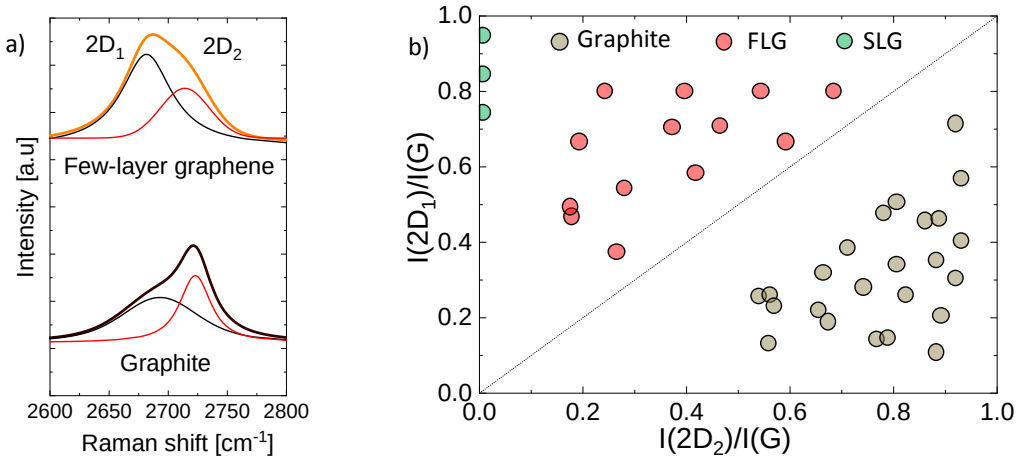

Figure 28 *- a) Effect of the decreasing of the number of layers on the components $I(2D_1)$ and $I(2D_2)$ (154), b) scheme representing the discrimination of graphitic flakes (grey), MLG (blue) and FLG (red) expressing the $I(2D_1)/I(G)$ in function of $I(2D_2)/I(G)$.*

2.3.2. Atomic force microscopy (AFM)

The AFM enables the estimation of the number of layers by measuring the height of the flakes and dividing by the graphite interlayer distance, *i.e.*, 0.34 nm. (*72*, *73*) In this regard, the thickness of ~ 100 flakes is measured to build up the statistics. Statistical analyses are fitted with log-normal distributions, following the behaviour of a fragmented system. (*321*)

The images are acquired with Bruker Innova AFM in tapping mode using silicon probes (f = 300 kHz, k = 40 Nm^{-1}). Images of 5×5 μm^2 are collected with 512 data points per line and measurements are taken using a scan rate of 0.7 Hz. The sample preparation is done by drop casting the exfoliated graphite dispersion onto a Si/SiO_2 wafer (Si-Mat Silicon Materials) substrate and dried under vacuum overnight.

The FLG-$PMMA_{US}$ dispersions are filtered by vacuum filtration, followed by the washing with acetone. In order to re-disperse the flakes in acetone, the filters are sonicated for 30 minutes. The as-produced dispersions are diluted 1:30 in acetone and 10 µL of the diluted dispersions are drop-cast onto Si/SiO_2 wafers and dried at 60 °C for 24 hours in a vacuum oven. The samples of the FLG_{US}

dispersions are diluted 1:30 before the drop-casting onto the Si/SiO_2 wafers, with the same drying process of the FLG-$PMMA_{US}$ dispersions. The FLG_{WJM} dispersion is diluted 1:50 and NMP is eliminated by drying the sample at 50 °C overnight under vacuum.

2.3.2.1 Analysis of PMMA traces on the atomic force microscopy (AFM) samples by thermogravimetric analysis (TGA)

The presence of PMMA residues on the AFM samples of the FLG-$PMMA_{US}$ dispersion centrifuged at 200 g is evaluated using TGA. The dispersion rinsed from PMMA is deposited on the pan for analysis in nitrogen atmosphere at a flow rate of 50 mL min^{-1} and a heating ramp from 30 °C to 800 °C at 10 °C min^{-1}.

2.3.3. Transmission electron microscopy (TEM)

Transmission electron microscopy is used to measure the lateral size of the exfoliated graphite flakes. In order to obtain a measurement as accurate as possible, the lateral size of ~100 flakes is analysed and a log-normal distribution is applied to the statistics achieved from the measurements. (*174*) It was found that the values of the lateral size of the flakes produced by sonication follow a log-normal distribution. (*174*) The samples for TEM are prepared by diluting (1:30) the exfoliated graphite dispersions and then drop-casting the diluted dispersion onto holey carbon 400 mesh Cu grids, from Ted Pella Inc. A JEOL JEM-1011 transmission electron microscope is used to collect the TEM images.

2.3.4 Viscosity measurement by rheology

The viscosity measurements of acetone and the mixture acetone-PMMA are performed with a Discovery HR-2 Hybrid Rheometer (TA instruments), using a double-wall concentric cylinders geometry (inner diameter of 32 mm and an outer diameter of 35 mm), designed for low-viscosity fluids. The tests are carried out setting a constant shear rate at 50 s^{-1} at a temperature of 25 °C, and

taking three measurements per sample. The stress, σ_S, at a constant shear rate, $\dot{\gamma}$, at a constant temperature is collected to calculate the viscosity through the equation 7: (*322*)

$$\eta = \frac{\sigma_S}{\dot{\gamma}} \quad \textit{Equation 7}$$

The stress σ_S is obtained by measuring the torque, *M*, during the test, as the stress is expressed by the equation 8. (*322*)

$$\sigma = M \times K_\sigma \quad \textit{Equation 8}$$

in which, K_σ is the stress constant and it is a geometry dependent factor. (*322*)

2.3.5 Contact angle

The surface tension measurements of acetone and the mixture acetone-PMMA are carried out with a Dataphysics OCAH200 contact angle goniometer equipped with a 2/300 CCD Chip camera at laboratory conditions (temperature 22-25 °C and relative humidity 50-60 %). The surface tension is evaluated through the pendant drop method dispensing 12 µL of the different solutions at ambient temperature. (71) Moreover, the Young-Laplace equation is used for the calculations of the surface tension. (72)

The surface tension γ is calculated through the equation 9: (*323*, *324*)

$$\gamma = \frac{\Delta\rho \; G_c \; R_0^2}{\beta} \quad \textit{Equation 9}$$

in which $\Delta\rho$ is the density difference between the medium in the drop and the surrounding atmosphere, G_c is the gravitational constant, R_0 is the radius of curvature at the drop apex and β is a shape factor. (*323*, *324*)

2.3.6 Techniques to evaluate the graphene concentration

The concentration of the graphene dispersions is measured using different techniques, *i.e.*, as vacuum filtration, TGA and OAS.

2.3.6.1 Vacuum filtration

The evaluation of the concentration of the FLG_{US} and FLG-$PMMA_{US}$ dispersions is carried out through vacuum filtration, using polytetrafluoroethylene (PTFE) filters with a pore size of 0.2 µm (Merck Millipore). A volume of FLG_{US} or FLG-$PMMA_{US}$ dispersions is vacuum filtrated and the mass of the filter is measured before ($M_{initial}$) and after (M_{final}) the vacuum filtration. The concentration is calculated using equation 10.

$$C = \frac{M_{initial} - M_{final}}{V_{FLG}} \quad \textit{Equation 10}$$

In order to remove the moisture and the residual acetone in M_{final}, the filters are dried before and after the filtration in a vacuum oven (Binder VLD 115) for 24 hours at 40 °C. Moreover, the filters used for the filtration of the dispersions FLG-$PMMA_{US}$ centrifuged at 200 *g*, 4300 *g* and 17000 *g*, are washed with 50, 100 and 150 mL of acetone, respectively, to eliminate the excess of PMMA. Thermogravimetric analysis and optical extinction spectroscopy are used to validate the concentration data obtained by the vacuum filtration method.

2.3.6.2. Thermogravimetric analysis (TGA)

The thermogravimetric analysis is used to have an indication of the mass of graphene present in the FLG-$PMMA_{US}$ dispersion. The TGA analysis is performed on the FLG-$PMMA_{US}$ dispersion, centrifuged at 200 g, to confirm that PMMA is not affecting the values of concentration obtained in vacuum filtration. In fact, graphene is stable up to 800 °C in a nitrogen atmosphere (*325*, *326*), so that the residue of the sample can be exploited to have an indication of the quantity of graphene in a sample. The TGA analysis is carried out using a TGA Q500-TA Instrument at a flow rate of 50 mL min^{-1} under a nitrogen atmosphere. The TGA is performed on five samples, which are prepared by casting 1 mL of FLG-$PMMA_{US}$ dispersion in the TGA pans. The analysis begins with an isothermal at 60 °C for 15

minutes to remove the solvent and then, once the temperature reaches 30 °C, it is raised up to 800 °C using a heating rate of 10 °C min^{-1}.

2.3.6.3 Optical absorption spectroscopy (OAS)

Optical absorption spectroscopy is used to calculate the concentration of the graphene dispersions by using a Cary Varian 5000UV-Vis spectrophotometer.

The concentrations are calculated through the Lambert-Beer law, expressed in equation 11.

$$Ab = \alpha l C \quad \textit{Equation 11}$$

The absorbance value (*Ab*) is chosen in a point of the spectrum where there are no features, *e.g.,* 660 nm. Moreover, α is the extinction coefficient and *l* is the light path length.

In the case of the graphene dispersions produced through ultrasonication, the OAS is used to confirm the concentration obtained in the vacuum filtration, in order to assure that the PMMA is not affecting the measured value.

The extinction coefficient of the FLG-$PMMA_{US}$ dispersion, centrifuged at 200 g, is calculated through the following steps:

1) Prepare six different FLG-$PMMA_{US}$ diluted dispersions with dilutions 1:100, 1:80, 1:60, 1:50, 1:30 and 1:20, taking as “known” concentration the one obtained from the TGA (section 2.3.6.2.).
2) Measure the absorbance value for all the diluted FLG-$PMMA_{US}$ dispersion, performing the analysis on five samples for each different dilution
3) Express the measured absorbance in function of the “known” concentration of the diluted FLG-$PMMA_{US}$ dispersions, obtaining a curve.
4) Calculate the extinction coefficient as the slope of the obtained curve

For what concern the FLG_{WJM} dispersions, the samples for the OAS are prepared by diluting the dispersion graphene-NMP in NMP with ratio 1:100, measuring the optical absorption coefficient at 660 nm and considering 2460 L g^{-1} m^{-1} as extinction coefficient. (*118*)

2.3 Graphene-polymer composites

The following paragraphs describe the processes used to produce and manufacture the graphene-polymer composites, followed by the description of the experimental details regarding the characterization. **Fig. 30** describes the production and manufacturing processes used to prepare the samples of the graphene-polymer composites and the characterization techniques exploited for their characterization.

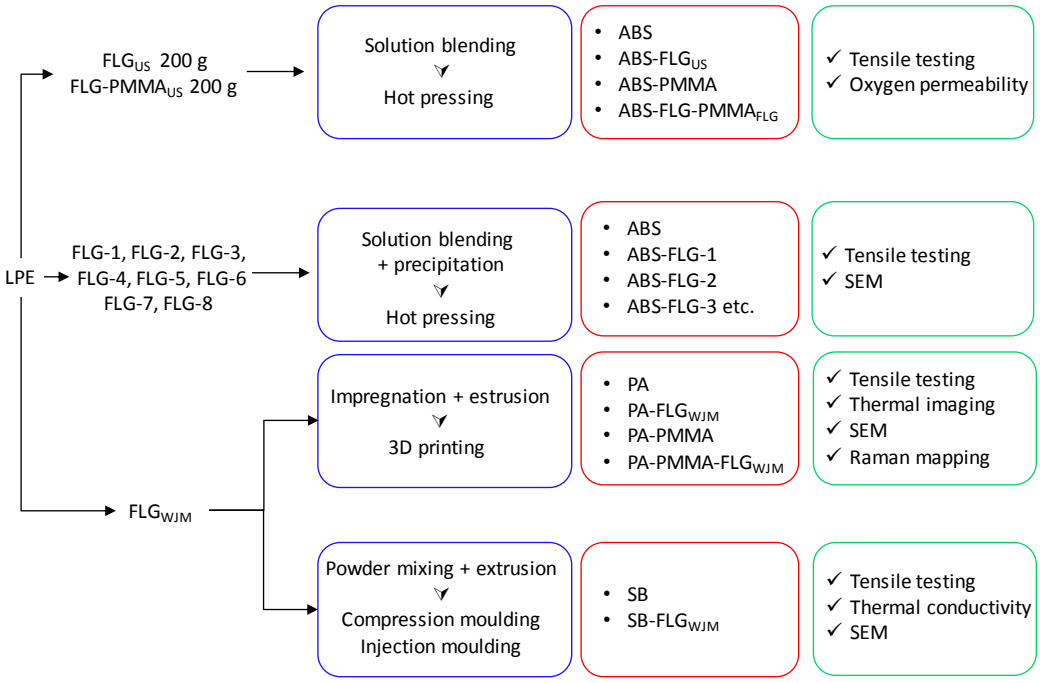

Figure 30 *– Scheme of the production, the manufacturing of the graphene-ABS composites prepared with the dispersions FLG_{US} and FLG-$PMMA_{US}$ and the dispersions FLG-1, FLG-2, etc.; the graphene-PA composites and graphene-SB composites produced with the graphene powder obtained by the dispersion FLG_{WJM}.*

2.3.1 Production of graphene-polymer composites

The following paragraphs present the different techniques used to produce the graphene-polymer composites. In detail, solution blending is performed to produce graphene-ABS composites using

the FLG_{US} and FLG-$PMMA_{US}$ dispersions and the FLG dispersions in NMP. While, graphene-PA composites and graphene-SB composites are prepared by means of melt blending, using the graphene-based powder obtained from the FLG_{WJM} dispersions.

2.3.1.1 Graphene-acrylonitrile butadiene styrene (ABS) composites

2.3.1.1.1 Use of the exfoliated graphite dispersions in acetone and acetone-poly methyl methacrylate (PMMA) mixture

The ABS composites are prepared using both FLG_{US} and FLG-$PMMA_{US}$ dispersions centrifuged at 200 g. The solution blending method is used to prepare six different composites with a loading ranging from 0.005 to 0.1 wt %, compared to the ABS matrix. The ABS dispersion in acetone (30 wt % of ABS) is mixed with both the FLG_{US} and FLG-$PMMA_{US}$ dispersions and cast into glass Petri dishes (diameter = 7.5 cm). Firstly, the drying of the films is done in air for 16 hours and then in a vacuum oven (Binder VLD 115) at 30 °C for other 16 hours. The same procedure is used to prepare control samples ABS-PMMA, containing the same amount of PMMA present in the ABS-FLG-$PMMA_{US}$ and ABS composites, *i.e.,* 0.34 wt %, 0.68 wt %, 3.4 wt % and 6.8 wt %.

2.3.1.1.2 Use of the exfoliated graphite dispersions in N-methyl pyrrolidone (NMP)

Acrylonitrile butadiene styrene (ABS) pellets are dissolved in acetone with a concentration of 240 mg mL^{-1}. The exfoliated graphite flakes dispersed in NMP are exchanged in acetone at a concentration of 10 mg mL^{-1}. The as-obtained dispersion in acetone and the ABS dispersion are mixed and sonicated for 1 h, obtaining composites with loadings ranging from 0.01 to 1 wt %. Pellets are formed by coagulating/precipitating the previously prepared dispersion of ABS and exfoliated graphite flakes in acetone. Finally, composite pellets are dried in a vacuum oven at 80 °C for 12 hours (Binder VLD 115).

2.3.1.2 Graphene-polyamide 6 (PA) composites

The graphene-PA composites are prepared using the lyophilized powder obtained from the FLG_{WJM} dispersion, described in section 2.2.2.

Three composites are produced:

1) PA-FLG_{WJM}, containing FLG_{WJM}
2) PA-PMMA-FLG_{WJM} containing both PMMA and FLG_{WJM}
3) Control samples without graphene "PA-PMMA"

In order to prepare the composites, the pristine PA pellets are impregnated with dispersions of FLG_{WJM} re-dispersed in bare acetone or acetone-PMMA mixture, at a concentration of 10 g L^{-1}, to produce the composites PA-FLG_{WJM} and PA-PMMA-FLG_{WJM}, respectively (**Table 2**). The obtained dispersions are then ultrasonicated for 1 hour at a temperature ranging from 25 °C to 35 °C (VWR-Ultrasonic cleaner USC-THD). Bare acetone and acetone-1 wt %PMMA mixture without WG are subjected to the same treatment, in order to be used to impregnate the pristine PA pellets and produce the pristine PA and "PA-PMMA" samples, accordingly (**Table 2**). The impregnation process is performed by stirring mechanically (Heidolph MR Hei-Standard) the as-prepared dispersions with pristine PA pellets at 60 °C, until the complete evaporation of the solvent.

***Table 3**- Compositions of the prepared samples*

Sample	Dispersion for impregnation	FLG_{WJM} (wt%)	PMMA (wt%)
PA	Bare acetone	-	-
PA-1FLG_{WJM}	Acetone + FLG_{WJM}	1	-
PA-3FLG_{WJM}	Acetone + FLG_{WJM}	3	-
PA-PMMA-1FLG_{WJM}	Acetone-PMMA + FLG_{WJM}	1	1
PA-PMMA-3FLG_{WJM}	Acetone-PMMA + FLG_{WJM}	3	3
PA-1PMMA	Acetone-PMMA	-	1
PA-3PMMA	Acetone-PMMA	-	3

The impregnated pellets are then dried overnight under vacuum at 80 °C (Binder VLD 115). Subsequently, extrusion by means of a single-screw extruder is performed using the dried pellets

(Single screw module diameter 12 11 L/D, Scamex) using a temperature range between 235 °C and 245 °C, to obtain a filament. The compositions and the dispersions used for the impregnation of the prepared samples are shown in **Table 3**.

2.3.1.3 Graphene- styrene butadiene copolymer (SB) composites

The graphene-SB composites are produced using the lyophilized powder from the FLG_{WJM} dispersion. The SB powder is mixed with the FLG_{WJM} powder using a planetary mixer (Thinky ARE-250) for 2 minutes at 1000 rpm for two times. Then, the mixed powders are extruded using a twin-screw extruder (2C15-45 L/D laboratory, Bandera extrusion academy) in the 140 °C - 160 °C temperature range. The as-prepared samples are the pristine SB and the composites containing 1, 2, 4, 6, 8, 10 and 15 wt% of FLG_{WJM}.

2.3.2 Manufacturing of graphene-polymer composites

Various manufacturing techniques are exploited in the following paragraphs, in order to prepare the samples for the characterization of the graphene-polymer composites. The graphene-ABS composites are manufactured by hot-pressing the films obtained from the aforementioned solution blending procedure. Instead, 3D printing is exploited to prepare the samples of the graphene-PA composites. About the graphene-SB composites, two different manufacturing techniques are utilized, compression moulding and injection moulding.

2.3.2.1 Graphene-acrylonitrile butadiene styrene (ABS) composites

The films obtained by solution blending using FLG_{US} and FLG-$PMMA_{US}$ are hot-pressed (Specac – Atlas Auto T8), applying 1 metric ton at 180 °C, to obtain 200 µm in thickness. The thickness of the films is measured with a calibre (Mahr 16EX).

Hot pressing (Specac – Atlas Auto T8) is used to manufacture composite films by using the pellets obtained from the solution blending with FLG dispersions in NMP exchanged in acetone. The manufacturing process is performed at 215°C using 1 metric ton for 5 minutes.

2.3.2.2 Graphene-polyamide 6 (PA) composites

The filaments obtained from the extrusion of the impregnated pellets of the samples "PA-FLG_{WJM}", "PA-PMMA-FLG_{WJM}" and "PA-PMMA" are used to 3D print the samples for the characterization through the fused deposition modelling technique (FDM) (Ira3D, Poetry Infinity). The code files used in FDM are obtained from a design software (AutoCAD) and the slicing program "Ira3D 6.3.3". The samples are printed using the following parameters: nozzle diameter 0.45 mm; raster of infill ± 45 °; infill percentage 75 %; layer height 0.1 mm; printing speed 40 mm s^{-1}; nozzle temperature 245 °C; bed temperature 90 °C.

2.3.2.3 Graphene-styrene butadiene copolymer (SB) composites

The extruded filaments are pelletized and the pellets are manufactured through compression moulding and injection moulding. The compression moulding is carried out by using a hot pressing machine applying a load of 10 bar for 5 minutes at 100 °C. The injection moulding is performed using a Babyplast 6/10P (Cronoplast S.L.) in the 245 °C - 255 °C temperature range and injecting the melted material in a mould at room temperature. The samples used for thermal imaging are obtained from the compression moulded samples containing 15 % of loading. These samples are hot-pressed (Specac – Atlas Auto T8), applying 4 metric ton at 100 °C, to obtain 100 µm in thickness. The thickness of the films is measured with a calibre (Mahr 16EX).

2.3.3 Characterization of the graphene-polymer composites

The following paragraphs describe the experimental details of the techniques used to characterize the graphene-polymer composites. Tensile testing is performed in order to measure the mechanical properties. While, the thermal conductivity and the heat transfer are evaluated through transient plane source and thermal imaging, respectively. An optical oxygen analyser is exploited to obtain the values of the oxygen permeability. About the tribological properties, the coefficient of friction and the wear rate are measured by using a scratch test, static and cyclic, accordingly. Moreover, scanning electron microscopy and Raman mapping are used to study the morphology of the graphene-polymer composites.

2.3.3.1 Tensile testing

The tensile tests are performed using an Instron dual column tabletop universal testing System 3365. The cross-head speed is 5 mm min^{-1} for the graphene-ABS composites and the graphene-PA6 composites, while it is 50 mm min^{-1} for the graphene-SB composites. The samples are dog-bone-shaped with the dimensions chosen according to ASTM D638 standard. Fifteen samples are tested for each composite. The parameters evaluated through tensile testing are the Young's modulus and the tensile strength. The Young's modulus is defined as the slope of the stress versus the strain curve in the elastic region. (*327*) It describes the stiffness of the material, the higher is the Young's modulus value, and the stiffer is the material. (*327*) The tensile strength is the highest value of stress reached during the testing and it corresponds to the maximum load the material can handle. (*327*)

2.3.3.2 Gas barrier measurements

The oxygen permeation of the graphene-ABS composites is measured by using the Oxysense 5250i device (Oxysense, USA) equipped with a film permeation chamber. This instrument is operated according to ASTM Method F3136-15 (ASTM 1989). The test is performed under the standard

laboratory conditions*, i.e.,* 23 °C and 50 % relative humidity. The hot-pressed films are cut into a square piece (6 × 6 cm^2) and then placed inside the chamber. The OxySense fibre optic pen measures the oxygen reading from the oxydot, at specific time intervals. The oxygen transmission rate (OTR) of each film is measured by monitoring the oxygen uptake with time. Oxysense OTR software used this oxygen evolution to determine the OTR of films. Ten readings are taken for each sample with a minimum coefficient of determination (R^2) value of 0.995. The oxygen permeability, *i.e.,* OP, is defined through the equation 12. (*328*)

$$OP = \frac{OTR * t_f}{P_e - P_i} \quad \textit{Equation 12}$$

In which, OTR is the oxygen transmission rate, indicating the amount of oxygen passing through the sample per day, t_f is the thickness of the sample, while P_e and P_i are the partial oxygen pressure of the external environment and of the oxygen-free room, respectively. (*328*)

2.3.3.3 Tribological testing

The friction and wear resistance of the composites PA-1FLG$_{WJM}$, PA-3FLG$_{WJM}$, PA-PMMA-1FLG$_{WJM}$, PA-PMMA-3FLG$_{WJM}$ and of the pristine PA are tested through multi-pass scratch tests on a Micro-combi tester (Anton Paar Gmbh, Germany). All the samples are 3D printed and have a rectangular shape with arbitrary dimensions (length × width × height = 50×20×0.5 mm^3).

A bearing steel ball of 500 mm radius is used as the counterpart for rubbing, moving with a displacement rate of 10 mm min^{-1} for a reciprocating distance of 4 mm (frequency = 0.042 Hz). A constant load of 10 N is used for 10000 cycles for a total time of 11 hours and 30 minutes. All the tests are carried out under controlled laboratory conditions of a temperature of 21 ± 1 °C and relative humidity of 50 ± 5 %.

The scratch depth, *d,* is measured by using a profilometer (Ambios Technology XP-2). To calculate the wear volume through the equation 13: (*298*)

$$\Delta V = \frac{L_m}{2} {r_{ball}}^2 \left[cos^{-1}\left(\frac{r_{ball}-d}{r_{ball}}\right) - \frac{\sqrt{r_{ball}^2-d^2}}{r_{ball}} \right] \quad \textit{Equation 13}$$

in which, r_{ball} is the radius of the rubbing ball and L_m is the total scanned length.

The wear rate *K* is defined by the equation 14 (ASTM G-99):

$$K = \frac{\Delta V}{F \times N \times L_m} \quad \textit{Equation 14}$$

in which, *F* is the applied load, *N* is the number of cycles and L_m is the total length of the scratch. The values of the steady coefficient of friction (μ) are extracted from the experimental data plots, collected during the running-in phase

2.3.3.4 Thermal imaging

The thermal imaging analysis is performed on both the graphene-PA composites and on the graphene-SB composites. A thermal camera, FLIR A655sc series ResearchIR Max 4, is used for all the measurements.

About the graphene-PA composites, the samples have a rectangular shape and arbitrary dimensions (length × width × height = 50×20×0.5 mm^3). The samples are tested using a halogen lamp (Westelettric SL40, power 50 W) as a source of heat. The samples are exposed to the heat source at a distance of 15 cm for 20 s to test the thermal transfer.

About the thermal imaging analysis carried out on the graphene-SB composites, the samples are round-shaped films with a thickness of 100 µm (see section 2.3.2.3). The used source of heat is a heating gun (Bosch, GHG 660 LCD) set at a temperature of 50 °C, heating the sample from below. The samples are heated for two minutes and the test is repeated three times.

2.3.3.5 Thermal conductivity measurement

The thermal conductivity of the graphene-based composites is measured by the Hot Disk TPS-3500 thermal constants analyser at room temperature. The samples are circular disks with a diameter of 2 cm and a thickness of 3 mm produced by both compression and injection moulding, six samples for each composition are analysed.

2.3.3.6 Morphological analysis

The morphology of the graphene-SB composites and graphene-PA composites is investigated by using SEM with an FE-SEM Jeol GSM-7500FA. A gold film with a thickness of 10 nm is deposited by sputtering (Cressington sputter coater 208HR) on the cross-section of the samples. The SEM images are used to measure the orientation of the flakes protruding from the cross-section of the graphene-SB composites by a human operator. A number of 100 measurements are taken per sample by using the program ImageJ.

Raman mappings are carried out on the graphene-PA composites through a Renishaw inVia confocal Raman microscope using an excitation line of 514.5 nm (2.41 eV) in streamline HR mode with a 100× objective lens, and an incident power of 1 mW on the samples. During the Raman mapping, 784 spectra are collected over a 26 × 27.5 μm^2 area of the cross-section of the composites without any previous treatment.

Chapter 3: Poly methyl methacrylate assisted exfoliation of graphite and its use in acrylonitrile butadiene styrene composites

3.1 Motivation and rationale

In this study, the goal is to address the issues related to the use of toxic and high boiling point solvents in LPE for the production of graphene (see section 1.3.1.3). Low boiling point solvents, *i.e.*, <90 °C, are preferred in order to avoid damaging effects in the development of graphene-based polymer composites, *e.g.*, incipient degradation and shrinkage of the polymer matrix. (*329*, *330*) Moreover, the solvent has to be easy to remove, because the solvent residues influence the physical and chemical properties of the composite material. (*148*, *149*) Among the low boiling point solvents, acetone stands out as it is harmless (*331*) and it dissolves many polymers, *e.g.,* cellulose acetate (CA) (*332*), acrylonitrile butadiene styrene (ABS) (*333*), poly (methyl methacrylate) (PMMA) (*334*, *335*), styrene-acrylonitrile (*336*), poly (ethylene oxide) (*337*) and poly (vinyl acetate) (*338*, *339*), just to cite a few. However, the surface tension of acetone does not match the required value for the exfoliation of graphite, (*142*), *e.g.,* $\gamma_{acetone}$ = 26.67 mN m^{-1} (*144*). In general, polymers assist the stabilization of exfoliated graphene flakes in low boiling point solvents via steric stabilization.(*127*, *340*–*342*) For example, PMMA is an inexpensive (~ € 150 per ton(*343*)) and non-toxic polymer (*344*), which forms π-π bonds between the carbonyl groups and the graphene, promoting the attachment of the polymer chains onto the graphene flakes. (*345*–*347*) Moreover, PMMA can form homogeneous blends with other polymers, *e.g.,* PVC (*348*), polyaniline (PANI) (*349*), poly ethylen glycol (PEG) (*350*), ABS (*351*) among others. The miscibility of PMMA with other polymers can be exploited to obtain a homogenous distribution of the graphene flakes into different polymeric matrices.

In order to study the effect of PMMA on the LPE, dispersions of exfoliated graphite with three different centrifugal accelerations, *i.e.,* 200 *g*, 4300 *g* and 17000 *g*, are produced. The main features of the dispersions, as the concentration of the exfoliated graphite flakes, as well as their characteristics as the thickness, the number of layers and the lateral size, are analysed. Moreover, the obtained dispersions with and without PMMA are used to prepare ABS composites. In detail, the effect of the exfoliated graphite flakes produced in acetone and PMMA on the mechanical and gas barrier properties of the composites is analysed. In the composites containing both graphene and PMMA, the mechanical and gas barrier properties are improved with respect to the composites containing graphene only, as the presence of PMMA promotes the distribution of the flakes, due to its miscibility with ABS. (*351–356*)

3.2 Characterization of the exfoliated graphite dispersions

The FLG_{US} and FLG-$PMMA_{US}$ dispersions are analysed by Raman spectroscopy, in order to obtain an indication about the thickness of the flakes, identify the kind of defects and investigate a possible doping effect on the flakes due to PMMA addition (see section 2.3.1). (*304*, *305*)

The **Fig. 31a-c** present the $I(2D_1)/I(G)$ as function of $I(2D_2)/I(G)$ of the dispersions centrifuged at 200 *g* (**Fig. 31a**), 4300 *g* (**Fig. 31b**) and 17000 *g* (**Fig. 31c**), respectively. The percentage of the points above the middle line (few layer condition) over the total number of points are 36 %, 53 % and 93 % for the FLG_{US} dispersions and 58 %, 70 % and 98 % for the FLG-$PMMA_{US}$ dispersions, centrifuged at 200 *g*, 4300 *g* and 17000 *g*, respectively.

The FLG-$PMMA_{US}$ dispersions present a higher percentage of FLG flakes compared to the FLG_{US} dispersions. For both the dispersions, the percentage of MLG and unexfoliated flakes in the supernatant is decreasing with the centrifugal acceleration (**Fig. 31a-c**). Moreover, there is a decrease of the $I(2D_2)/I(2D_1)$ ratio due to the decrease of graphitic and MLG flakes in the supernatant, as the intensity of the component $2D_1$ increases (**Fig. 31d**).

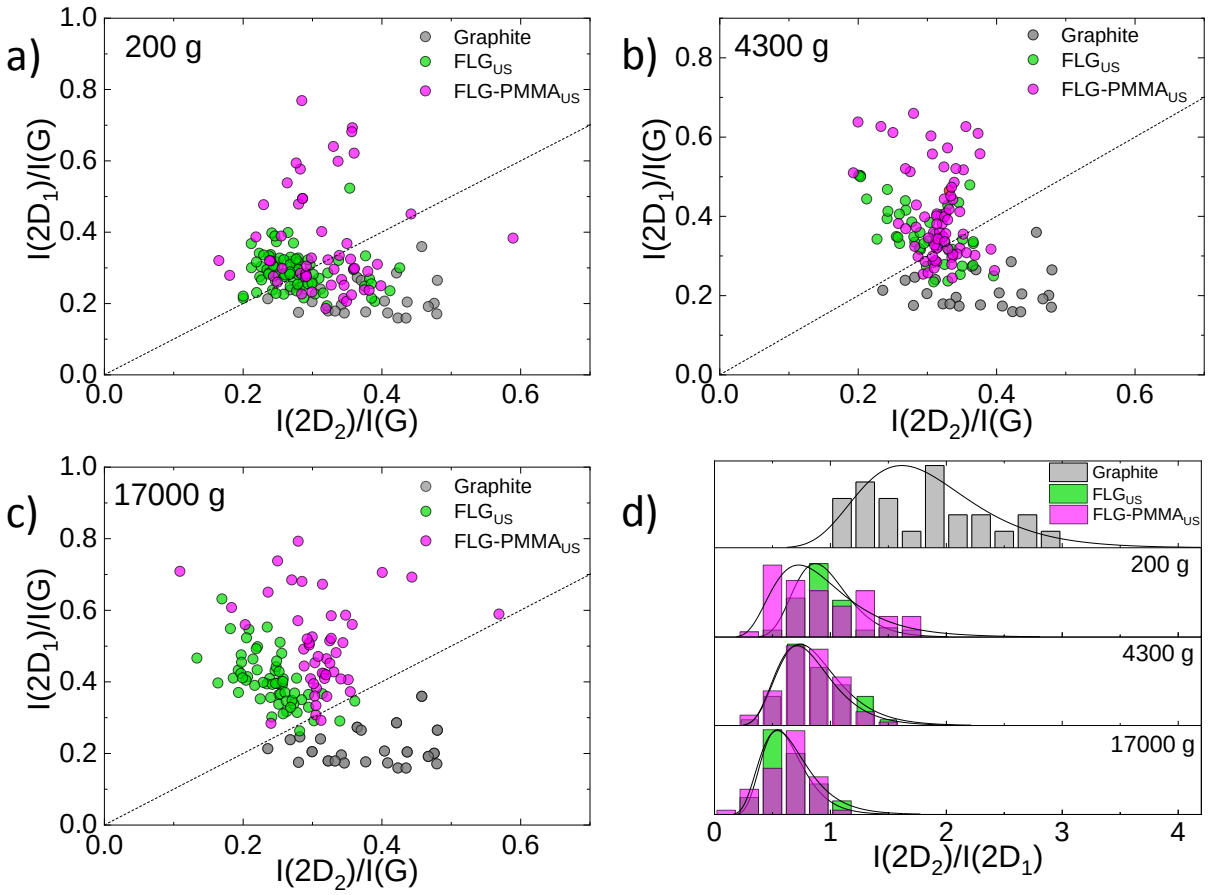

Figure 31 - The normalized intensities $I(2D_2)/I(G)$ vs $I(2D_1)/I(G)$ shows the distribution of FLG and graphitic flakes for the dispersions obtained at a) 200 g, b) 4300 g and c) 17000 g, d) $I(2D_2)/I(2D_1)$.

Fig. 32a-c represents the Raman spectra for the FLG_{US} (green spectrum) and $FLG\text{-}PMMA_{US}$ (magenta spectrum) dispersions produced using a centrifugal acceleration of 200 *g* (**Fig. 32a**), 4300 *g* (**Fig. 32b**) and 17000 *g* (**Fig. 32c**). Graphite (black spectrum) and PMMA (cyan spectrum) are also plotted for comparison. All the spectra, apart from bare PMMA, are normalized to the G peak.

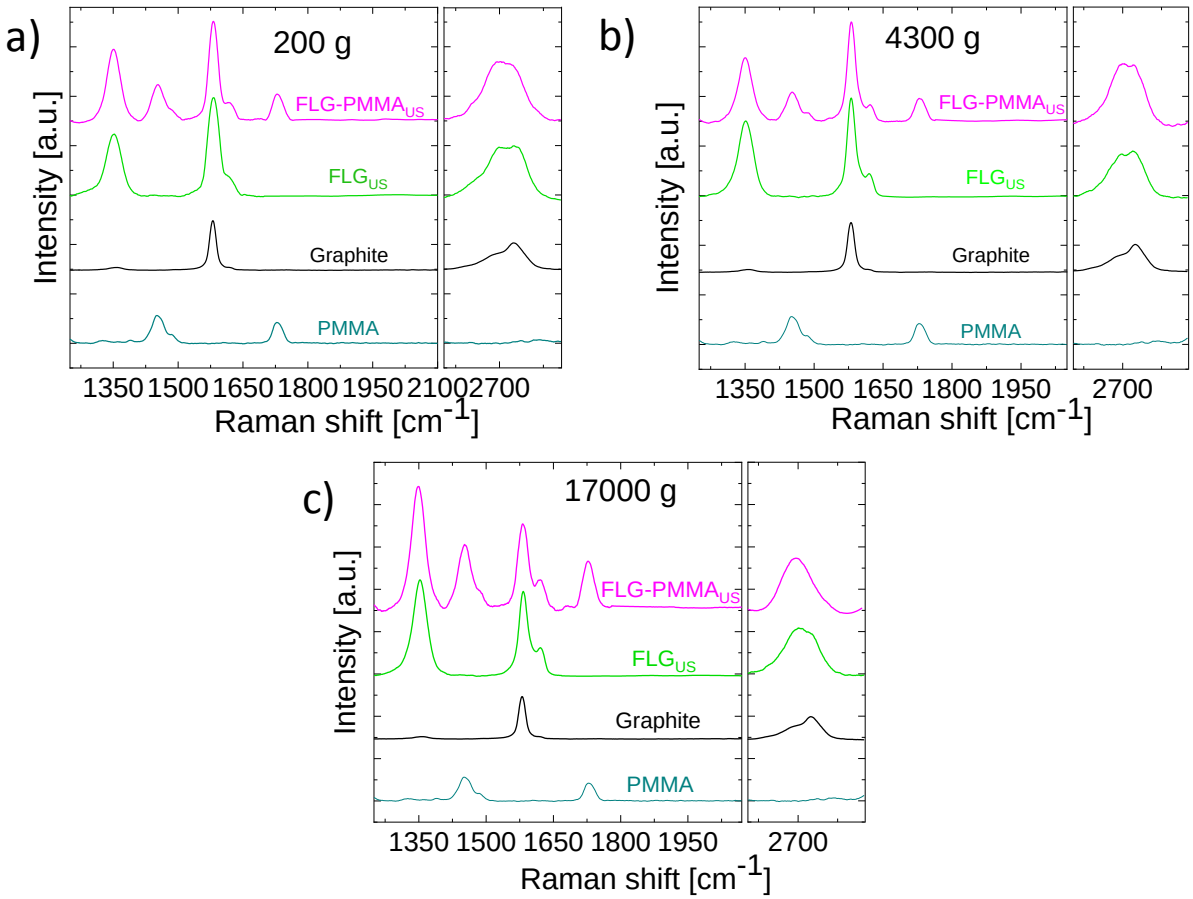

Figure 32 *- Raman spectra of graphite (black), bare PMMA (cyan) and the FLG-PMMA$_{US}$ (magenta) and FLG$_{US}$ (green) dispersions obtained with a centrifugal acceleration of a) 200 g, b) 4300 g and c) 17000 g.*

The analysis of the defects present on the flakes is important to assess the quality of the flakes, as explained in section 2.3.1. The correlation between FWHM(G) and the intensity and area ratios I(D)/I(G) and A(D)/A(G), respectively, is considered to distinguish between edge and basal plane defects. (*313*) In **Fig. 33**, it is shown that none of the dispersions have a correlation between the I(D)/I(G) and A(D)/A(G) versus the FWHM(G). Therefore, the defects are mainly located on the edges of the flakes. (*313*)

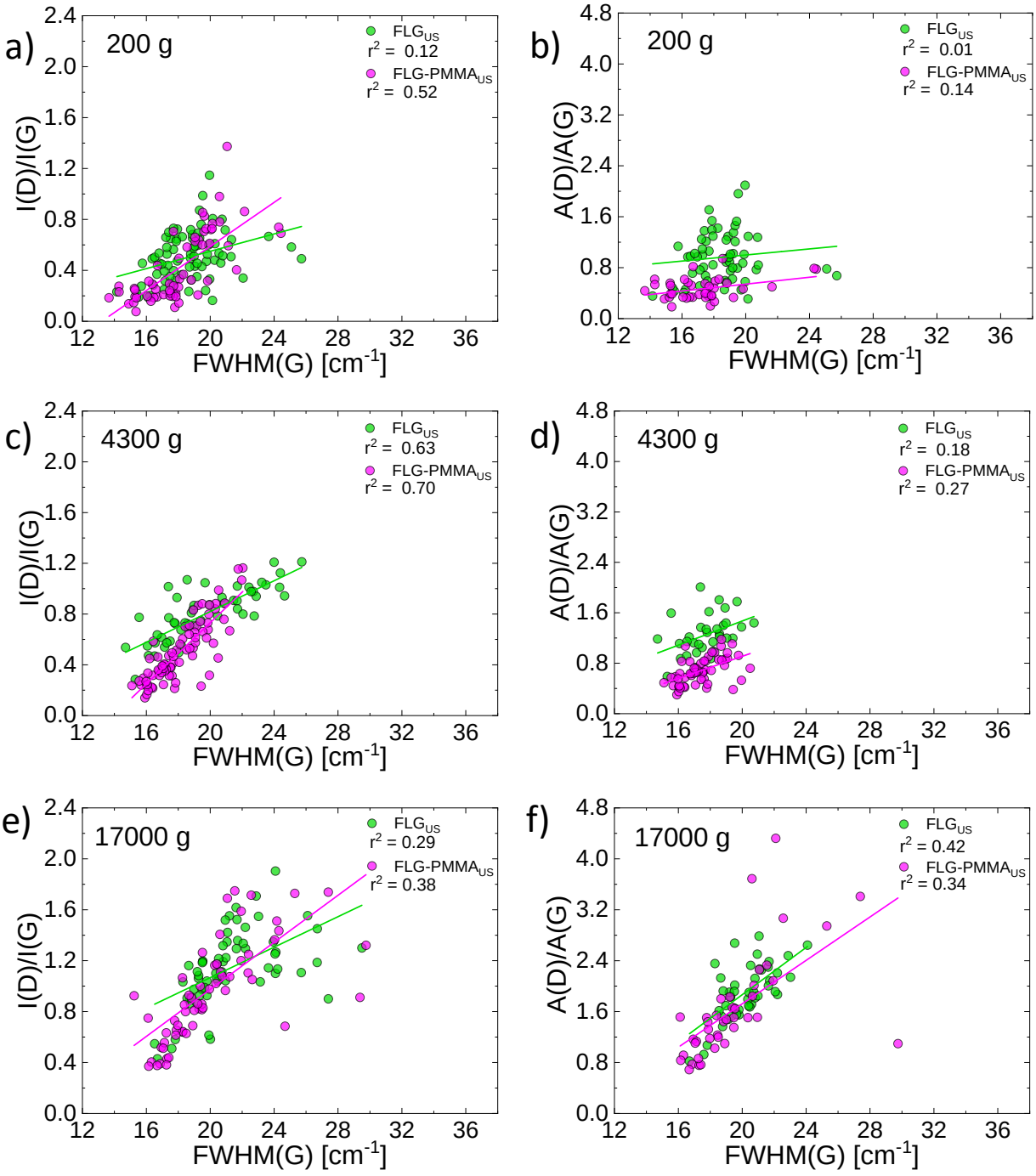

Figure 33 *– I(D)/I(G) and A(D)/A(G) expressed as function of FWHM(G) of the dispersions centrifuged at a-b) 200 g, c-d) 4300 g and e-f) 17000 g, respectively.*

It has been reported that FLG binds through π-π interactions with the carbonyl groups (C=O) of PMMA. (*346*, *347*, *357*) The re-stacking of the exfoliated graphite flakes during and after the exfoliation is hindered due to this interaction. (*340*) The Raman results on the Pos(G) and the FWHM(G) of the FLG-PMMA$_{US}$ dispersion do not change compared to the FLG$_{US}$, (**Fig. 34a-b**). This

indicates that PMMA has no doping effect on the exfoliated graphite flakes, so that the electronic structure of graphene is not affected by the presence of the polymer. (*306*)

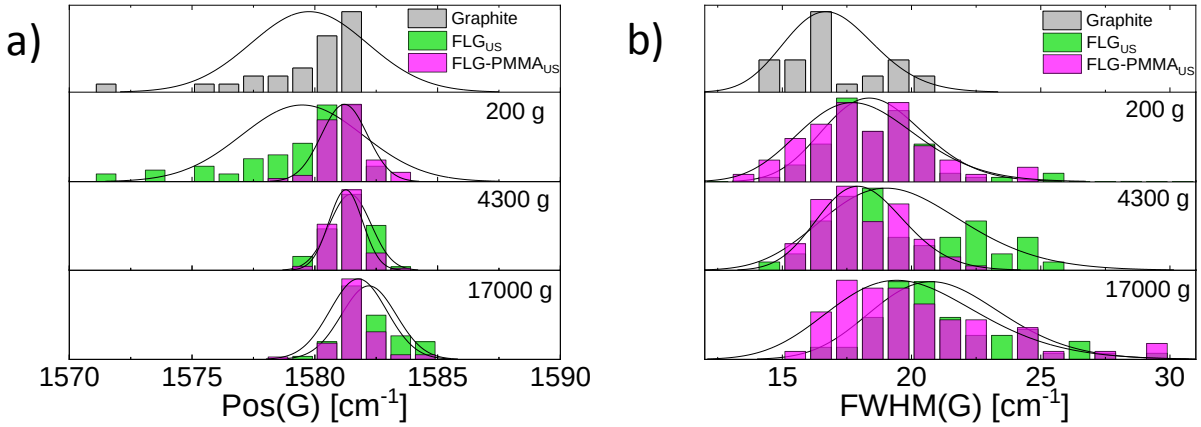

Figure 34 *–Statistical analysis of a) Pos(G) and b) FWHM(G) for the FLG$_{US}$ (green) and FLG-PMMA$_{US}$ (magenta) dispersions centrifuged at 200 g, 4300 g and 17000 g compared with graphite (grey).*

The thickness of the flakes is measured by AFM, considering that, according to literature (*358–361*), the thickness of the FLG flakes measured in tapping mode is lower than 4 nm, *i.e.,* less than 5 layers. The number of FLG flakes present in the FLG$_{US}$ and FLG-PMMA$_{US}$ dispersions is calculated in percentage. The results show that the percentages of exfoliated flakes are 13 %, 35 % and 53 % for the FLG$_{US}$ dispersions, and 30 %, 42 % and 88 % for the FLG-PMMA$_{US}$ dispersions, centrifuged at 200 g, 4300 g and 17000 g, respectively. The FLG-PMMA$_{US}$ dispersions contain a higher percentage of FLG flakes compared to the FLG$_{US}$ dispersions, in agreement with the Raman results.

Representative AFM images of the exfoliated flakes are shown in **Fig. 35a-f**, reporting the thickness statistics in the insets.

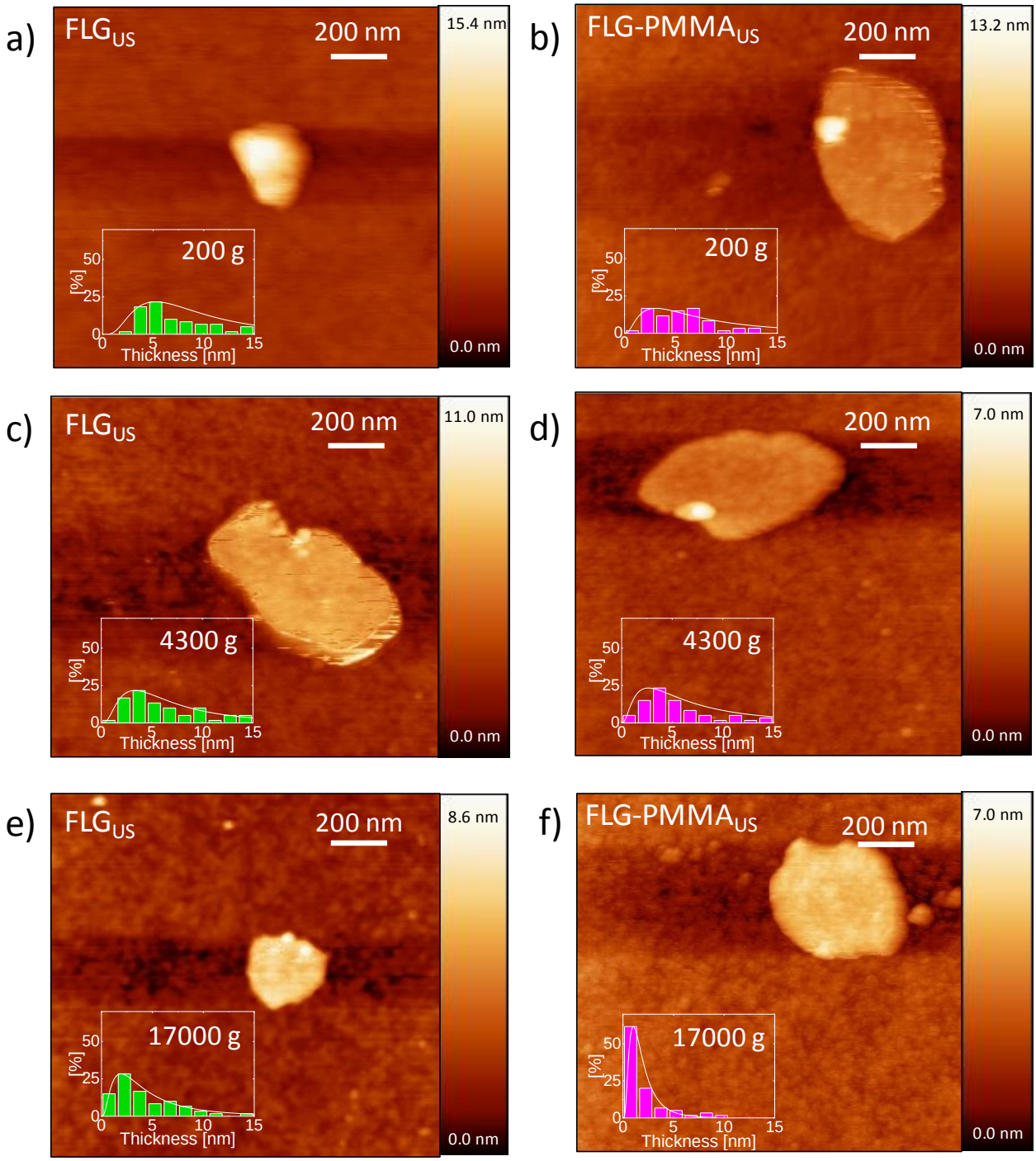

Figure 35 *- AFM images of exfoliated graphite flakes with the thickness distribution given in the inset of the dispersions a) FLG$_{US}$ and b) FLG-PMMA$_{US}$ centrifuged at 200 g, c) FLG$_{US}$ and d) FLG-PMMA$_{US}$ centrifuged at 4300 g and e) FLG$_{US}$ and f) FLG-PMMA$_{US}$ centrifuged at 17000 g.*

The presence of PMMA residue, *i.e.,* 1.5 % of the initial mass, in the AFM samples measured through TGA (**Fig. 36**), over-estimates the thickness measured with the AFM (49).

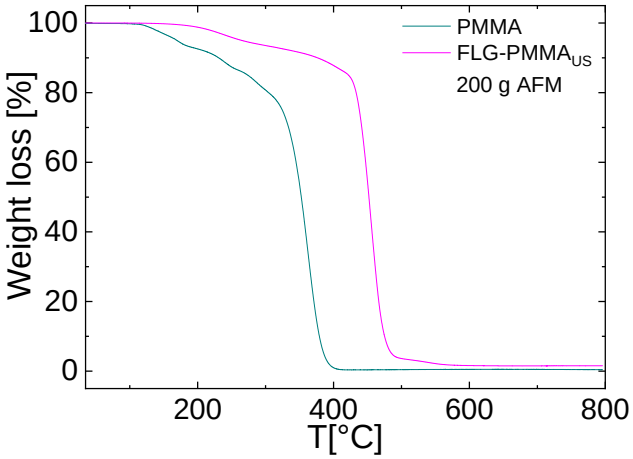

Figure 36 *- Weight loss curve of the concentrated sample obtained from the AFM sample of the FLG-PMMA$_{US}$ dispersion centrifuged at 200 g.*

The TEM indicates the lateral sizes of the flakes of 520 nm (S.D. 0.57), 400 nm (S.D. 0.50), 300 nm (S.D. 0.60) for the FLG$_{US}$ dispersions, and 600 nm (S.D. 0.40), 370 nm (S.D. 0.43), 270 nm (S.D. 0.33) for the FLG-PMMA$_{US}$ dispersions, centrifuged at 200 *g*, 4300 *g* and 17000 *g*, respectively.

The difference in the lateral size of the flakes in the FLG-PMMA$_{US}$ and FLG$_{US}$ dispersions is minimal, but the standard deviation indicates that the distribution of the lateral size of the flakes is more homogeneous than in the flakes of the FLG$_{US}$ dispersion. Representative TEM images of the exfoliated graphite flakes are shown in **Fig. 37a-f** with their corresponding lateral size statistics reported in the insets.

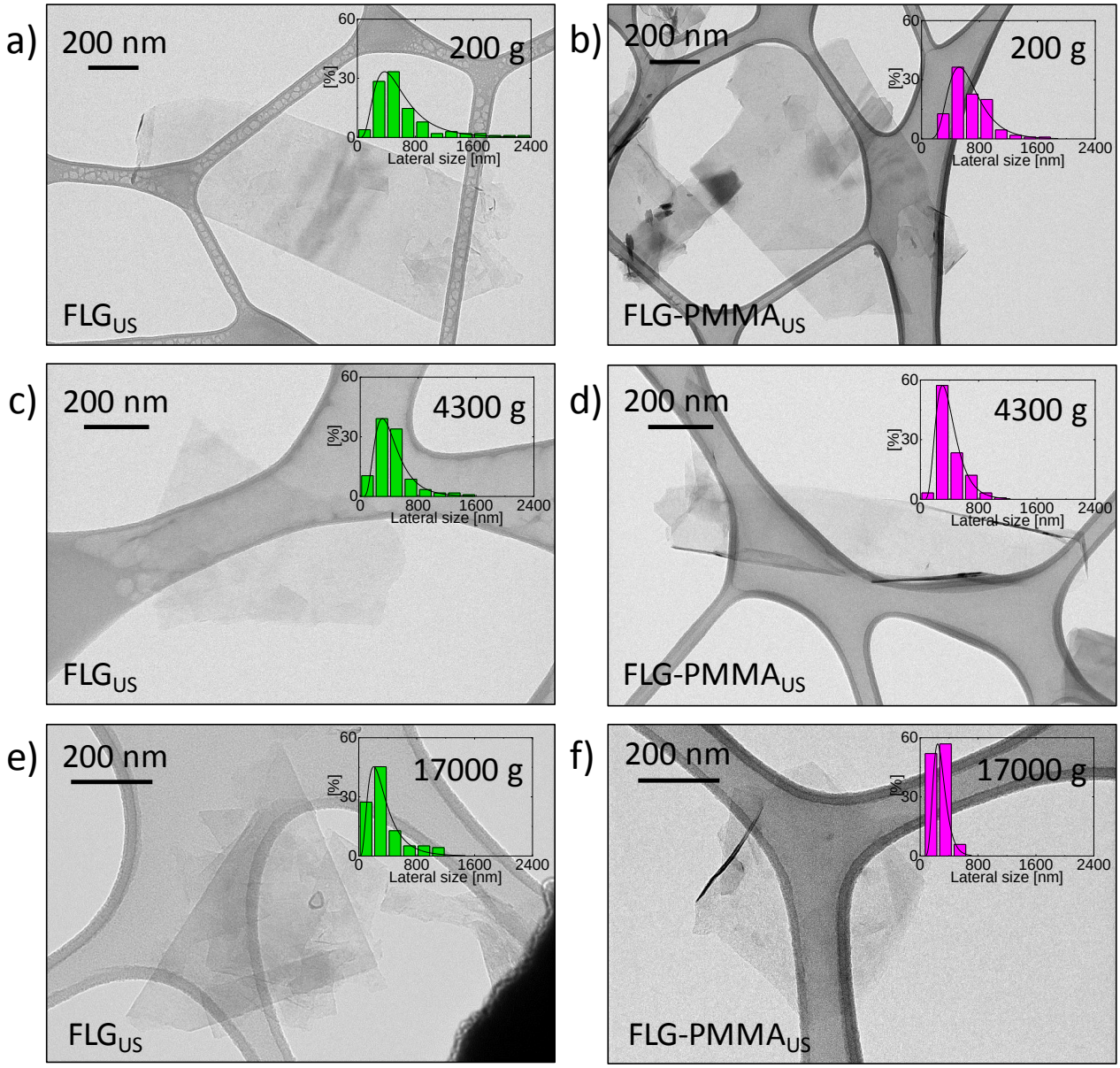

Figure 37 *- TEM images of exfoliated graphite flakes with the lateral size distribution given in the inset of the a) FLG$_{US}$ and b) FLG-PMMA$_{US}$ dispersions centrifuged at 200 g, c) FLG$_{US}$ and d) FLG-PMMA$_{US}$ dispersions centrifuged at 4300 g and e) FLG$_{US}$ and f) FLG-PMMA$_{US}$ dispersions centrifuged at 17000 g.*

The concentration achieved in the exfoliated graphite dispersions is 80 ± 20 mg L^{-1}, 30 ± 10 mg L^{-1} and 1 ± 0.2 mg L^{-1} for the FLG$_{US}$ dispersions, and 220 ± 40 mg L^{-1}, 90 ± 20 mg L^{-1} and 30 ± 6 mg L^{-1} for the FLG-PMMA$_{US}$ dispersions, centrifuged at 200 *g*, 4300 *g* and 17000 *g*, respectively. The concentration of the FLG-PMMA$_{US}$ dispersions is higher compared to the FLG$_{US}$ dispersion, *i.e.,* there is an improvement of + 175 %, + 200 % and + 2900 %.

The concentration of the exfoliated graphite dispersions obtained at 200 g is evaluated also using the TGA, by collecting the residue of both PMMA and of the FLG-PMMA$_{US}$ dispersion (**Fig. 38**). The equation 15 shows the calculation used to achieve the exfoliated graphite mass.

$$m_{FLG} = \frac{m_{tot(FLG-PMMA_{US})} * \left(r_{FLG\text{-}PMMA_{US}} - r_{PMMA}\right)}{100} \quad \textit{Equation 15}$$

in which, $m_{tot(FLG\text{-}PMMAus)}$ is the mass of the FLG-PMMA$_{US}$ sample after the isothermal ramp (see section 2.3.2.1), $r_{FLG\text{-}PMMAus}$ and r_{PMMA} are the residues at 800 °C expressed in percentage of the FLG-PMMA$_{US}$ dispersion and of the bare PMMA, respectively. The measured mass of exfoliated graphite is in agreement with the previous results, *e.g.,* the mass of the exfoliated graphite is 227 ± 8 mg L^{-1} for the sample FLG-PMMA$_{US}$ centrifuged at 200 *g*.

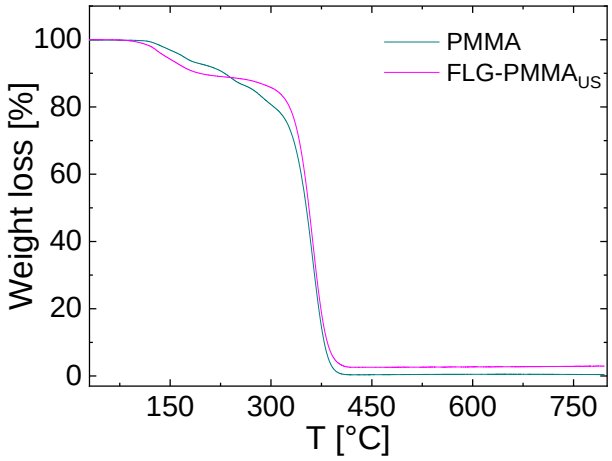

Figure 38 *- Weight loss curves comparison of the bare PMMA and the FLG-PMMA$_{US}$ dispersion centrifuged at 200 g.*

In order to calculate also the effective concentration of the FLG-PMMA$_{US}$ dispersions achieved at 4300 *g* and 17000 *g*, the extinction coefficient of the FLG-PMMA$_{US}$ dispersion is evaluated using OAS, considering the exfoliated graphite mass measured through the TGA. The estimated extinction coefficient is 4954 ± 135 L g^{1} m^{-1}. The extinction coefficient is calculated as the slope of the curve in **Fig. 39,** which express the absorbance of the FLG-PMMA$_{US}$ dispersion centrifuged at 200 *g*

obtained at 660 nm from different dilutions (1:100, 1:80, 1:60, 1:50, 1:30 and 1:20) in function of the concentration (see section 2.3.6.3). Therefore, the concentrations of the FLG-PMMA$_{US}$ dispersions centrifuged at 4300 *g* and 17000 *g* obtained through OAS are 74.6 ± 0.1 mg L^{-1} and 30.1 ± 0.2 mg L^{-1}, respectively, in agreement with the previous measurements obtained through vacuum filtration.

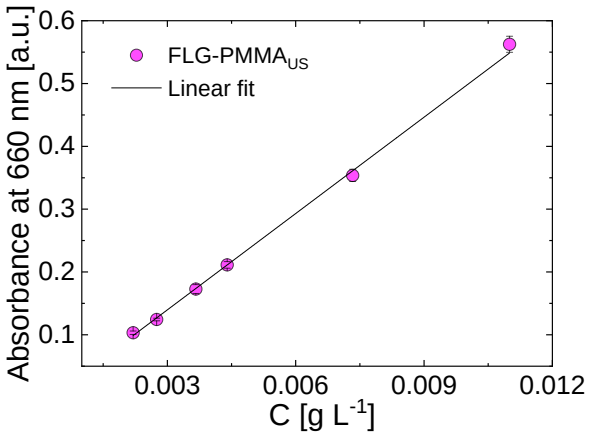

Figure 39 *- Absorbance at 660 nm as a function of the concentration of the FLG-PMMA$_{US}$ dispersion centrifuged at 200 g giving an extinction coefficient of 4954 ± 135 L g^{-1} m^{-1}.*

The obtained results, summarized in **table 4**, indicate that the FLG-PMMA$_{US}$ dispersions contain thinner flakes and present a higher concentration compared to the FLG$_{US}$ dispersions.

Table 4 *– Concentration, percentage of FLG flakes and lateral size of the FLG$_{US}$ and FLG-PMMA$_{US}$ dispersions with the corresponding standard deviations in parenthesis.*

	FLG$_{US}$	FLG-PMMA$_{US}$	FLG$_{US}$	FLG-PMMA$_{US}$	FLG$_{US}$	FLG-PMMA$_{US}$
	@ 200 *g*		@ 4300 *g*		@ 17000 *g*	
C [mg L^{-1}]	80 (20)	220 (40)	30 (10)	90 (0.20)	1 (0.2)	30 (6)
Few layer flakes [%]	36	58	53	70	93	98
Lateral size [nm]	520 (0.57)	600 (0.40)	400 (0.50)	370 (0.43)	300 (0.60)	270 (0.33)

The difference in thickness between the flakes contained in the FLG$_{US}$ and FLG-PMMA$_{US}$ dispersions is due to the stabilization effect of the PMMA. The surface tension of acetone and of the mixture acetone-1 wt % PMMA is analysed, in order to exclude the involvement of this parameter in the stabilization of the flakes. Acetone and the mixture acetone-1 wt % PMMA have surface tensions of

23.8 ± 0.4 and 23.3 ± 0.2 mN m^{-1}, respectively, mismatching the surface energy of the exfoliated flakes. Therefore, in the FLG-$PMMA_{US}$ dispersions, the steric repulsion between the polymer chains, attached to the flakes, is hindering the re-stacking of the flakes. (*340*)

In order to explain the increase in the concentration in the FLG-$PMMA_{US}$ dispersions, the density, ρ, and the viscosity, η, of the mediums for performing the exfoliation are measured (**Table 5**). PMMA does not affect meaningfully the density of acetone, while the viscosity is almost twice compared to the bare acetone.

Table 5 *– Density and viscosity of acetone and the mixture acetone-1 wt % PMMA, with the corresponding standard deviations in parenthesis.*

	ρ [g cm^{-3}]	*η [mPa s]*
Acetone	0.80 (0.02)	0.295 (0.001)
Acetone-1 wt % PMMA	0.77 (0.03)	0.559 (0.001)

The sedimentation coefficient is inversely proportional to the viscosity, so that an increase in the viscosity of acetone corresponds to a decrease of the sedimentation rate of the flakes (see section 1.3.3). (*184*) Therefore, after the centrifugation a higher amount of flakes remains in the FLG-$PMMA_{US}$ dispersions compared to the FLG_{US} ones.

Moreover, the percentage of FLG flakes increases and the concentration of the flakes in the dispersions decreases, when the centrifugal acceleration is raised. When the centrifugal acceleration is increased, a higher centrifugal force is applied to the flakes. (*184*) The thicker flakes contained in the dispersions are the first to precipitate, as they sediment faster compared to the thinner flakes. (*184*) In fact, thicker flakes possess a higher sedimentation coefficient with respect to the thinner flakes. (*184*) Hence, the population of thick flakes, and so the concentration of the overall flakes, in the supernatant decreases as the centrifugal acceleration varies from 200 *g* to 17000 *g*.

The phenomena observed in this study are summarized in the scheme in **Fig. 40**.

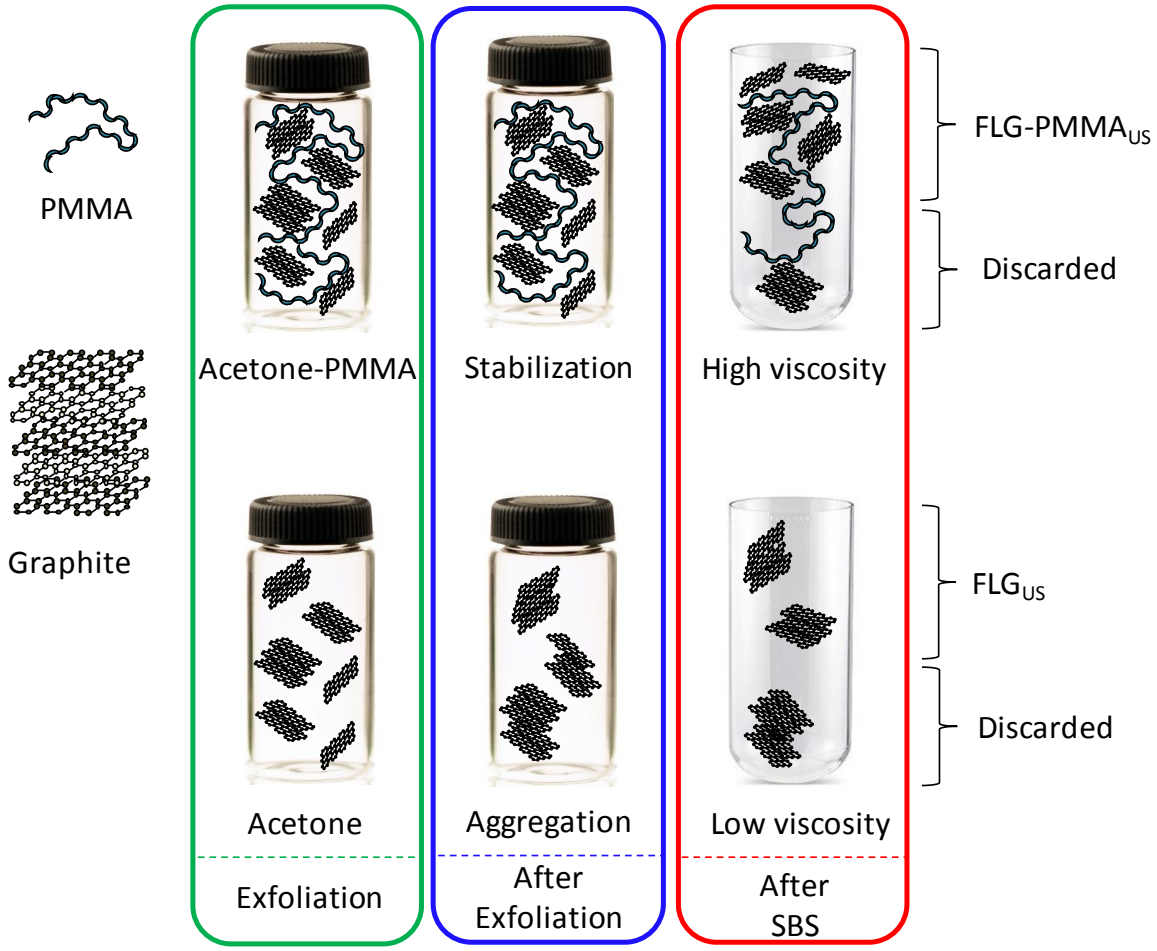

Figure 40 *- Scheme of the production of the FLG$_{US}$ and FLG-PMMA$_{US}$ dispersions: dispersion of graphite in acetone and acetone-1 wt % PMMA, followed by ultrasonication (graphite exfoliation step) and ultra-centrifugation (SBS process).*

3.3 Characterization of the exfoliated graphite-acrylonitrile butadiene styrene (ABS) composites

The mechanical properties of the polymer blends for the production of membranes for gas separation (*362–364*), *e.g.* CO_2 (*364*), are improved by using ABS as a reinforcing polymer. In order to enhance the performance of ABS in the aforementioned blends, it is necessary to improve both

the mechanical and gas barrier properties through the addition of exfoliated graphite flakes into ABS. (*44*)

In this case, the FLG_{US} and FLG-$PMMA_{US}$ dispersions centrifuged at 200 *g* are used to prepare the ABS composites, as their concentration is the highest among the prepared dispersions, *i.e.,* 220 ± 40 mg L^{-1} and 80 ± 20 mg L^{-1} for the dispersions FLG-$PMMA_{US}$ and FLG_{US}, respectively. The presence of PMMA is promotes the distribution of the flakes in the ABS. In fact, PMMA is able to form miscible blends with ABS or its component styrene acrylonitrile, (*351–356*) in which miscibility is defined as the capability of a mixture of polymers to form a single phase (*365*).

The mechanical properties, *i.e.,* the Young's modulus and the tensile strength, are evaluated by tensile testing. In literature (*234*, *264*, *366*), an improvement of the Young's modulus of ca. 64 % is achieved using 8 wt% of commercial GnPs as filler (*234*). However, a decrease in the tensile strength is observed, owing to a poor adhesion between the filler and the matrix, *e.g.,* -9 % with 8 wt% of FLG flakes. (*234*) The functionalization of the FLG flakes with octadecylamine was proposed as a way to solve this issue (*367*, *368*), enhancing the tensile strength, *e.g.,* +32% with 1 wt% of filler (*368*). But, a drop to the value of the pristine polymer of the tensile strength is observed, as the FLG flakes loading is increased up to 3 wt %, due to the aggregation of filler. (*367*, *368*) In our study, the Young's modulus and the tensile strength improve of ~ 22 % and ~ 17 %, respectively (**Fig.41a-b**), compared to the pristine ABS, by using a loading of 0.01 wt% of FLG flakes. The presence of PMMA in the ABS-FLG-$PMMA_{US}$ composites may hinder the aggregation of the FLG flakes, in fact the tensile strength remains constant as the loading of the filler is increased. On the opposite, there is no enhancement of the tensile strength in the ABS-FLG_{US} composites compared to the unfilled polymer, when the loading is increased. Control samples ABS-PMMA are also tested, no improvement is observed in these cases in the Young's modulus and the tensile strength, compared to the pristine ABS (see **Fig. 41c-d**).

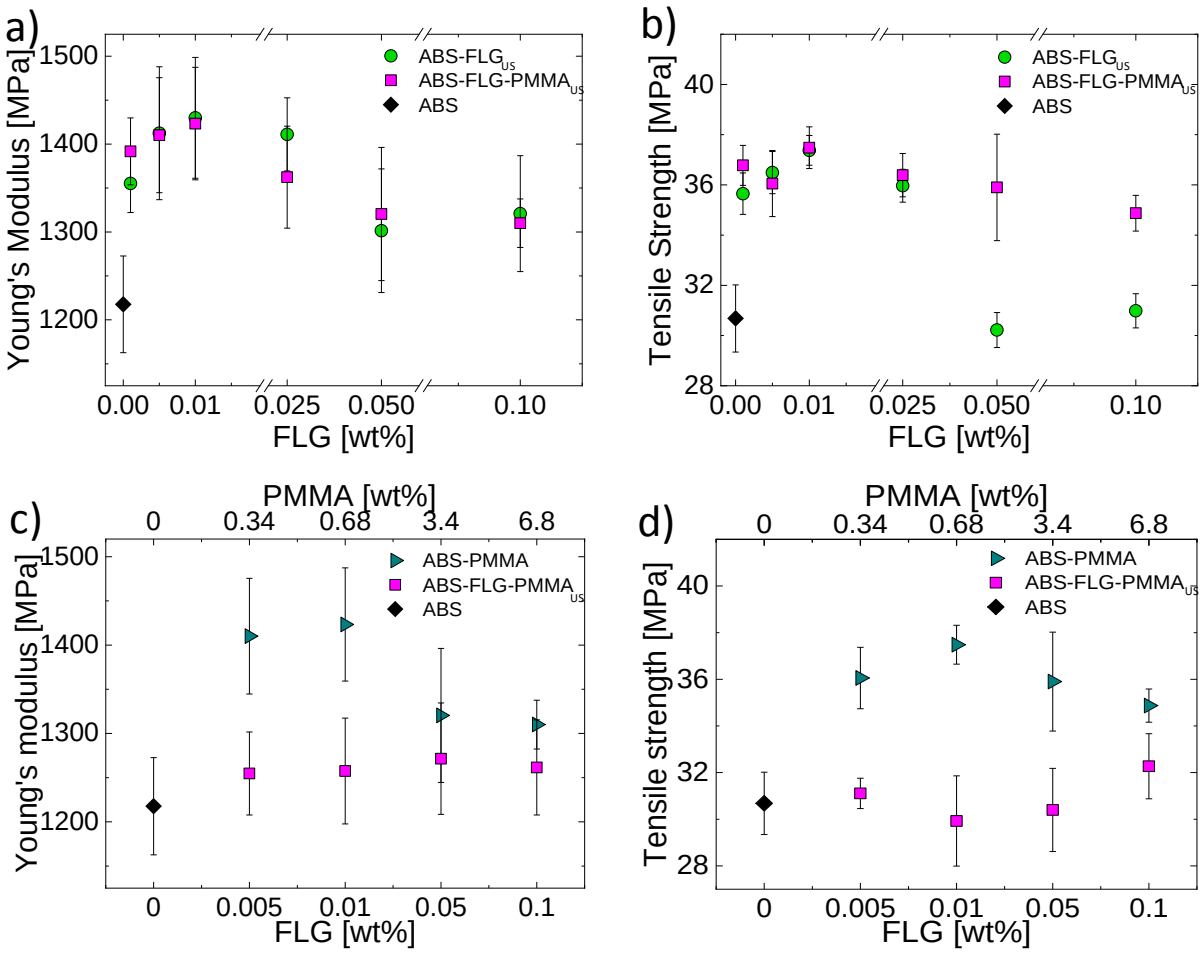

Figure 41 *- a) Young's modulus and b) tensile strength of the pristine ABS and of the ABS-FLG$_{US}$ and ABS-FLG-PMMA$_{US}$ composites with increasing loading of FLG flakes; comparison of the composites ABS-FLG-PMMA$_{US}$ with the control samples ABS-PMMA of c) Young's modulus and d) tensile strength.*

In literature, GnPs are exploited in the polymer composites to hinder the gas permeation.(*289*, *292*, *369*, *370*) In fact, the incorporation of the filler forms a network, which make a tortuous path for the diffusion of gases through the polymer matrix.(*289*, *370*) In our study, the oxygen permeability (OP) of the composites ABS-FLG$_{US}$ and ABS-FLG-PMMA$_{US}$ with 0.1 wt % of filler is dropped of ~ 13 % and ~ 20 %, respectively, compared to the pristine ABS (**Fig. 42a**). In the composites ABS-FLG-PMMA$_{US}$, the OP is ~ 7 % lower than in the ABS-FLG$_{US}$ composites, as both PMMA and the FLG flakes hinder the oxygen passage. A control sample ABS-PMMA not containing the FLG flakes is tested, in order to demonstrate that PMMA is playing a role in the OP decrease. The OP of the

sample ABS-PMMA presents an OP, which is ~ 11 % lower compared to pristine ABS, proving the influence of PMMA on the gas barrier properties in the composites ABS-FLG-PMMA$_{US}$ (**Fig. 42b**).

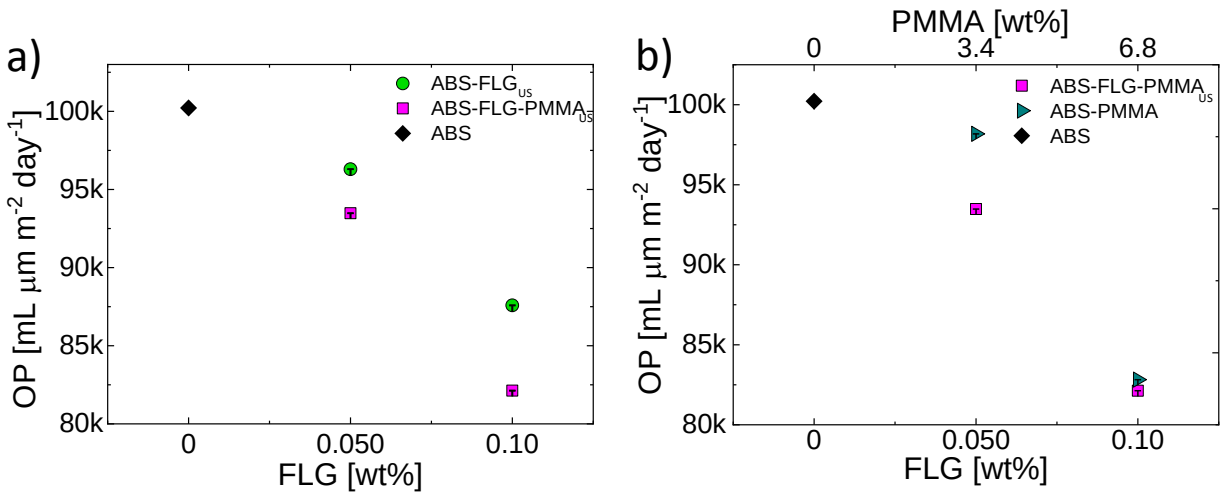

Figure 42 *- Comparison of the Oxygen permeability of c) the pristine ABS vs the composites ABS-FLG$_{US}$ and ABS-FLG-PMMA$_{US}$ and d) of the composites ABS-FLG-PMMA$_{US}$ and of the ABS-PMMA samples.*

3.4 Conclusions

The presence of PMMA enhances the exfoliation of graphite in acetone, in which the PMMA hinders the re-stacking of the exfoliated flakes and slows down the sedimentation of the flakes. In fact, the concentration of the dispersions increases when PMMA is present, *e.g.,* from 80 mg L^{-1} to 220 mg L^{-1} for a centrifugal acceleration of 200 *g*. The Raman spectroscopy proves that the PMMA has no doping effect on the flakes and it does not influence the final lateral size. An enhancement in both the Young's modulus (~ 22 %) and tensile strength (~ 17 %) is achieved in the acrylonitrile-butadiene-styrene (ABS) composites containing few-layer graphene flakes and the ABS composites containing both few-layer graphene and PMMA, by using 0.01 wt % of filler loading. The oxygen permeability was also tested, showing an improvement in the gas barrier properties, as the oxygen permeability has a drop of ~ 20% when the loading is 0.1 wt %.

Chapter 4: Dependence of the graphene flakes morphology for the mechanical reinforcement in acrylonitrile butadiene styrene composites

4.1 Motivation and rationale

In this study, exfoliated graphite dispersions with different morphology, *i.e.,* surface area (*A*) and thickness (*t*), are produced through ultrasonication-based LPE followed by cascade centrifugation steps (see section 2.2.1.2). The morphology of the as-produced graphene flakes is evaluated in terms of lateral size (TEM), surface area (TEM), and thickness (AFM). Then, the prepared flakes having different morphologies are used as filler to prepare ABS composites. In fact, the main goal of this work is to unravel the dependence of the stiffness enhancement of the ABS matrix, as a function of the filler content and flakes morphology. The nearly linear relation between the mechanical reinforcement and A/t^2 ratio is demonstrated. Moreover, a regime of high stiffness is identified at a loading below 0.1 wt % and large A/t^2 values ($\sim 46 \times 10^3$), in which the experimental value of the Young's modulus of the flakes, *i.e.,* 1.28 TPa, which represent an higher value compared to the theoretical one, *i.e.,* 1 TPa (*10*).

4.2 Characterization of the exfoliated graphite flakes

The exfoliated graphite flakes produced through LPE possess a broad distribution of both thicknesses (from monolayer flakes to un-exfoliated material) and lateral size (from few nanometres to micrometres scale). (*72*) The AR of FLG flakes in the graphene-polymer composites plays a crucial role in improving the mechanical properties of the polymer matrix. (*238–242*) Therefore, tailoring the morphological properties of the as-produced flakes would be useful to achieve an insightful understanding of the effect of the AR of the flakes on the mechanical reinforcement in the graphene-polymer composites. Exfoliated graphite dispersions with different morphologies are prepared by exploiting ultra-centrifugation cascades. (*303*) Eight different dispersions are prepared,

using a centrifugal acceleration of 170 g (sample FLG-1), 1000 g (sample FLG-2), 4250 g (sample FLG-3), 9500 g (sample FLG-4) and 17000 g (sample FLG-5). As the centrifugal acceleration increases, the area and the thickness of the flakes decrease. Moreover, the AFM analysis shows that the dispersions contain mostly FLG flakes. **Fig. 43** shows the TEM and AFM images of flakes, with the corresponding statistics of areas and thickness.

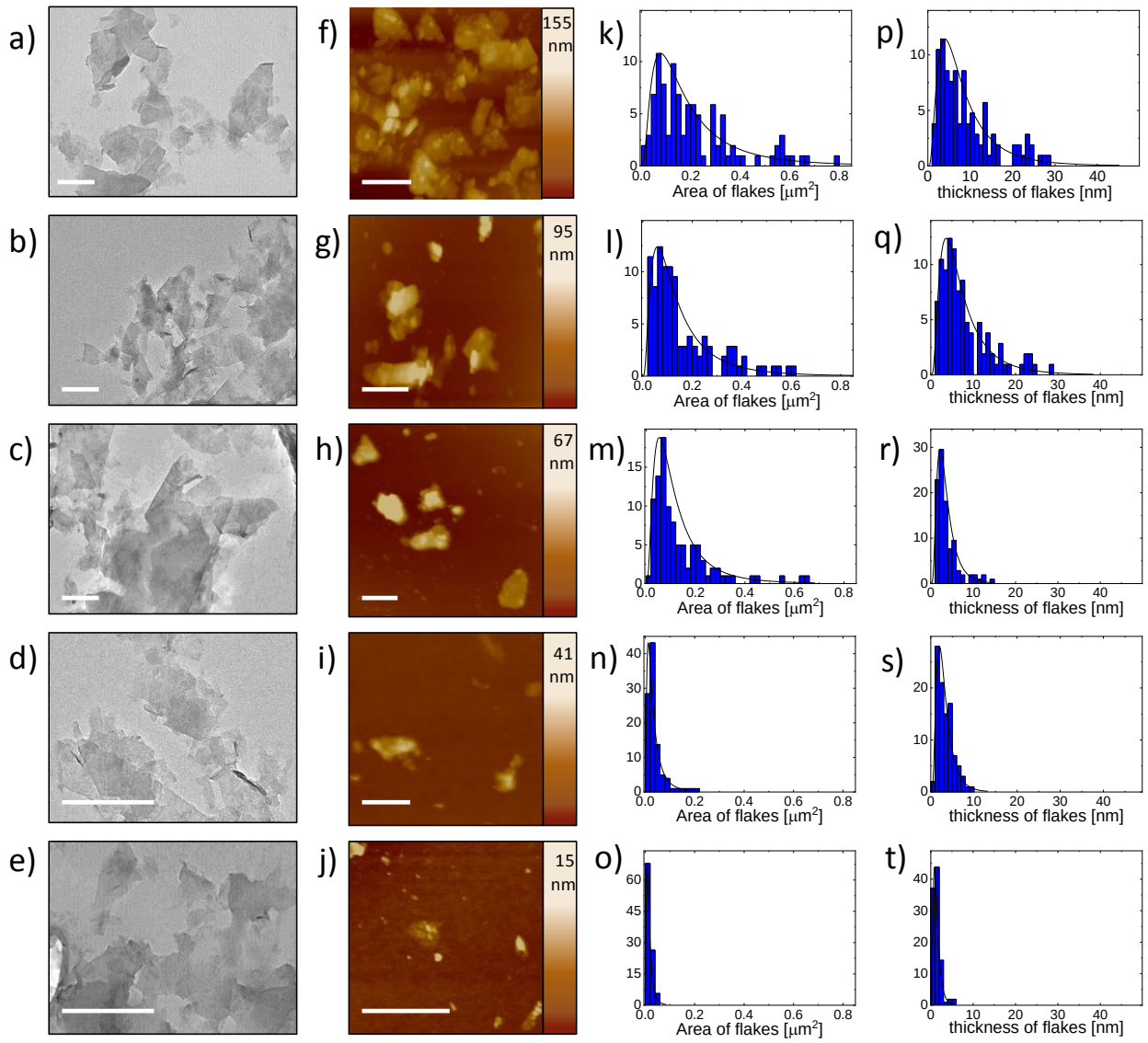

Figure 43 *- Morphological characterization of the graphene flakes obtained by tuning ultra-centrifugation g-forces. a-e) TEM images (scale bars corresponds 500 nm), and (f-j) AFM images of selected flakes (scale bars correspond to 600 nm). Statistical analysis of surface area (k-o) and thickness (p-t) of different graphene flake dispersions.*

The average areas and thicknesses of the flakes contained in the aforementioned dispersions is presented in table 6.

***Table 6**- The A, t, and A/t^2 morphological properties of the flakes contained in the dispersions FLG-1, FLG-2, FLG-3, FLG-4 and FLG-5.*

sample	*A*	*T*	A/t^2
	(μm^2)	(nm)	
FLG-1	0.078	4.2	4421.8
FLG-2	0.059	3.8	4085.9
FLG-3	0.052	2.2	10743.8
FLG-4	0.013	2.1	2947.8
FLG-5	0.008	0.9	9876.5

The samples prepared using cascade centrifugation steps by 170-4250-170 g, 170-4250-170-170 g, and 170-4250-170-170-170 g are FLG-6, FLG-7 and FLG-8, respectively. **Fig. 44** reports the TEM and AFM images of flakes, with the corresponding statistics of areas and thickness.

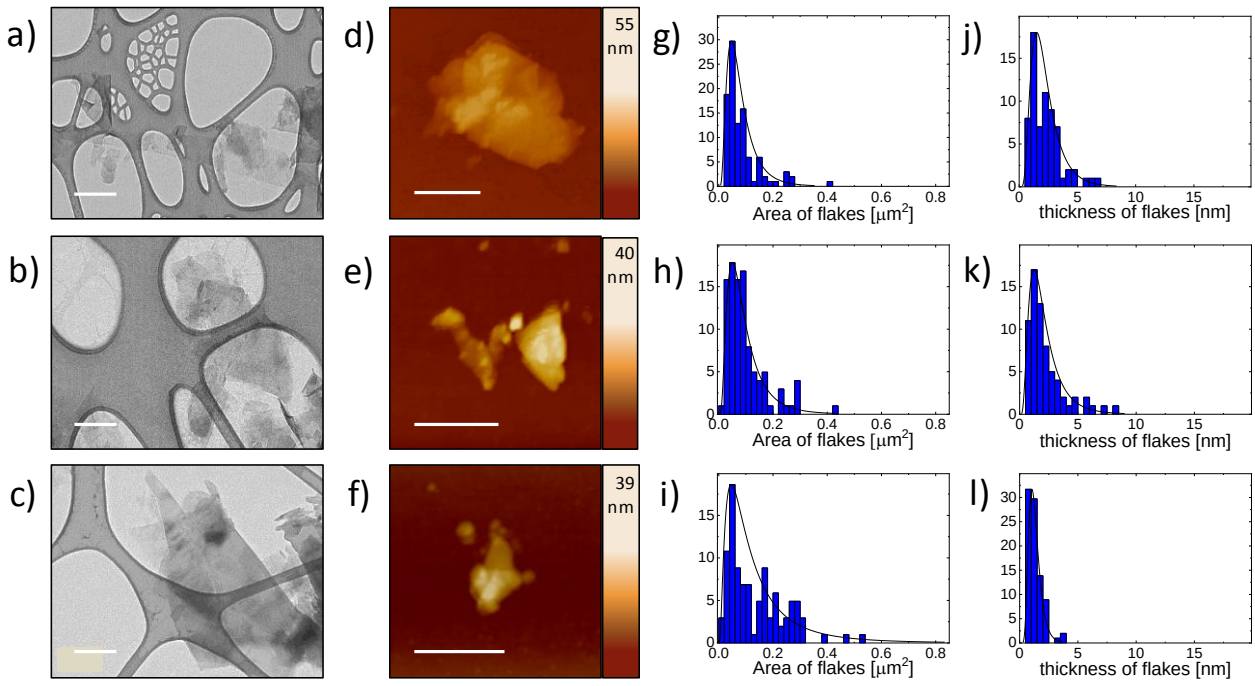

***Figure 44** - Morphological characterization of the 4250 g cascade ultracentrifugation-related flakes. a-c) TEM images (scale bars correspond to 200 nm)., and (d-f) AFM images of selected flakes (scale bars correspond to 500 nm). Statistical analysis on (g-i) surface area and (j-l) thickness.*

The FLG flakes contained in the dispersions are removed in each step of the cascade, so that the resultant supernatants become eventually SLG enriched and the flakes have a similar surface area (see table 7). (*303*)

***Table 7**- The A, t, and A/t^2 morphological properties of the flakes contained in the dispersions FLG-6, FLG-7 and FLG-8.*

Sample	*A*	*T*	A/t^2
	(μm^2)	(nm)	
FLG-6	0.046	1.0	46000.0
FLG-7	0.051	1.2	35416.7
FLG-8	0.048	1.5	21333.3

4.3 Characterization of the FLG-ABS composites

Morphology of pristine ABS and the FLG-ABS composites is investigated by HR-SEM (**Fig. 45**), showing a homogenous distribution of the FLG flakes thorough the ABS matrix.

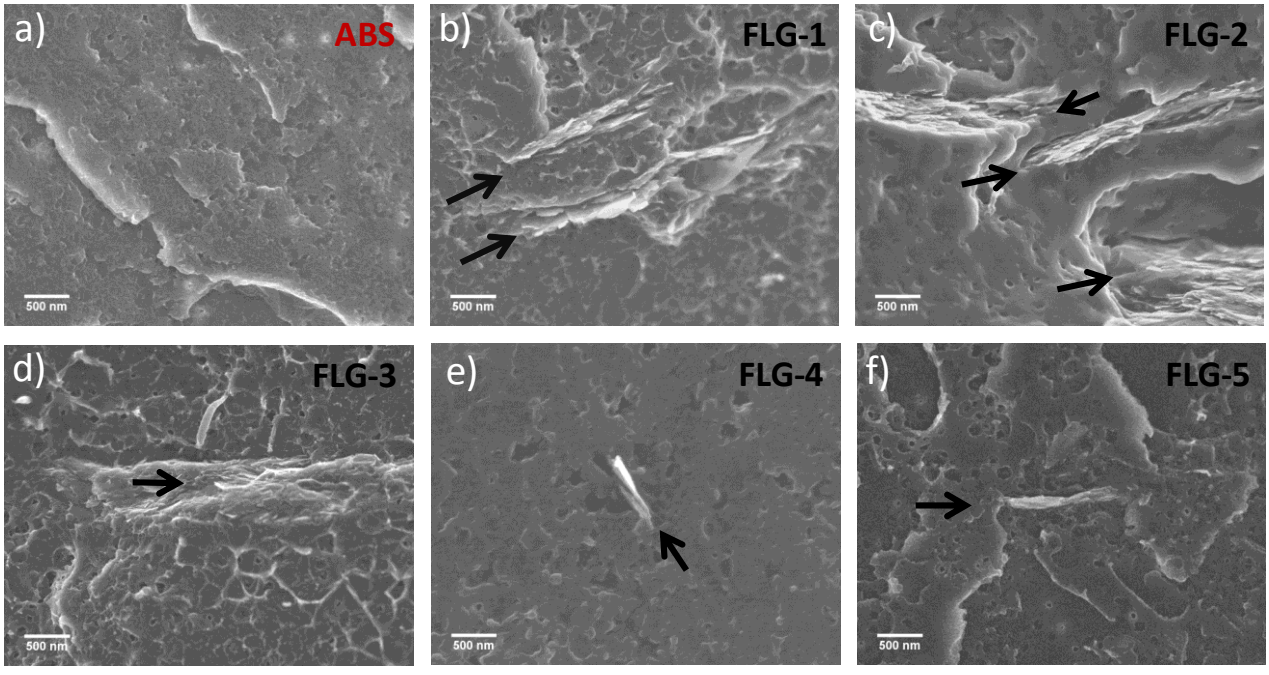

***Figure 45** - HR-SEM images of a) ABS, and the FLG-ABS composites containing b) FLG-1, c) FLG-2, d) FLG-3, e) FLG-4 and f) FLG-5.*

Moreover, HRTEM analysis is used to obtain a further insight on the FLG-ABS interface in the composite containing 0.1 wt % of loading (**Fig. 46**). The aligned FLG flakes with large aspect ratio, *i.e.,* $A/t^2 \sim 40$, are clearly visible (see white triangles in **Figure** 46).

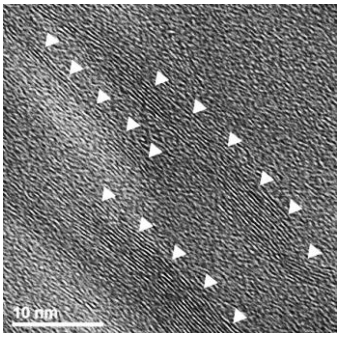

Figure 46 *- HRTEM image of FLG-ABS composite.*

Mechanical tests on both bare ABS and FLG-ABS composites films are performed, measuring the Young's modulus. The beneficial effect of the presence of the FLG flakes on the overall stiffness of the composites is highlighted by the increase of the Young's modulus, when the loading is increased, with respect to the pristine ABS. The Young's modulus of the ABS composites containing the FLG flakes prepared with different centrifugal accelerations (samples FLG-1 to FLG-5) and with the cascade centrifugation (samples FLG-6 to FLG-8) is presented in **Fig. 47a** and **Fig. 47b**, respectively. The maximum improvement, *i.e.* ~ 24 %, in the Young's modulus compared to the pristine matrix is reached using 0.1 wt % of FLG-6 flakes.

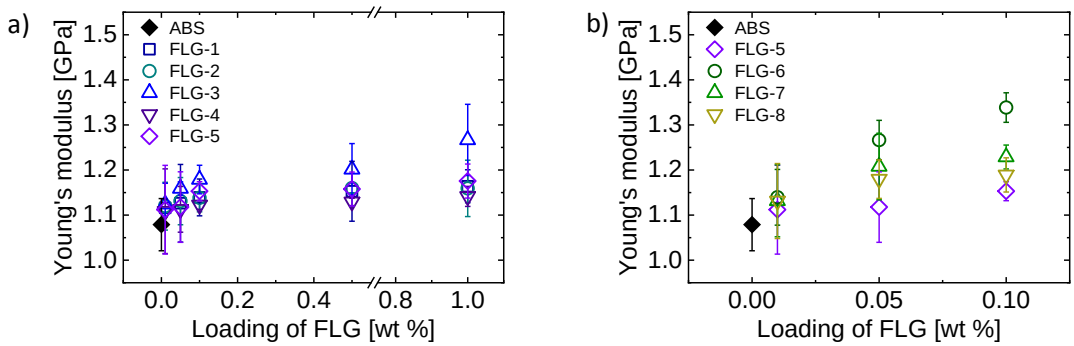

Figure 47 *– Young's modulus of the FLG-ABS composites prepared with a) FLG-1 to FLG-5 and with b) FLG-5 to FLG-8 compared with the pristine ABS.*

The Young's modulus of the composites is expressed in function of different representations of the AR, as *l/t* (Fig. a, e, i), *√A/t* (Fig. b, f, l), *A/t* (expressed in µm, Fig. c, g, m) and A/t^2 (Fig. d, h, n), in order to investigate on the relationship between the enhancement of the polymer properties and the flakes morphology. The values of the Young's modulus are the ones measured for the composites containing 0.01 wt %, 0.05 wt % and 0.1 wt % of loading. The graphs reported in **Fig. 48** show that there is a linear correlation between the Young's modulus and the morphological features *l/t*, *√A/t*, and *A/t* and especially with A/t^2.

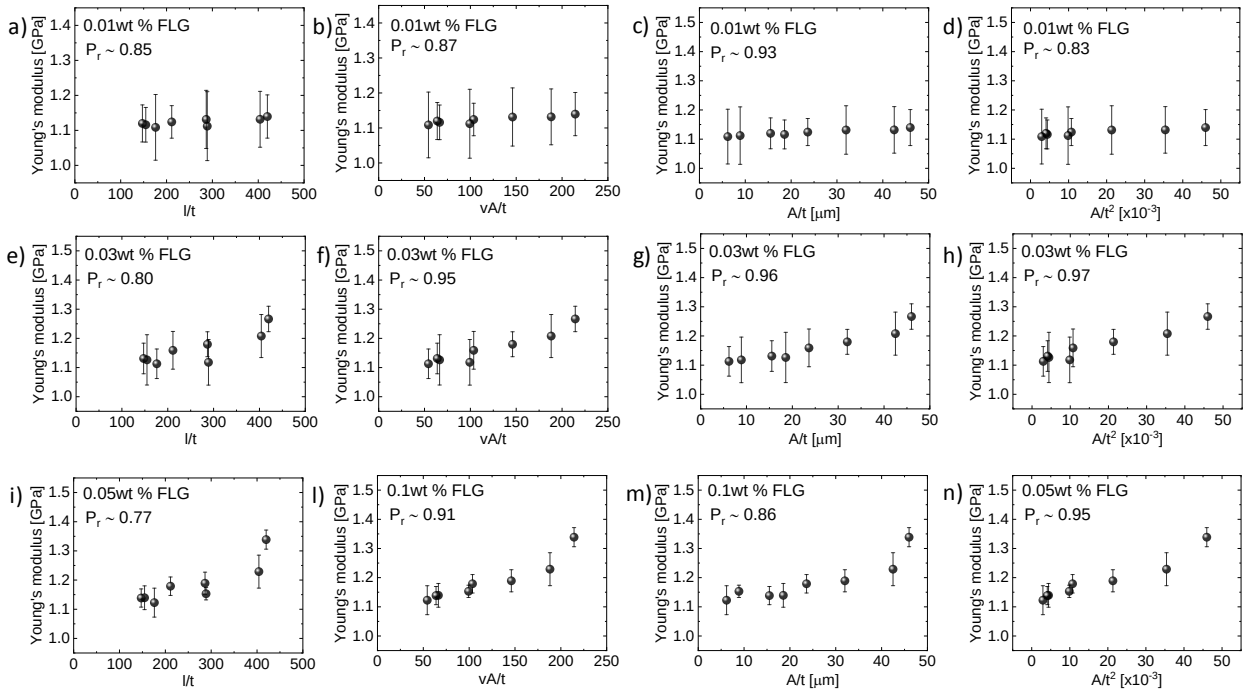

Figure 48 *- Study of Young's Modulus of composites as function of morphological properties, a-e-i) l/t (first column),b-f-l) √A/t (second column), c-g-m) A/t (expressed in µm, third column) and d-h-n) A/t^2 (fourth column), and loading, a-d) 0.01 wt % (first raw),e-h) 0.05 wt % (second raw),i-n) 0.1 wt % (third raw).*

In order to quantify the linear correlation between the morphological parameters and the Young's modulus, the Pearson's coefficient, *i.e.*, P_r (*371*), is evaluated by linearly fitting the values of the Young's modulus and the parameters. The P_r is equal to 1 when there is a perfect linear correlation between two variables, while if it equals zero, it indicates there is no linear correlation between the variables (*371*). Therefore, the variables are linearly related as more as P_r tends toward 1 (*371*).

In our case, P_r values for the correlation between the Young's modulus and the parameter A/t^2 are the highest among the considered parameters. In detail, P_r is equal to 0.97 and 0.95 for the loadings of 0.05 wt % (Fig. h) and 0.1 wt % (Fig. n), respectively. The Cox model can be used to explain this relationship as it predicts indeed a linear relationship, if the ratio of the Young's modulus of the matrix over the filler is negligible (*372*). The reinforcement achieved from a high-modulus filler, as FLG, in a low-modulus matrix, as polymers, can be described by the so-called "rule of mixtures", in which the Young's modulus of the composite YM_c is given by equation 16 (*373*, *374*).

$$YM_c = \varphi_f YM_f + \varphi_m YM_m \quad \textit{Equation 16}$$

In which YM_f and YM_m are the moduli of the filler and the matrix, while φ_f and φ_m are the volume fractions of the filler and the matrix, respectively (*373*, *374*). The rule of mixtures is used to perform a back-calculation of the effective Young's modulus of the FLG flakes (YM_f), to evaluate the effective reinforcement. The results show that for a loading of 0.01 wt %, using the flakes FLG-6 (A/t^2 = 46 × 10^3), the calculated value of YM_f is ~ 1.28 TPa, which is beyond the theoretical values of graphene, i.e., ~ 1.0 TPa (*375*). The back-calculation of the YM_f is performed also for different loadings and A/t^2 values (Fig. 49). The values of the YM_f is found to be below (empty symbols) or beyond (full symbols) the theoretical value, identifying a reinforcement region at a loading of 0.01 wt %.

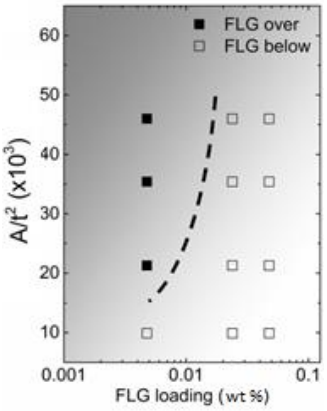

Figure 49 - The back-calculated Young's moduli (YM_f) of the FLG flakes as a function of loading and A/t^2 ratio filled symbols indicate flakes with a YM_f over the theoretical value, whereas empty symbols indicate flakes with a YM_f below the theoretical value.

4.4 Conclusions

In summary, FLG flakes dispersions are produced through the ultrasonication-based exfoliation in N-methyl pyrrolidone. Then, the morphology of the FLG flakes, in terms of area and thickness, is tailored by using sedimentation-based separation with different centrifugal acceleration and cascade centrifugations. The as-prepared FLG flakes are used as filler in the ABS matrix, to study the relationship between the morphology of the flakes and their reinforcing effect on the polymer, evaluating the Young's modulus. The highest improvement, i.e. ~ 24 %, in the Young's modulus, compared to pristine ABS, is reached by using 0.1 wt % of the FLG flakes with the largest area over squared thickness ratio, *i.e.,* A/t^2. The linear correlation between the Young's modulus and the parameter A/t^2 is demonstrated by considering the Pearson's coefficient as discriminating factor. Moreover, back-calculations of the Young's modulus of the FLG flakes have revealed the existence of a reinforcement region at a loading of 0.01 wt %, in which the calculated Young's modulus of the FLG is beyond the theoretical one.

Chapter 5: Wet jet milling graphene and its use in 3D printed polyamide 6-graphene composites for the enhancement of mechanical, tribological and thermal properties

5.1 Motivation and rationale

Polyamide 6 is a thermoplastic polymer, whose mechanical, tribological and thermal properties are exploited in applications as gears (*209*), bearings (*209*), slide blocks (*209*) and structural components in the automotive industry (*376*). This study is focused on the improvement of these properties by the addition of FLG flakes to the polymer matrix. I defined a scalable methodology for the preparation of the composites, starting from the production of the FLG flakes, through wet jet milling, to the manufacturing of the composites, by means of 3D printing. Moreover, a third component as PMMA is used to promote the distribution of the FLG flakes in the PA matrix, assuring the improvement of the desired properties. In fact, the carbonyl group of PMMA interacts with both the filler and the matrix, forming a hydrogen bond. (*345–347*, *357*)

5.2 Features of the wet jet milling graphene dispersion

The morphological properties of the FLG_{WJM} flakes, *i.e.*, thickness, lateral size as well as the concentration in dispersion, are evaluated through Raman spectroscopy, AFM, TEM and OES to assess the quality of the graphite exfoliation process. In **Fig. 49a**, the Raman spectra of graphite (black spectrum) and of the FLG_{WJM} dispersion (blue spectrum) are represented. The Raman spectrum of the FLG_{WJM} dispersion displays all the peaks characteristic of exfoliated graphite and they are normalized to the G peak. The intensity ratios $I(2D_1)/I(G)$ and $I(2D_2)/I(G)$ are considered (**Fig. 49b**), in order to have an insight of the number of layers of the as-produced FLG flakes. In fact, the $I(2D_1)/I(G)$ expressed in function of $I(2D_2)/I(G)$ allows to discriminate the FLG flakes, *i.e*., above the line, from the graphitic flakes, *i.e.,* below the line. (*318*, *319*, *377*) In the aforementioned graph,

the percentage of points corresponding to FLG flakes is around 70 %. The average thickness of the flakes evaluated by the AFM analysis is ~ 3.2 nm, indicating that the flakes are mostly FLG flakes (*358–361*), in agreement with the Raman spectroscopy results (**Fig. 49c**). Moreover, the average value of the distribution of the lateral size of the flakes is ~ 1200 nm, as revealed by the TEM analysis (**Fig. 49d**). The concentration of the FLG flakes in the FLG_{WJM} dispersion is ~ 3 g L^{-1}, as measured through OAS.

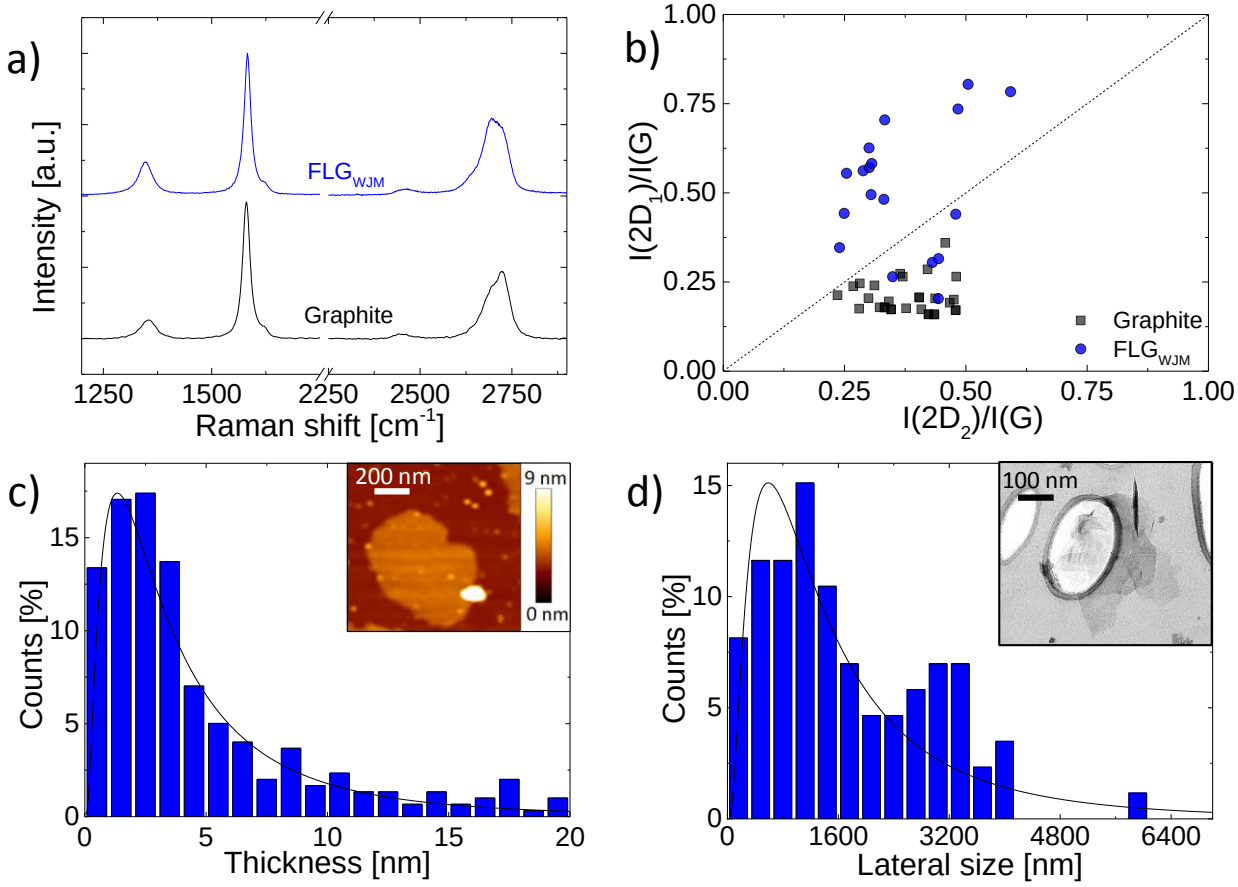

Figure 49 *- Comparison of the graphite (black line) and the dispersion FLG_{WJM} (blue line) a) Raman spectra and b) the normalized intensities $I(2D_2)/I(G)$ vs $I(2D_1)/I(G)$, c) thickness distribution and AFM image of FLG_{WJM} flakes (inset), d) lateral size distribution and TEM image of FLG_{WJM} flakes (inset).*

5.2.1 Morphology of commercial graphene powders

The FLG_{WJM} flakes are compared with the commercial graphene powders by using the lateral size and the thickness of the flakes. Table 8 presents the name and the producing company of the commercial graphene powder with the corresponding lateral size and thickness.

Table 8 *– Comparison of the graphene powders present in the market with the* $FLG_{WJM.}$

Name	Company	Lateral size [μm]	Thickness [nm]	Material
Elicarb materials grade	Thomas Swan (*378*)	~ 6.0	N.D.	GnPs
AV-PLAT-2	Avanzare (*379*)	~ 2.0	~ < 10	~ < 20 layers
AV-PLAT-7	Avanzare (*379*)	~ 7.2	~ 3	N.D.
AV-PLAT-40	Avanzare (*379*)	~ 40	~ 10	~ < 30 layers
AV-PLAT-70	Avanzare (*379*)	~ 70	~ 10	~ < 30 layers
G2NAN	Nanesa (*380*)	~ 50	N.D.	GnPs
AO-1 grade	Graphene Supermarket (*381*)	~ 10	~ 1.6	~ < 3 layers
AO-2 grade	Graphene Supermarket (*381*)	~ 5	~ 8	~ 20-30 layers
AO-3 grade	Graphene Supermarket (*381*)	~ 4.5	~ 12	~ 30-50 layers
AO-4 grade	Graphene Supermarket (*381*)	~ 7	~ 60	N.D.
A-12 grade	Graphene Supermarket (*381*)	~ 2-8	~ > 3	~ 3-8 layers
C-1 grade	Graphene Supermarket (*381*)	~ 5-25	~ 5-30	N.D.
xGnPs Grade R	XG Science (*382*)	~ 25	N.D.	GnPs
XGnPs Grade C	XG Science (*382*)	~ < 2	N.D.	GnPs
Nanene	Versarien (*383*)	~ < 10	N.D.	~ < 10 layers
GNP-HP	Versarien (*383*)	~ < 27	N.D.	~ < 10 layers
FLG_{WJM} (our material)	-	~ 1.2	~ 3.2	FLG

5.3 Results of the characterization of the graphene-polyamide 6 composites

Polyamide 6 (PA) is used as material for gears (*209*), bearings (*209*), slide blocks (*209*) and structural components in the automotive industry (*376*). The performance of this polymer in the aforementioned applications can be improved by adding FLG flakes as filler. In fact, the FLG-PA composites present enhanced mechanical, tribological and thermal properties with respect to the pristine polymer. (*297*, *298*, *384–386*) As addressed in chapter 1, a homogeneous distribution of the flakes in the matrix is required to obtain an improvement in the desired properties. The enhancement of the mechanical properties in FLG-polymer composites is based on the transfer of the stress from the matrix to filler. (*44*, *270*) But, aggregates reduce the available area of the filler for the stress transfer, which is less efficient than in the case of well-distributed flakes. (*255*, *272*, *273*) About the tribological properties, in FLG-polymer composites, the FLG flakes protect the polymer matrix from wear by forming a protective layer both on the surface of the rubbing counterpart and of the sample. (*232*, *297–299*) It is necessary to distribute the flakes homogenously in the matrix, as aggregates tend to hinder the formation of the protective layer, worsening the wear of the surface of the polymer. (*298*, *302*) The thermal properties are also influenced by the distribution of the flakes in the pristine polymer. In graphene, the heat propagates quickly through phonons owing to its crystalline structure. (*278*, *279*) But, when the FLG flakes are inside the polymer matrix, the phonons are scattered at the FLG-polymer interface, slowing down the heat propagation. (*280*) A homogeneous distribution of the FLG flakes is necessary to reduce the scattering and promote the heat transfer in the matrix. (*223*, *255*, *287*)

In this study, PMMA is used to promote the distribution of the flakes in the polymer matrix, as the carbonyl group of PMMA interacts with the amide group of PA in PMMA/PA blends and with the FLG flakes through hydrogen bonding (*345–347*, *357*). Therefore, the goal of the following

paragraphs is to investigate the effect of PMMA on the distribution of the flakes in the matrix and how this will be reflected on the mechanical and tribological properties of the composites.

The lyophilized powder obtained from the FLG_{WJM} dispersion is used to prepare the PA-composites (section 2.2.2). The composites PA-FLG_{WJM} contain just FLG flakes, while in the composites PA-PMMA-FLG_{WJM} there are both graphene flakes and PMMA.

The area of the cross section of the 3D printed samples is analysed through SEM and Raman-mapping. The SEM images show that the composite PA-3FLG_{WJM} presents aggregates, highlighted by the white squares (**Fig. 50a**). On the contrary, the composite PA-PMMA-3FLG_{WJM} shows a good distribution of the flakes, marked by the white circles (**Fig. 50b**). Examples of an aggregate and of a flake sticking out from the cross section area are represented in the insets of the **Fig. 50a** and **Fig. 50b**, respectively.

In order to confirm the difference in the distribution of the flakes observed in the SEM images, the Raman mapping is performed and a map is obtained by integrating the intensity of the G peak of the FLG flakes. Therefore, the white colour corresponds to the only polymer zones, as the G peak is not detected in the collected spectra. Instead, the green and magenta zones represent the collected spectra where the G peak is present (*i.e.*, presence of FLG flakes) for the composites PA-FLG_{WJM} and PA-PMMA-FLG_{WJM}, respectively (see **Fig. 50c-d**). The results of the Raman mapping indicate that the FLG_{WJM} flakes possess a more homogeneous distribution in the PA-PMMA-FLG_{WJM} composites compared with the PA-FLG_{WJM}. In fact, in the map of the composite PA-3FLG_{WJM}, the exfoliated flakes have a poor distribution (**Fig. 50c**) and in the composite PA-PMMA-3FLG_{WJM} the flakes are homogenously distributed (**Fig. 50d**).

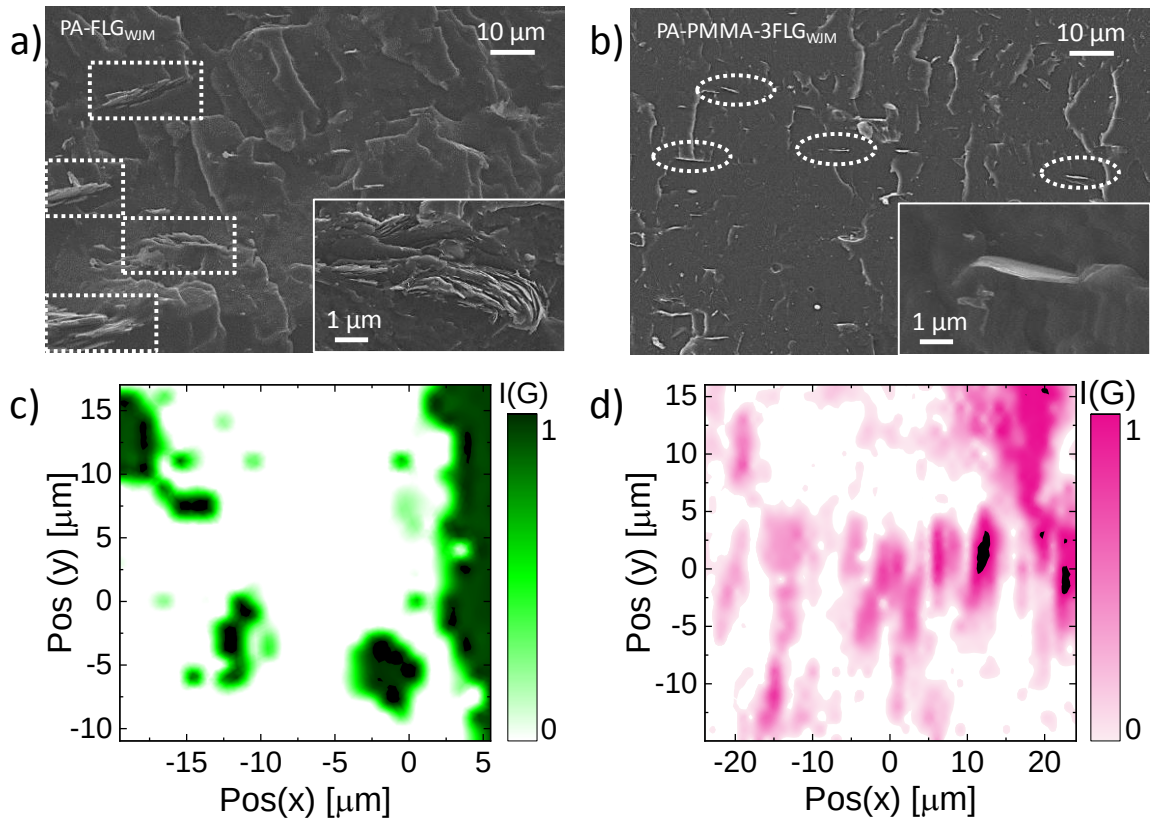

Figure 50 *- SEM images of the composites a) PA-3FLG$_{WJM}$ (aggregates in the white squares), the zoom in the inset is showing an aggregate and b) PA-PMMA-3FLG$_{WJM}$ (well distributed flakes in the white circles), the zoom in the inset presents a flakes sticking out of the analyzed surface, Raman mapping of the composites c) PA-3FLG$_{WJM}$ and d) PA-PMMA-3FLG$_{WJM}$.*

The composites PA-FLG$_{WJM}$ and PA-PMMA-FLG$_{WJM}$ containing 1 and 3 wt % of FLG flakes and the samples PA-PMMA prepared with 1 and 3 wt % of PMMA are tested through tensile testing. The measured mechanical properties are the Young's modulus and the tensile strength. As it is represented in **Fig. 51a**, when the loading is raised, the Young's modulus increases for both composites PA-FLG$_{WJM}$ and PA-PMMA-FLG$_{WJM}$, in agreement with the literature data (*297*, *387*–*392*). An enhancement of 130 % and 160 % is achieved for the composites PA-3FLG$_{WJM}$ and PA-PMMA-3FLG$_{WJM}$, respectively, compared to the pristine polymer (see **Fig. 51a**). The tensile strength has an improvement of 60 % and 100 % for the composites, PA-FLG$_{WJM}$ and PA-PMMA-FLG$_{WJM}$, respectively (**Fig. 51b**). In literature (*385*, *393*, *394*), the aggregation of the FLG flakes in the matrix in the FLG-PA composites leads to a lower value in the tensile strength with

respect to composites having homogeneously distributed FLG flakes. Therefore, the fact that the tensile strength is constant with the increase in the loading, for the PA-PMMA-FLG$_{WJM}$, can be attributed to an improvement in the distribution of the FLG flakes owing to PMMA, as observed in the morphological analysis. Moreover, the Young's modulus and tensile strength of the samples PA-PMMA are 100 % and 90 % lower compared to the composites PA-PMMA-FLG$_{WJM}$. (**Fig. 51a-b**) These results indicate that the improvement observed in the mechanical properties of the composites is mainly due to the addition of the FLG flakes.

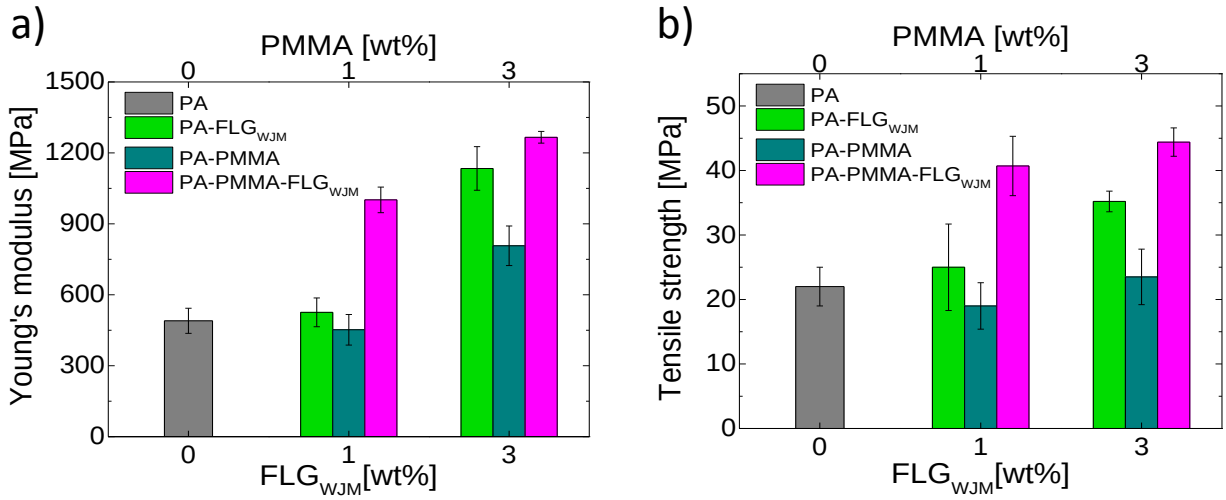

Figure 51 *- a) Young's modulus and b) tensile strength of pristine PA (grey column), PA-FLG$_{WJM}$ composites (green column), PA-PMMA control samples (cyan column), PA-PMMA-FLG$_{WJM}$ composites (magenta column).*

The measured tribological properties are the steady coefficient of friction (μ) and the wear rate (K). The required steady coefficient of friction depends on the final use of the material, for example, a friction as low as possible is necessary for applications as gears and bearings, while the opposite is needed for other applications, *e.g.,* hose clamps, fasteners, etc.. (*376*). Instead, the wear rate (*K*) indicates the wear of the surface of the samples when a constant load is applied during the cyclic sliding of a steel ball.

The FLG flakes are considered as solid lubricant, the low friction of this material originates from the interlayer shear, facilitated by the weak bonding between the layers. (*207*, *395*) Therefore, in literature (*297*, *298*, *385*), the FLG flakes are used to decrease the μ of the PA matrix. The steady coefficient of friction (μ) is measured for both the composites PA-FLG_{WJM} and PA-PMMA-FLG_{WJM}. The μ has an increment of 20 % and 90 % in the composites PA-FLG_{WJM} and PA-PMMA-FLG_{WJM}, respectively, compared to PA (**Fig. 52**). The μ is expected to decrease with the FLG loading according to the studies present in literature (*297*, *298*, *385*). Further analysis need to be performed in order to understand this phenomenon.

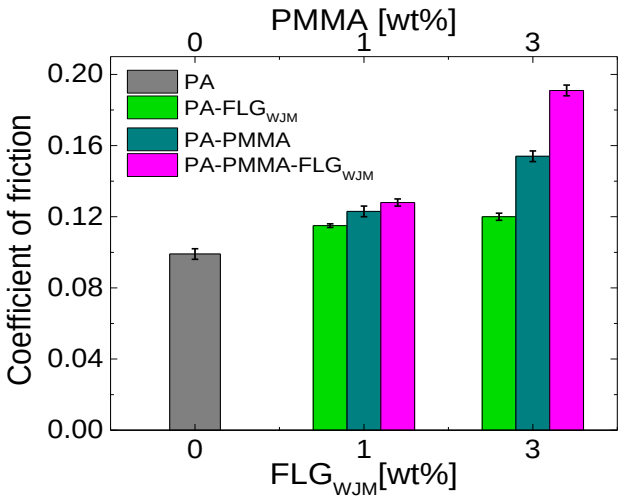

Figure 52 *- Steady coefficient of friction (μ) of pristine PA (grey column), PA-FLG_{WJM} composites (green column), PA-PMMA control samples (cyan column), PA-PMMA-FLG_{WJM} composites (magenta column).*

The *K* of the composite PA-PMMA-1FLG_{WJM} decreases of 50 % compared to PA (**Fig. 53a**) and its sliding path is smooth with no debris (**Fig. 53b**). The mechanism of wear-hindering in FLG-polymer composites consists in the formation of a protective film on the steel ball, while the graphene-based flakes form a "film" on the surface of the sample, reducing the friction. (*299*, *302*, *396*) This phenomenon is observed in the composite PA-PMMA-1FLG_{WJM}, in fact there are FLG flakes on the surface of the sample, as shown in **Fig. 53b**. However, there is a drastic increase in the *K* of PA-3FLG_{WJM} of 230 % with respect to PA (**Fig. 53a**). Instead, the *K* of PA-PMMA-3FLG_{WJM} has an

increment of 108 % in comparison with PA, but it is 122 % lower than the composite not containing PMMA. (**Fig. 53a**) The sliding paths of both the composites present debris on the edges and longitudinal cracks. (**Fig. 53c-d**) This phenomenon may be due to the presence of aggregates, which detach from the sample surface during the testing and act as an abrasive body between the sample and the steel ball, hindering the formation of the protective films. (*298*) As it can be observed from the enlargements of the SEM images, in the case of the composite PA-PMMA-3FLG$_{WJM}$, the surface of the sample is covered by the FLG flakes (**Fig. 53c**), unlike the surface of the composite PA-3FLG$_{WJM}$ (**Fig. 53d**). This may explain the lower value of *K* in PA-PMMA-3FLG$_{WJM}$, as during the testing there are the FLG flakes protecting the surface from wear, as explained earlier, but there are also aggregates hindering the protective mechanism. Moreover, as it can be noticed from **Fig. 53a**, the PMMA affects slightly the *K* of PA as the PA-PMMA samples have a maximum increase of 22 % compared to PA.

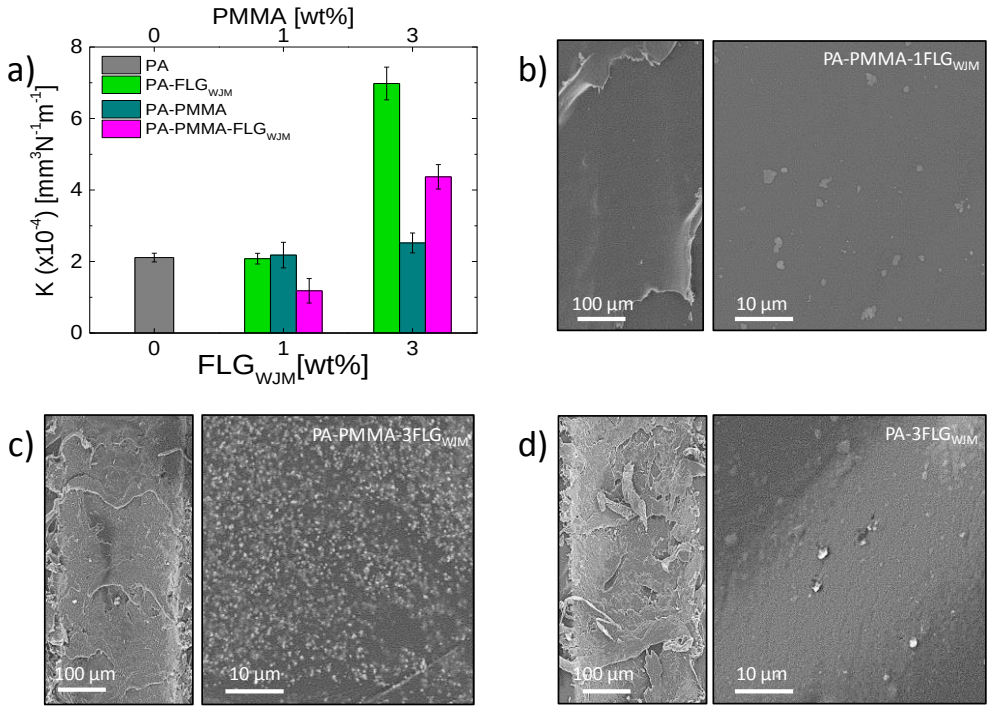

Figure 53 *- a) Comparison of the wear rate (K) of the composites PA-FLG$_{WJM}$ (green column), PA-PMMA-FLG$_{WJM}$ (magenta column) and the samples PA (gray column) and PA-PMMA (cyan column), SEM images of the sliding paths with their magnification of b) PA-PMMA-1FLG$_{WJM}$, c) PA-PMMA-3FLG$_{WJM}$ and d) PA-3FLG$_{WJM}$.*

The heat transfer of PA through the material itself needs to be improved, as heat is generated when extensive friction occurs. In this regard it is preferable to choose a material able to dissipate heat, assuring the durability of the component. (*397*)

Thermal imaging is performed by heating the samples at 60 °C for 20 seconds, in order to compare the heat transfer of the pristine polymer with the one of the composites.

The results (**Fig. 54a**) show that the pristine PA and the sample PA-3PMMA both reach a temperature of 26°C after 20 s, indicating that the PMMA does not affect the heat transfer in PA (**Fig. 54b-c**). Instead, in the composites PA-3FLG$_{WJM}$ (**Fig. 54d**) and PA-PMMA-3FLG$_{WJM}$ (**Fig. 54e**), the temperature increases to 52 °C after 20 s, owing to an improved heat transfer compared to the pristine polymer. In fact, in literature (*388*, *398–401*), FLG flakes are known to increase the thermal conductivity of the PA matrix.

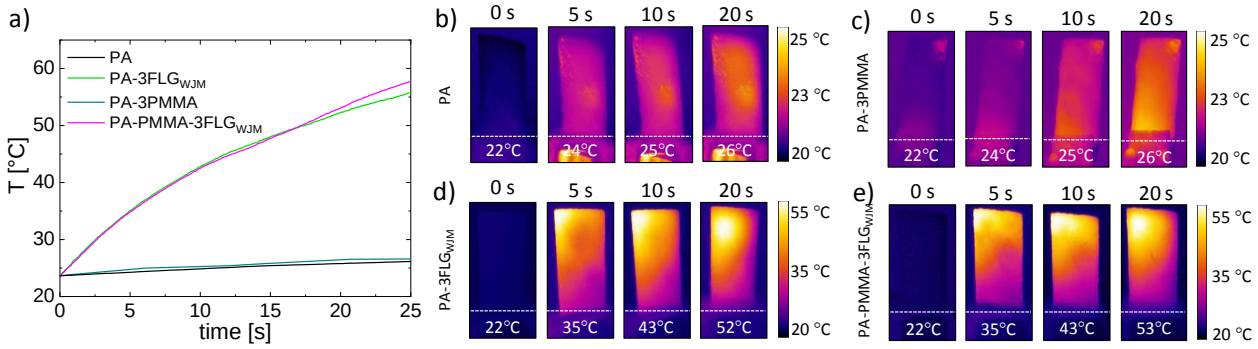

Figure 54 *– a) Average temperature in function of time of the samples PA, PA-3FLG$_{WJM}$, PA-3PMMA, PA-PMMA-3FLG$_{WJM}$, thermal images of b) PA, c) PA-3PMMA, d) PA-3FLG$_{WJM}$ and e) PA-PMMA-3FLG$_{WJM}$.*

5.4 Conclusions

The graphene-polyamide 6 composites are produced using scalable methods, starting from the production of few layer graphene by wet jet milling, passing through the processing and the manufacturing of the composites by using extrusion and 3D printing. The poly methyl methacrylate (PMMA) is used as additive to improve the few-layer graphene flakes distribution into the matrix polyamide 6, which results in an enhancement in both the mechanical and tribological properties. The Young's modulus and the tensile strength of the composites containing PMMA and 3 wt % of few-layer graphene flakes reach an improvement of 160 % and 100 %, respectively, compared to the pristine polymer. Moreover, the composite containing both PMMA and few-layer graphene flakes (1 wt %) presents an increase of 30 % in the steady state coefficient of friction and a decrease of 50 % in the wear rate with respect to the unloaded polymer. The thermal transfer is improved in both the composites containing just few-layer graphene flakes (3 wt %) and the composites containing both PMMA and few-layer graphene flakes (3 wt %). In fact, the pristine polyamide 6 reaches a temperature of 25 °C after 20 s under the heating source, while for the composites the temperature value is doubled (50 °C) with respect to the virgin polyamide 6. This result indicates that PMMA is not affecting the thermal properties of the material. These features make the composite containing 1 wt % of few-layer graphene and PMMA, potentially suitable for applications, where friction and resistance to wear are required, *e.g.,* hose clamps and fasteners.

Chapter 6: Wet jet milling graphene - elastomer composites: effect of processing on the mechanical and thermal properties

6.1. Motivation and rationale

The styrene-butadiene (SB) copolymer is a thermoplastic elastomer, which is typically used for applications in sporting goods and hot-melt adhesives. (*402*) Styrene-butadiene has similar properties to thermosetting rubbers as a high elongation at break, *i.e.,* 680 %, and, unlike thermosetting rubbers, there is no need of the vulcanization step. (*403*) Moreover, SB can be re-processed, making it compatible with the manufacturing processes and suitable for recycling. (*403*) The goal of the PhD activity reported in this chapter was to improve the mechanical, thermal and electrical performance of the SB pristine polymer, introducing graphene for applications in electronics, *e.g.,* all plastic electronic circuits. The as-produced composites are not electrically conductive, as the graphene flakes did not form a percolative path inside the matrix. Therefore, the mechanical and thermal properties of the graphene-SB composites are analysed, in order to be potentially useful as materials for heat sink for electronics packaging. Moreover, the graphene-SB composites are produced using scalable and industrially compatible techniques, starting from the production of graphene-based flakes, using wet jet milling. (*154*) Two different techniques are used to manufacture the graphene-SB composites, *i.e*., compression and injection moulding techniques, in order to analyse their effect on the mechanical and thermal properties.

6.2 Results of the characterization of the elastomer-graphene composites

The samples used for the mechanical and thermal characterization are manufactured using injection moulding and compression moulding, on the pellets obtained by extrusion.

6.2.1 Mechanical testing

In **Fig. 55a-b** can be observed that the Young's modulus and the tensile strength of both the samples produced by injection moulding (IM) and compression moulding (CM) increase with the FLG_{WJM} loading with respect to the pristine SB. In literature (*404*, *405*), the reinforcement effect at 20-45 wt % loading is attributed to the uniform distribution of the FLG flakes in the matrix. A homogeneous distribution of the flakes in the matrix is fundamental to provide an efficient stress transfer from the matrix to the filler. (*255*, *272*, *273*) When there are aggregates in the matrix, the area of the flakes available for the stress transfer is reduced, and so the reinforcing effect of the flakes is not as efficient as in the case of homogenously distributed flakes. (*255*, *272*, *273*)

The IM samples show a better mechanical performance compared to the CM samples. In fact, the Young's modulus of the IM samples and the CM samples have an improvement of 60 % and 45 %, respectively, compared to the pristine polymer. For what concern the tensile strength, it is enhanced by 40 % in the CM samples and 46 % in the IM samples, compared to the unloaded matrix.

In literature has been reported that (*405*) when injection moulding is used to manufacture the samples, the flow of the molten composite into the mold induces the alignment of the FLG flakes along the flow direction. During the mechanical testing of the composite, if the alignment of the flakes is parallel to the direction of the applied tensile load, the reinforcing effect of the flake on the matrix is better than in the case of randomly oriented flakes. (*249*, *257*, *270*, *271*)

Therefore, the difference in the mechanical performance of the IM and CM samples is due to the different orientation of the FLG_{WJM} in the matrix, given by the manufacturing technique. This

hypothesis will be demonstrated through the morphological analysis of the cross section of the dog-bone samples.

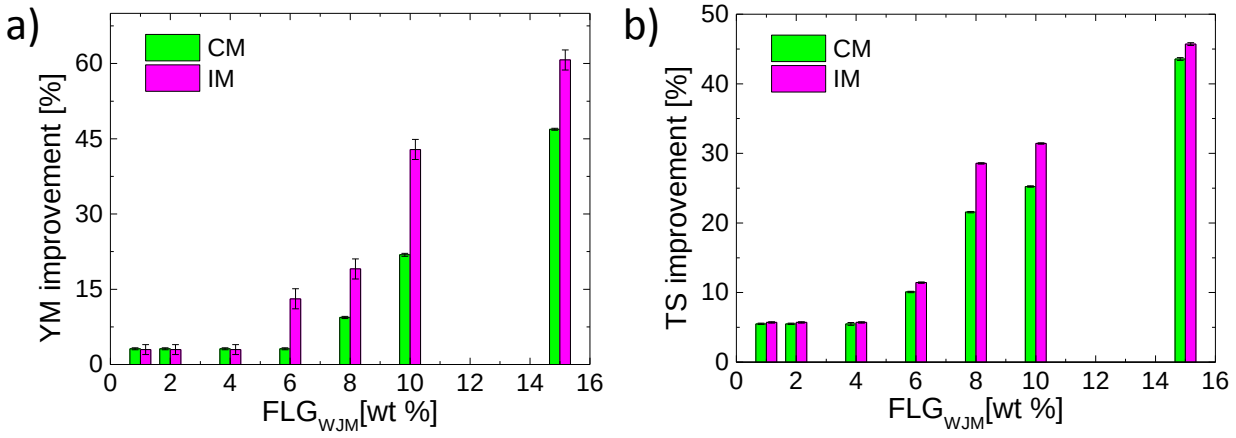

Figure 55 *- Comparison of a) the Young's modulus (YM) and b) the tensile strength (TS) of the composites produced through compression moulding (CM) (green) and injection moulding (IM) (magenta).*

6.2.2 Thermal properties

The thermal conductivity of the composites IM and CM increases compared to the pristine SB, by the increasing the FLG_{WJM} percentage from 1 wt % to 15 wt %. This improvement is not caused by the formation of a percolative path in which the FLG_{WJM} are touching each other as it will be revealed in the morphological analysis. On the contrary, the presence of the FLG_{WJM} facilitates the heat transfer through the insulating matrix, resulting in an enhancement of the thermal conductivity, in agreement with literature data. (*406*, *407*)

The CM and IM samples reach an improvement of 170 % and 110 %, respectively, using 15 wt % of FLG compared to the SB polymer (**Fig. 56**). The better performance of CM samples may be owing to the difference in the orientation of the flakes in the disk samples compared to the IM samples. In fact, as stated in Chapter 1, the orientation of the graphene flakes plays a crucial role. In fact, if the flakes themselves are aligned along the testing direction, the heat transfer is more efficient than in the case of having randomly oriented flakes. (*257*, *285*, *286*)

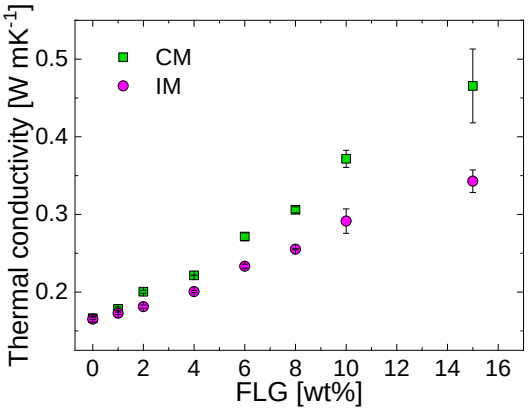

Figure 56 *- Thermal conductivity of the SB-FLG composites produced through compression moulding "CM" and injection moulding "IM".*

6.2.3 Morphological analysis

The distribution of the flakes on the cross section area of extruded filaments is analysed by means of SEM. The flakes are aligned along the extrusion direction, protruding from the analysed surface (**Fig. 57**). Moreover, the distribution of the flakes is homogeneous at 15 wt% of FLG_{WJM} loading.

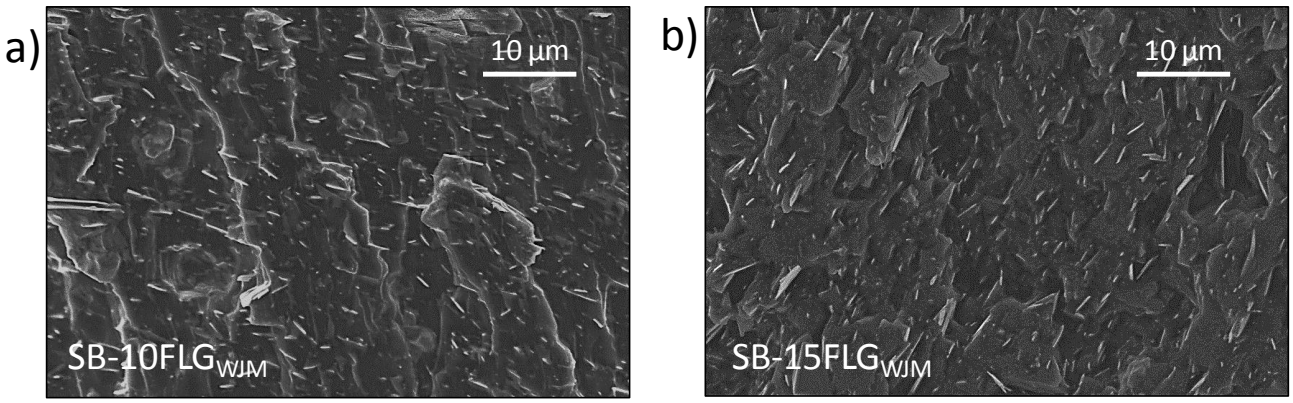

Figure 57 *- SEM images of the area of the cross section of the extruded filaments of, a) SB-10FLG$_{WJM}$ and b) SB-15FLG$_{WJM}$.*

The cross section of the dog-bone and disk-shaped samples is analysed, in order to demonstrate the different orientation of the FLG_{WJM} in the CM and IM samples, corroborating the hypothesis exploited to explain the improvements observed in the mechanical and thermal properties.

According to the hypothesis, the morphological analysis should show that the orientation of the flakes is parallel to the applied tensile load in the IM dog-bone samples, following the injection flow direction, and randomly oriented in the CM dog-bone samples (see **Fig.58a**). The IM disk-shaped sample should contain flakes, which are orthogonal to the direction used to test thermal conductivity and parallel to the injection flow, while the CM disk-shaped samples should present randomly aligned flakes (see **Fig.58b**).

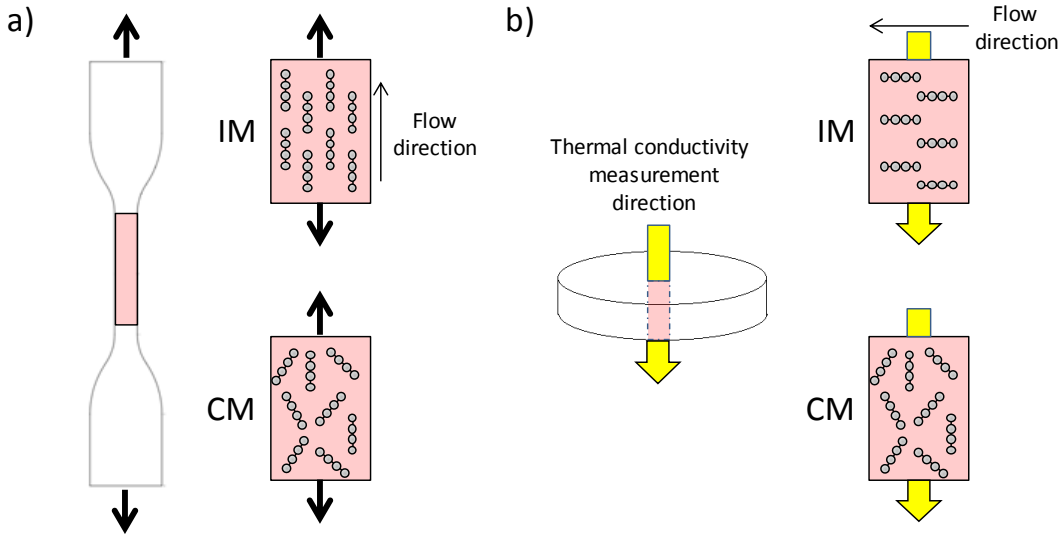

Figure 58 *–Scheme showing the orientation of the flakes in a) dog-bone samples and b) disk-shaped samples.*

The orientation of the flakes into the matrix is analysed through the measurements of the angle between the flakes protruding from the cross-section and the surface of the composite. A scheme is presented in **Fig. 59**, showing how the angle was considered during the measurements.

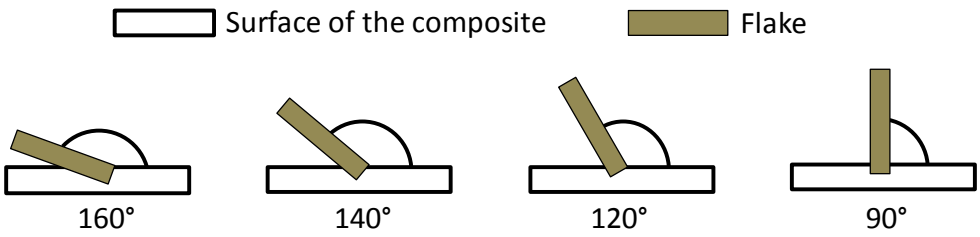

Figure 59 *- Scheme representing some examples of angles measured between the flake and the surface of the composite on the SEM image.*

The flakes in the IM dog-bone sample seem to be oriented along the direction of the tensile load (red circles) (see **Fig. 60a**). On the contrary, the dog-bone sample produced by CM presents randomly oriented flakes (yellow boxes) (**Fig. 60b**). These trends are confirmed by the measurements of the flakes angles. In fact, for the IM sample, the values of the angle of the flakes are mainly focused around 90 °. While, on the contrary, in the CM sample the values of the angle of the flakes have a range between 90 ° and 165 °.

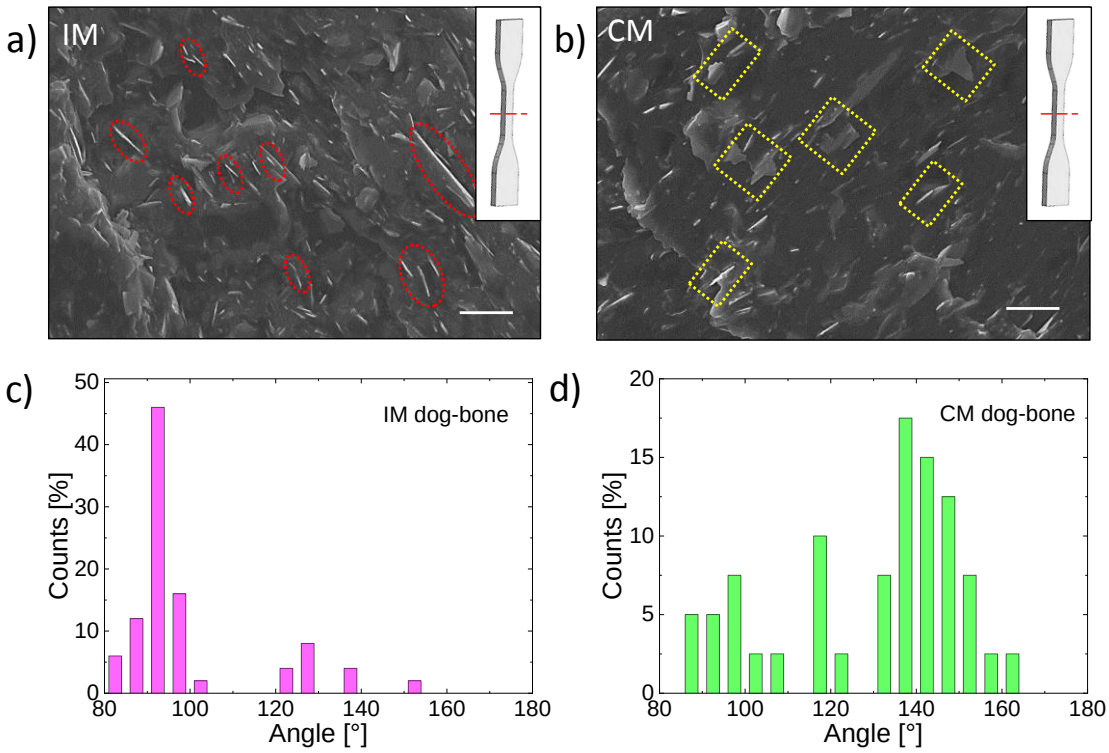

Figure 60 *- SEM images of the cross section of the samples of composite SB-15FLG$_{WJM}$: a) dog-bone sample IM, b) dog-bone sample CM, the analysed cross-section is indicated by the red line on the dog-bone in the inset, all scale bars correspond to 10 µm. c,d) Distribution of the angles of the flakes for the c) IM and d) CM sample.*

Regarding the disk shaped samples, the cross-section orthogonal to the direction used to measure the thermal conductivity is analysed. In both IM and CM samples, the FLG$_{WJM}$ are uniformly distributed in the matrix and there are not aggregates. (**Fig. 61a-b**) The flakes in the CM sample are protruding from the cross section and, even if the alignment is random, there is a preferential orientation along the direction used for measuring the thermal conductivity (red circles) (**Fig. 61a**). **Fig. 61b** shows that IM disk-shaped sample presents flakes, which are orthogonal to the testing

direction (yellow boxes). The values of the angles of the flakes of the IM samples present a distribution, which is in the 120 ° - 180 ° range (see **Fig. 61c**). On the contrary, most of the flakes in the CM sample possesses an angle around 90 °(**Fig. 61d**).

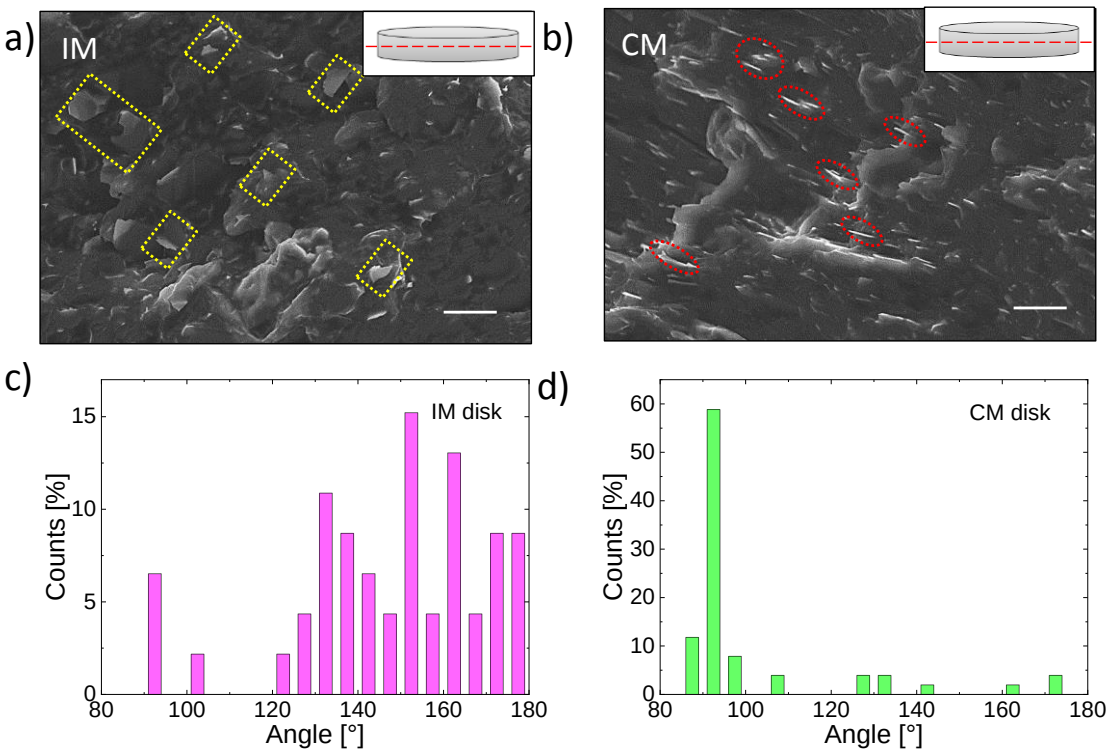

Figure 61 *- SEM images of the cross section of the samples of composite SB 15FLGWJM: a) disk shaped sample IM, b) disk shaped sample CM, the analysed cross-section is indicated by the red line on the dog bone in the inset, all scale bars correspond to 10 µm. c,d) Distribution of the angles of the flakes for the c) IM and d) CM sample.*

6.2.4 Thermal imaging

In order to demonstrate the suitability of the graphene-SB composite for the application of heat sink material in electronic packaging, the heat transfer of the composite containing 15 wt % of FLG_{WJM} is studied. The sample used to perform the thermal imaging is obtained by hot-pressing the CM disk shaped sample, because it has the highest thermal conductivity among the tested samples. **Fig. 62a** shows the average temperature of the pristine SB and the composite SB-15FLG_{WJM} measured during the heating of the samples at 50 °C in two minutes. As it is possible to observe in **Fig. 62b-c**, after two minutes the samples are heated up at 50 °C, the pristine material reaches ~36 °C, while the average temperature of the SB-15FLG_{WJM} composite is around 46 °C. These results suggest that the composite SB-15FLG_{WJM} can transfer better the heat compared to the pristine SB.

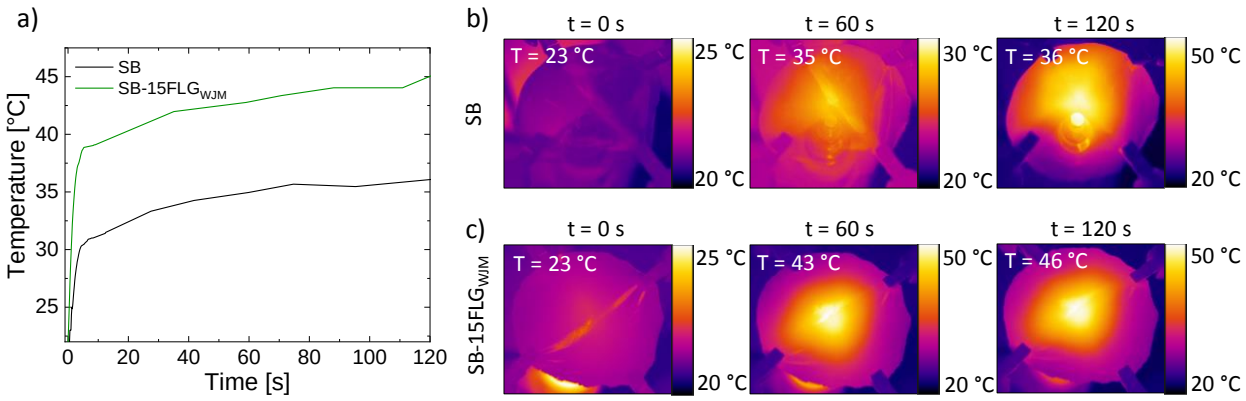

***Figure 62** - a) Average temperature in function of time of the samples SB and SB-15FLG_{WJM}, thermal images of b) SB, and c) SB-15FLG_{WJM}.*

6.3 Conclusions

This study has been focused on the production of graphene by means of wet jet milling and on the preparation of the graphene-styrene butadiene copolymer composite through a large-scale technique, *i.e.*, extrusion. The samples are manufactured using two different methods, compression and injection moulding. The effect of the manufacturing methods on the mechanical and thermal properties is studied. The injection moulded (IM) samples present better mechanical properties compared to the compression moulded (CM) ones, as the flakes are oriented in the testing direction in the IM dog-bones. Specifically, an enhancement of 60 % and 30 % is achieved, for the Young's modulus and the tensile strength, respectively, compared to the unloaded polymer by using 15 wt % of few layer graphene flakes. On the contrary, the CM samples show a higher thermal conductivity than the IM samples, obtaining an increase of 170 % compared to the matrix. This result is due to the orientation of the graphene flakes, as it is orthogonal to the testing direction in the IM samples, reducing the efficiency of the few layer graphene flakes in transferring the heat. Moreover, the thermal imaging shows that the heat transfer of the composite containing 15 wt % of loading is improved compared to the pristine polymer. In fact, after two minutes of heating both samples at 50 °C, the composite has reached ~ 46 °C, while the temperature of the unloaded polymer is around 36 °C.

Chapter 7: Conclusions and perspectives

The development of high-performance polymer composites is performed using graphene as nanofiller, due to the combination of its outstanding properties. However, technical issues need to be solved to achieve an enhancement of the desired properties in the polymer matrix. The aggregation of the graphene is deleterious for many properties of the composite, as mechanical, thermal, etc.. On the contrary, a poor interaction between the matrix and the graphene flakes leads to the embrittlement of the material and it damages the efficiency of graphene in improving the properties of the matrix. Moreover, the morphological features need to be tuned to tailor the final properties of the composites for each specific application.

Liquid phase exfoliation is a versatile approach to produce graphene flakes, allowing to introduce additional components, as poly methyl methacrylate (PMMA), in the processing. These components aid both the exfoliation of graphite and the distribution of graphene in different polymer matrices, *e.g.*, acrylonitrile-butadiene-styrene and polyamide 6, during the production of the graphene-polymer composites afterwards. Furthermore, it is possible to produce graphene with tailored morphological features by using the liquid phase exfoliation coupled with the sedimentation based separation.

In the following, a brief summary of the most relevant results achieved in my Thesis work is presented.

Polymethyl methacrylate assisted exfoliation of graphite and its use in acrylonitrile butadiene styrene composites

I have demonstrated that small amounts of PMMA (1 wt %) used as stabilizers for the exfoliation of graphite in acetone, allows to achieve a higher percentage of few-layer graphene flakes in the dispersion, obtaining a higher concentration of exfoliated flakes (*i.e.,* reaching 220 mg L^{-1}), compared to the exfoliation carried out in the bare acetone. In specific, the re-stacking of the

exfoliated flakes is hindered by the steric repulsion provided by the polymeric chains and the sedimentation of the flakes is slow down due to the increased viscosity. These phenomena lead to an increase in the concentration of the exfoliated graphite dispersions compared to the dispersions in bare acetone, *e.g.,* from 80 mg L^{-1} to 220 mg L^{-1} for a centrifugal acceleration of 200 *g.* Moreover, the dispersions produced in acetone-PMMA contain a higher quantity of few-layer graphene flake compared to the bare acetone dispersions*, e.g.,* from 36 % to 58 % for a centrifugal acceleration of 200 g. The Raman spectroscopy results show that PMMA has no doping effect on the flakes, while the TEM highlights that it does not affect the lateral size. The ABS composites prepared with the exfoliated graphite dispersions in acetone and acetone-PMMA present improvements in both the mechanical and gas barrier properties. A filler loading of 0.01 wt % is sufficient to obtain an enhancement in both the Young's modulus (~ 22 %) and tensile strength (~ 17 %) compared to the unloaded polymer. On the contrary, the composites containing 0.1 wt % of exfoliated flakes present a drop of ~ 20% in the oxygen permeability compared to the matrix. The ABS composites prepared with the few-layer graphene dispersions in acetone-PMMA can be used in the fabrication of membranes for the oxygen barrier to be exploited in food and electronic packaging.

Dependence of the graphene flakes morphology for the mechanical reinforcement in acrylonitrile-butadiene-styrene composites

The morphological properties of the graphene flakes are tuned by using sedimentation-based separation and cascade centrifugations. The as-produced graphene dispersions contain flakes, which possess areas in the range 0.01-0.8 μm^2 and thicknesses in the range of 0.9-4.2 nm. The mechanical properties of the graphene-ABS composites prepared with the as-produced dispersions are evaluated, in order to investigate the relationship between the reinforcement and the morphological features of graphene. The results highlight that there is a linear correlation between

the enhancements in Young's Modulus of composites and the parameter A/t^2. Moreover, it has been shown the existence of a high-stiffness regime at a loading below 0.1 wt %.

Wet jet milling graphene and its use in 3D printed polyamide 6-graphene composites for the enhancement of mechanical, tribological and thermal properties

A novel process for the production of graphene flakes is exploited: the wet jet milling (WJM). The graphene dispersion produced by WJM have a concentration of 3 g L^{-1}, containing few layer graphene (FLG) flakes with an average lateral size of 1200 nm. The as-produced graphene dispersion is used in the production of graphene-polyamide 6 composites through extrusion, using PMMA as additive, while the manufacturing of testing samples is carried out by means of 3D printing. The effect of PMMA on the distribution of the FLG flakes in the matrix is investigated by analyzing the mechanical, tribological and thermal properties of the composites.

The composites containing PMMA and FLG show a better mechanical and tribological performance compared to the composites prepared with FLG only, due to the fact that PMMA promotes a homogeneous distribution of the flakes. The best results in the mechanical properties are achieved in the composites containing PMMA and 3 wt % of filler, reaching an enhancement in the Young's modulus and the tensile strength of 160 % and 100 %, respectively, compared to the pristine polymer. Regarding the tribological properties, in the composite with PMMA and 1 wt % of filler, the steady state coefficient of friction has an increase of 30 % and the wear rate decreases of 50 % compared to the unloaded polymer. Both the graphene-polyamide 6 composites, with and without PMMA, show an improved thermal transfer, indicating that PMMA does not affect this property. The improvements in the mechanical, tribological and thermal properties observed in the graphene-polyamide 6 composites point out that these materials are suitable for applications requiring friction and resistance to wear, *e.g.* hose clamps and fasteners.

Wet jet milling graphene - elastomer composites: effect of processing on the mechanical and thermal properties

The FLG flakes produced through wet jet milling was also used for the preparation of styrene-butadiene (SB) composites, by extrusion. The extruded samples were manufactured by using compression and injection moulding to study the effect of the different manufacturing methods on the composite properties. The results indicate that the samples prepared by injection moulding, present better mechanical properties than the compression moulded ones. The Young's modulus and the tensile strength present an enhancement of 60 % and 47 %, respectively, compared to the unloaded polymer by using 15 wt % of graphene flakes. Instead, the compression moulded samples possess better thermal properties compared to the injection moulded ones. The thermal conductivity has an increase of 170 % with respect to the pristine polymer. We demonstrate that the reported performance improvements are due to preferential flakes orientation in the samples. In fact, injection moulded samples used for the tensile testing possess graphene flakes, which are oriented along the direction of the applied tensile load. The flakes contained in the disk-shaped samples present flakes, which are oriented in the direction considered in the thermal conductivity measurement. The heat transfer of the pristine styrene butadiene copolymer and of the composite containing 15 wt % of loading, prepared through compression moulding followed by hot-pressing, is studied. Thermal imaging is performed by exposing both the materials at a heat source at 50 °C for 2 minutes. The results show that the heat transfer is better in the composite compared to the pristine polymer. In fact, during the testing, the pristine polymer reaches a temperature of ~ 36 °C, while the temperature of the composite is around 46 °C. The produced graphene-SB composites can be used as heat sink materials for the electronic packaging, due to the improved mechanical and thermal properties.

Future perspectives

In the graphene-polymer composites field, there are still many challenges to face ahead. The exploitation of copolymer, i.e., Poly methyl methacrylate (PMMA), could improve the distribution of graphene flakes as filler in other polymer matrices, enhancing other properties, such as thermal/chemical stability and flame retardancy.

Furthermore, other two-dimensional crystals, such as boron nitride and molybdenum disulfide, can be produced in low boiling point solvents using PMMA or other polymers as stabilizers.

The final properties of the graphene-polymer composites can be tailored using other manufacturing techniques, as 3D printing, on the basis on the effect of the orientation of the flakes. For example, creating preferential thermal paths for the management of the heat on complex electronic structures and devices.

Thesis summary

1. Introduction

Graphene is a two-dimensional material, composed by sp^2 hybridized carbon atoms in a hexagonal lattice (*37*) This material has attracted great interest in the scientific community due to its outstanding properties, *e.g.,* Young's modulus ~ 1 TPa (*10*), thermal conductivity of 5300-6000 W mK^{-1} (*9*), among others.

The production of graphene is performed through various methods (*73*), *e.g.,* chemical vapour deposition (*88*), growth on silicon carbide. (*76*), etc. Among the production techniques, liquid-phase exfoliation (LPE) of graphite stands out due to scalability and versatility. (*73*) The process starts with the dispersion of graphite into a solvent with a surface tension around 40-50 mN m^{-1} to minimize the interfacial tension between the graphite and the solvent itself. (*118*) However, most of the solvents used for exfoliation of graphite, as well as of other layered materials, have a high boiling point and are toxic, making them unsuitable for the further processing of the graphene dispersions. (*143*, *144*) The surface tension of low boiling point solvents is not ideal (*142*), so the aid of stabilizers is needed, *e.g.,* surfactants (*122*) or polymers (*128*). Then, the exfoliation is done by means of ultrasonication or high-pressure homogenizers, where graphite is exfoliated by cavitation or shear forces, respectively. (*118*, *133*, *320*) Ultrasonication is more oriented towards laboratory-scale production, while, among the high-pressure homogenizers, wet jet milling is potentially promising as an industrially scalable method. (*320*) Finally the obtained dispersion is "purified" from the un-exfoliated and the thickest flakes through sedimentation based separation (SBS). (*184*) Graphene can potentially be exploited in various applications, as electronics (*42*), energy storage (*45*) and in polymer composites (*44*), in which it is generally used as filler to improve the properties of the matrix. In fact, composites with improved mechanical properties are used in the aerospace field (*197*) and in sporting goods (*195*), while composites with an enhanced thermal transport can be found in wearables, e.g. helmets and shoes. (*200*, *202*) The composites can be also potentially used into the food packaging due to their gas barrier properties (*205*), and as components in the automotive, *e.g.,* transmission gears, for their tribological properties (*210*).

The production of graphene-composites can be performed by mainly three routes: in-situ polymerization, solution blending and melt blending. (*44*) In-situ polymerization is performed by mixing the graphene flakes with a monomer solution, forming the composite by initiating the polymerization through heat or radiation. (*44*) Solution blending occurs by mixing the polymeric solution with graphene, followed by the solvent evaporation. (*44*) These two techniques require the use of a solvent allowing to obtain an optimal distribution of graphene flakes into the matrix. (*44*) On the contrary, melt blending consists of mixing the graphene flakes with the matrix in the molten state by applying shear forces using instruments as extruders. (*44*) It is more compatible with the industrial manufacturing techniques compared to the others, *e.g.,* injection moulding, and no solvent is involved. (*44*)

After the production of graphene-polymer composites, the final composites are manufactured in the desired shape through mainly three processes: compression moulding (*254*), injection moulding (*246*) and fused deposition modelling (FDM) (*259*). Compression moulding consists in applying pressure and heat simultaneously on the composite pellets in a mould, in this case, the graphene flakes are randomly oriented in the matrix. (*254*) In injection moulding, the composites pellets are first melted, then injected into a mould, the graphene flakes are oriented in the direction of the flow. (*246*) Fused deposition modelling belongs to the class of the 3D printing techniques and it is compatible with thermoplastics. (*259*) During the FDM process, the sample is built layer by layer through the extrusion of "roads" on a plate, which lowers in the zeta direction. (*259*) In FDM, the graphene flakes tend to align along the printing direction in the matrix. (*259*) The orientation of the filler in the matrix has to be considered when choosing the manufacturing method, as it affects the properties of the graphene-polymer composites.

The mechanical, thermal, gas barrier and tribological properties are influenced by factors regarding the aspect ratio, the distribution and the orientation of the graphene flakes in the matrix, as well as the interface between the filler and the polymer. (*44*)

The improvement of the mechanical properties is based on the transfer of the stress from the polymer matrix to the filler.(*270*) It is necessary to use graphene flakes with an aspect ratio as high as possible so that there is a large area available for the stress transfer. (*240*) If the filler is aligned along the direction of the stress, then the stress transfer is more effective than the case of randomly oriented filler. (*257*) Moreover, aggregation decreases the area of the filler, diminishing the reinforcing effect on the matrix with respect to well-distributed graphene flakes. (*255*) In addition, a strong interface between the filler and matrix, *e.g.,* covalent bonding, promotes the transfer of the stress. (*274*) The thermal properties of the graphene-polymer composites depend on the heat transfer in the polymer matrix. (*281*) The heat transfer is promoted when the distance between the graphene flakes is as small as possible, so a high aspect ratio is preferable. (*283*) The orientation of the filler is affecting the direction and the efficiency of the thermal propagation. (*257*) Furthermore, a good distribution of the graphene flakes allows forming a thermal path between the flakes, promoting the heat transfer. (*287*) A weak interface among the filler and the matrix causes the scattering of the phonons, hindering the heat passage. (*288*) The gas barrier properties of the graphene-polymer composites are enhanced, as graphene makes the molecules of gas follow a longer and more tortuous pathway to cross the matrix. (*289*) Graphene flakes possessing a high aspect ratio make a longer gas path length with respect to the flakes with low aspect ratio. (*290*) Moreover, the filler has to be oriented orthogonally to the gas flow, in order to maximize the gas barrier effect. (*271*) The distribution of the flakes is fundamental to assure the formation of a “labyrinth-like” structure in the matrix and slow down the passage of the gases. (*294*) The lubricant property of graphene improves the tribological properties of the graphene-polymer composites, decreasing the wear.(*232*, *298*) The graphene flakes form a protective layer on the rubbing part and on the tested material, avoiding the damage of the composites. (*232*, *298*) In this context, the distribution of the flakes plays a crucial role, as the aggregates, once they are pulled out from the surface, act as a third body worsening the wear and hindering the formation of the protective layer. (*232*, *298*)

The scheme presented in **Fig. 1** presents the production of graphene-based flakes, their integration into polymer composites and the possible applications following the obtained properties.

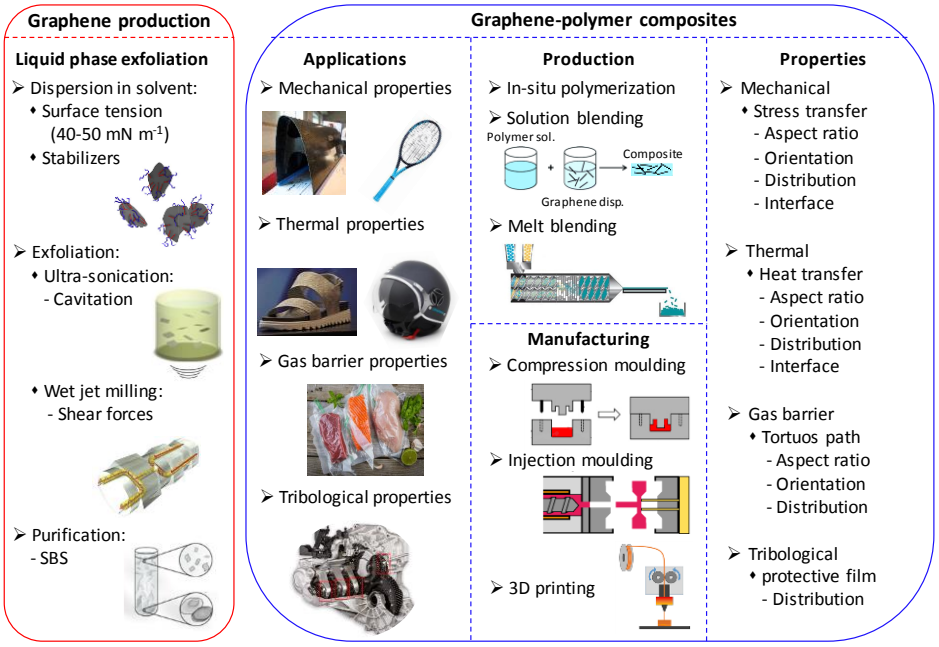

Figure 1 *– Scheme of the production of graphene-based flakes, the integration into polymer composites, their properties and the feasible applications.*

2. Polymethyl methacrylate assisted exfoliation of graphite and its use in acrylonitrile butadiene styrene composites

In this study, the goal was to address the issues related to the use of toxic and high boiling point solvents in LPE for the production of graphene flakes. On this regard, polymethyl methacrylate (PMMA) is exploited as a stabilizing polymer for the exfoliation of graphite in acetone. (*346*, *347*, *357*) In order to study the effect of PMMA on the exfoliation, dispersions of exfoliated graphite are produced using ultrasonication based LPE by using acetone and acetone-PMMA as solvents. The dispersions produced in acetone are defined as "FLG_{US}" and the dispersions produced in the mixture acetone-PMMA are called "FLG-$PMMA_{US}$". Moreover, the effect of PMMA is studied also in the SBS step by using three different centrifugal accelerations, *i.e.,* 200 *g*, 4300 *g* and 17000 *g*. The influence of PMMA on the main features of the exfoliated graphite dispersions is considered, *e.g*., lateral size, thickness, etc. Furthermore, the obtained dispersions centrifuged at 200 *g* are used to prepare acrylonitrile butadiene styrene (ABS) composites by solution blending and hot pressing. In detail, the effect of the graphene flakes produced in acetone and PMMA on the mechanical and gas barrier properties of the composites is analysed. PMMA is supposed to improve the aforementioned properties by promoting the optimal distribution of the flakes into the polymeric matrix, due to its miscibility with ABS. (*351–356*)

2.1 Characterization of the exfoliated graphite dispersions

The main results of the Raman spectroscopy analysis indicate that the PMMA does not have doping effect on the flakes and that the dispersions "FLG-$PMMA_{US}$" contain a higher percentage of few-layer graphene flakes than the dispersions "FLG_{US}". (Table 1) This result is confirmed by the measurement of the graphene flakes performed by atomic force microscopy (AFM). The percentage of the FLG in the dispersions increases with the centrifugal acceleration. (Table 1) Moreover, PMMA seems to have no effect on the lateral size of the flakes, evaluated by transmission electron microscopy (TEM), see Table 1. The lateral size of the as-produced flakes decreases, as the centrifugal acceleration raises. The concentration of both the dispersions is measured by vacuum filtration. In addition, optical absorption spectroscopy (OAS) and thermogravimetric analysis (TGA) are used to analyse the concentration only for the FLG-$PMMA_{US}$ centrifuged at 200 *g*, in order to exclude any side effects of PMMA and confirm the concentration measurements performed through vacuum filtration. The concentration of the "FLG-$PMMA_{US}$" dispersions is higher compared to the "FLG_{US}" dispersions, for all the three centrifugal accelerations. (Table 1)

Table 1 *- Percentage of FLG flakes and lateral size of the flakes; concentration of the dispersions FLG_{US} and FLG-$PMMA_{US}$ with the corresponding standard deviations in parenthesis.*

	FLG_{US}	FLG-$PMMA_{US}$	FLG_{US}	FLG-$PMMA_{US}$	FLG_{US}	FLG-$PMMA_{US}$
	@ 200 *g*		@ 4300 *g*		@ 17000 *g*	
FLG [%]	36	58	53	70	93	98
Lateral size [nm]	520 (0.57)	600 (0.40)	400 (0.50)	370 (0.43)	300 (0.60)	270 (0.33)
C [mg L^{-1}]	80 (20)	220 (40)	30 (10)	90 (0.20)	1 (0.2)	30 (6)

In order to explain the effect of PMMA on the LPE process, the density (ρ), the viscosity (η) and the surface tension (γ) of acetone and the acetone-PMMA mixture are analyzed. (Table 2) The results show that there is no difference in ρ and γ when PMMA is added to acetone, while η is doubled.

Table 2 *– The ρ, η and γ of acetone and the mixture acetone-PMMA, with the corresponding standard deviations in parenthesis*

	ρ [g cm^{-3}]	η [mPa s]	γ [mN m^{-1}]
Acetone	0.80 (0.02)	0.295 (0.001)	23.8 (0.4)
Acetone-PMMA	0.77 (0.03)	0.559 (0.001)	23.3 (0.2)

The sedimentation coefficient is inversely proportional to the η so that an increase in the η of acetone corresponds to a decrease of the sedimentation rate of the flakes. (*184*) Therefore, a higher amount of flakes remains in the supernatant in the FLG-PMMA$_{US}$ dispersion compared to the FLG$_{US}$ dispersions, after the centrifugation. Moreover, the number of exfoliated flakes with a thickness lower than 4 nm is increasing, while the concentration of the flakes in the dispersions decreases, when the centrifugal acceleration is raised. When the centrifugal acceleration is increased, a higher centrifugal force is applied to the flakes. (*184*) The thicker flakes contained in the dispersions are the first to precipitate, as they sediment faster compared to the thinner flakes. (*184*) Hence, the population of thick flakes, and so the concentration of the overall flakes, in the supernatant decreases as the centrifugal acceleration varies from 200 *g* to 17000 *g*.

2.2 Characterization of polymer composites prepared with the exfoliated graphite dispersions

The mechanical properties of the polymer blends for the production of membranes for gas separation (*362–364*), *e.g.,* CO_2 (*364*), are improved by using ABS as a reinforcing polymer. In order to enhance the performance of ABS in the aforementioned blends, it is necessary to enhance both the mechanical and gas barrier properties through the addition of exfoliated graphite flakes into ABS (*44*). The FLG$_{US}$ and FLG-PMMA$_{US}$ dispersions centrifuged at 200 *g* are used to prepare the ABS composites, as their concentration is the highest among the prepared dispersions, *i.e.,* 220 ± 40 mg L^{-1} and 80 ± 20 mg L^{-1} for the dispersions FLG-PMMA$_{US}$ and FLG$_{US}$, respectively. The presence of PMMA is supposed to promote the distribution of the flakes in the ABS. In fact, PMMA is able to form miscible blends with ABS or its component styrene acrylonitrile. (*351–356*)

The mechanical properties, *i.e.,* the Young's modulus (YM) and the tensile strength (TS), are evaluated by tensile testing. In this study, the Young's modulus and the tensile strength improve of ~ 22 % and ~ 17 %, respectively, compared to the pristine ABS, by using a loading of 0.01 wt% FLG. The presence of PMMA in the ABS-FLG-PMMA$_{US}$ composites facilitates a homogeneous distribution of the FLG flakes, in fact the tensile strength remains constant as the loading of filler is increased. (**Fig. 2a**) On the opposite, there is no enhancement of the tensile strength in the ABS-FLG$_{US}$ composites compared to the unfilled polymer, when the loading is increased, due to the inhomogeneous distribution (**Fig. 2a**). (*367*, *368*) In literature, graphene nanoplatelets are exploited in the polymer composites to hinder the gas permeation.(*289*, *292*, *369*, *370*, *408*, *409*) In fact, the incorporation of the filler forms a network, which is a hindrance to the diffusion of gases through the polymer matrix.(*289*, *370*) In this study, the oxygen permeability (OP) of the composites ABS-FLG$_{US}$ and ABS-FLG-PMMA$_{US}$ with 0.1 wt % of filler is dropped of ~ 13 % and ~ 20 %, respectively, compared to the pristine ABS (**Fig. 2b**). In the composites ABS-FLG-PMMA$_{US}$, the OP is ~ 7 % lower than in the ABS-FLG$_{US}$ composites, as both PMMA and the few-layer graphene flakes may hinder the oxygen passage.

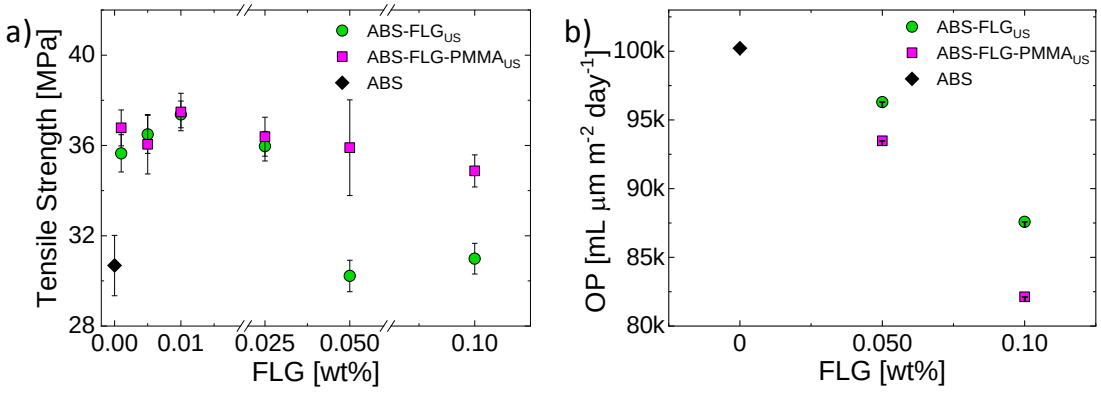

***Figure 2** – a) Tensile strength and b) oxygen permeability of the composites ABS-FLG$_{US}$ and ABS-FLG-PMMA$_{US}$ compared with the pristine ABS.*

3. Dependence of the graphene flakes morphology for the mechanical reinforcement in acrylonitrile butadiene styrene composites

Ultrasonication-based LPE followed by cascade centrifugation steps is used to produce dispersions of exfoliated graphite flakes having different morphology, *i.e.,* surface area (*A*) and thickness (*t*). A and t of the flakes are measured performing TEM and AFM analysis, respectively. Subsequently, ABS composites are prepared, exploiting the flakes having different morphologies, as the main goal of this work is to analyze the enhancement of the Young's modulus of the ABS matrix, as a function of the filler content and flakes morphology. In this regard, a linear relation between the mechanical reinforcement and A/t^2 ratio is demonstrated. Moreover, a regime of "high-stiffness" is found at a loading below 0.1 wt %, in which the experimental value of the Young's modulus of the flakes, *i.e.,* 1.28 TPa, is higher than the theoretical one, *i.e.,* 1 TPa (*10*). Five different dispersions are prepared, using a centrifugal acceleration of 170 g (sample FLG-1), 1000 g (sample FLG-2), 4250 g (sample FLG-3), 9500 g (sample FLG-4) and 17000 g (sample FLG-5). The AFM and TEM analysis show that the area and the thickness of the flakes decreases when the centrifugal acceleration is increased. Moreover, the dispersions FLG-6, FLG-7, FLG-8 are prepared through cascade centrifugation steps of 170-4250-170 g, 170-4250-170-170 g, and 170-4250-170-170-170 g, respectively. (*303*) The areas, the thicknesses and the ratio of the area over the squared thickness of the prepared dispersions are reported in table 3.

Table 3 *- The A, t, and A/t^2 morphological properties of the flakes contained in the prepared dispersions.*

sample	*A*	*t*	A/t^2
	[μm^2]	[nm]	
FLG-1	0.078	4.2	4421.8
FLG-2	0.059	3.8	4085.9
FLG-3	0.052	2.2	10743.8
FLG-4	0.013	2.1	2947.8
FLG-5	0.008	0.9	9876.5
FLG-6	0.046	1.0	46000.0
FLG-7	0.051	1.2	35416.7
FLG-8	0.048	1.5	21333.3

The Young's modulus (YM) of both bare ABS and FLG-ABS composites is measured by performing mechanical tests. The YM of the ABS composites containing the FLG flakes prepared with different centrifugal accelerations (samples FLG-1 to FLG-5) and with the cascade centrifugation (samples FLG-6 to FLG-8) is presented in Fig. 3a and Fig. 3b, respectively. The YM tends to increase with the loading of LFG and the maximum improvement, *i.e.,* ~ 24 %, in the Young's modulus compared to the pristine matrix is reached using 0.1 wt % of FLG-6 flakes.

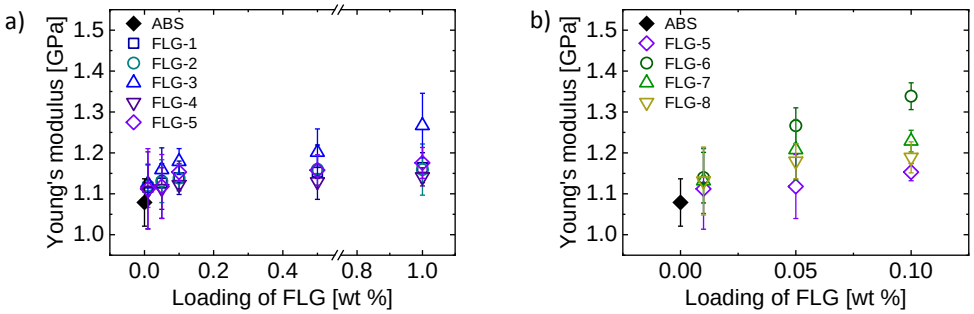

Figure 3*5 - Young's modulus of the FLG-ABS composites prepared with a) FLG-1 to FLG-5 and with b) FLG-5 to FLG-8 compared with the pristine ABS.*

Then, an investigation on the relationship between the YM of the composites and the morphological parameters, as *l/t*, *√A/t*, *A/t* and *A/t²,* is carried out. The linear relation between the YM and the morphological parameters is analyzed considering the Pearson's coefficient (P_r) as discriminating factor, between a linear and a non-linear correlation (*371*). The parameter A/t^2 is found to have a linear correlation with the YM, having a P_r is equal 0.95 for the composites containing a loading of 0.1 wt % (Fig. 4a). Finally, the YM of the FLG flakes is back-calculated using the "rule of mixture" for ABS composites containing different loadings of FLG flakes, having different A/t^2 values. The results show that for low loadings, *i.e.,* 0.01 wt %, the back-calculated YM of the FLG flakes, *i.e.,* ~ 1.28 TPa, is higher than the theoretical values, *e.g.,* ~ 1.0 TPa, revealing the existence of a regime of "high-stiffness" (Fig. 4b).

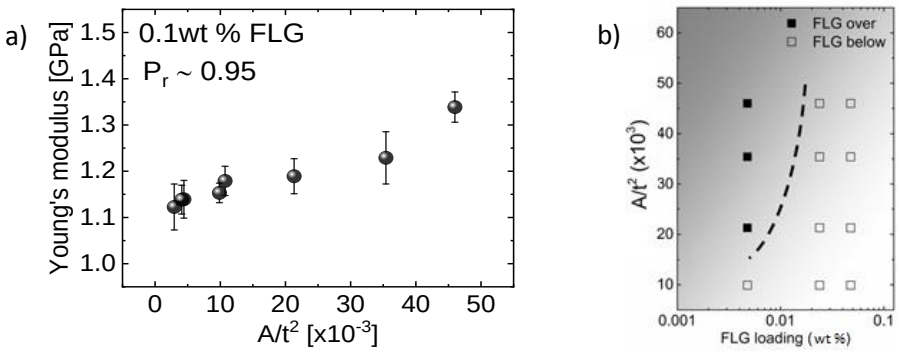

Figure 4*6 –a) Young's Modulus of the composites containing 0.1 wt % of FLG as function of the morphological property A/t^2, b) the back-calculated Young's moduli (YM_f) of the FLG flakes as a function of loading and A/t^2 ratio, filled symbols indicate flakes with a YM_f over the theoretical value.*

4. Wet jet milling graphene and its use in 3D printed polyamide 6-graphene composites for the enhancement of mechanical, tribological and thermal properties

Polyamide 6 (PA) is a thermoplastic polymer, whose mechanical, tribological and thermal properties are exploited in applications as gears (*209*), bearings (*209*), slide blocks (*209*) and structural components in the automotive industry (*376*). This study is focused on the improvement of these properties by the addition of graphene flakes to the polymer matrix. The third component as polymethyl methacrylate (PMMA) is used to promote the distribution of the graphene flakes in the PA matrix, assuring the improvement of the desired properties. In fact, the carbonyl group of PMMA interacts with both the filler and the matrix, forming a hydrogen bond. (*345–347*, *357*) In detail, the production of the graphene flakes is performed by wet jet milling, followed by the lyophilisation of the dispersion to obtain a powder (FLG_{WJM}). The powder is redispersed in acetone and in a mixture of acetone-PMMA. The achieved dispersions are used to impregnate pristine pellets of PA, which are then extruded in wires. The extruded composites are used in 3D printing to manufacture the samples for the characterization. The produced composites are PA-FLG_{WJM} and PA-PMMA-FLG_{WJM}, using a load of 1 wt % and 3 wt % in both the kind of composites. Control samples PA-PMMA not containing FLG_{WJM} are also prepared with 1 wt % and 3 wt % of PMMA.

The dispersions of graphene flakes obtained through wet jet milling are characterized by Raman spectroscopy, revealing that 70 % of the exfoliated graphite flakes are FLG ones. This result is confirmed by AFM, measuring the average thickness of the flakes around 3.2 nm, while the average lateral size of the flakes is at ~ 1200 nm, according to the TEM measurements. The concentration of the graphene dispersions equals to 3 g L^{-1} and it is evaluated through OAS. The cross-section of the composites PA-FLG_{WJM} and PA-PMMA-FLG_{WJM} is analysed by scanning electron microscopy (SEM) and Raman mapping. Both the analysis shows that the distribution of the FLG flakes in the composites PA-PMMA-FLG_{WJM} than in the composites PA-FLG_{WJM}.

Tensile testing is performed on the composites, considering the Young's modulus and the tensile strength. Enhancement of 130 % and 160 % is achieved for the composites PA-3FLG$_{WJM}$ and PA-PMMA-3FLG$_{WJM}$, respectively, compared to the pristine polymer. While, the tensile strength has an improvement of 60 % and 100 % for the composites, PA-FLG$_{WJM}$ and PA-PMMA-FLG$_{WJM}$, respectively. (**Fig. 5a**) In literature (*385*, *393*, *394*), FLG-PA composites, which are affected by aggregation of the filler, present a lower value in the tensile strength compared to composites having well-distributed graphene flakes. Therefore, the distribution of graphene flakes into the PA matrix is improved due to the PMMA presence, as the tensile strength is constant for the composites PA-PMMA-FLG$_{WJM}$. The required tribological properties depend on the final use of the material, for example, friction as low as possible is necessary for applications as gears and bearings, while the opposite is needed for other applications, *e.g.* hose clamps and fasteners. (*376*) Instead, the wear rate (K) indicates the wear of the surface of the samples when a constant load is applied during the cyclic sliding of a steel ball. The steady coefficient of friction (μ) is measured for both the composites PA-FLG$_{WJM}$ and PA-PMMA-FLG$_{WJM}$. The μ has an increment of 20 % and 90 % in the composites PA-FLG$_{WJM}$ and PA-PMMA-FLG$_{WJM}$, respectively, compared to PA (**Fig. 5b**). In literature (*297*, *298*, *385*), the graphene flakes, due to their lubricant action, are used to decrease the μ of the FLG-PA composites. Further studies need to be performed to explain why the μ is increasing in our composites.

The K of the composite PA-PMMA-1FLG$_{WJM}$ decreases by 50 % compared to PA (**Fig. 5c**). This phenomenon may be due to the formation of a protective film of graphene flakes both on the steel ball and on the surface of the sample, reducing the friction. (*299*, *302*, *396*) Morphological analysis carried out by SEM reveals that the sliding path of the composite is smooth and there is no debris, there are FLG flakes on the surface of the sample. However, there is a drastic increase in the K of PA-3FLG$_{WJM}$ of 230 % compared to PA. (**Fig. 5c**) Instead, the K of PA-PMMA-3FLG$_{WJM}$ has an increment of 108 % in comparison with PA, but it is 122 % lower than the composite not containing PMMA. (**Fig. 5c**) SEM analysis shows that the sliding paths of both the composites present debris on the edges and longitudinal cracks.

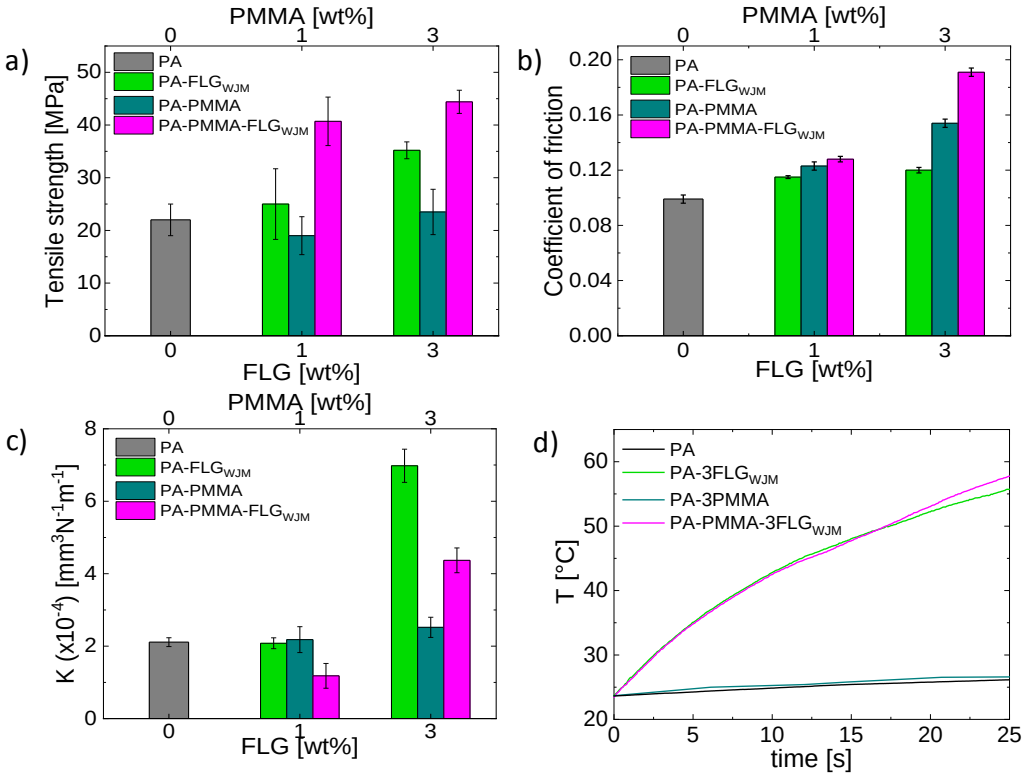

Figure 5 *- a) Tensile strength, b) coefficient of friction, c) wear rate, d) thermal imaging curves expressing the temperature in function of the time of the composites PA-FLG$_{WJM}$, PA-PMMA-FLG$_{WJM}$ and the samples PA-PMMA compared with the pristine PA*

This phenomenon may be due to the presence of FLG flakes aggregates, which detach from the sample surface during the testing and act as an abrasive body between the sample and the steel ball, hindering the formation of the protective films. (*298*) In order to improve the use of PA as material for the aforementioned applications, besides mechanical and tribological properties, also thermal transfer is considered as an important property to enhance. (*397*) In fact, when extensive friction occurs, heat is generated, so it is preferable to choose a material that can dissipate the heat to assure the durability of the component. (*397*) During the analysis with the thermal camera the pristine PA and the sample PA-PMMA reach a temperature of 26°C after being heated at 60 °C for 20 s (**Fig. 5d**). Instead, in the composites PA-3FLG$_{WJM}$ and PA-PMMA-3FLG$_{WJM}$, the temperature increases to 52 °C after 20 s, indicating that there is an improvement in the thermal transfer, even in the composites where there is the PMMA (**Fig. 5d**). In fact, in the literature (*388*, *398–401*), graphene flakes are known to increase the thermal conductivity of the PA matrix.

5. Wet jet milling graphene - elastomer composites: effect of processing on the mechanical and thermal properties

The styrene-butadiene copolymer (SB) is a thermoplastic elastomer, which is usually utilized for applications related to shoe soling and sporting goods. (*402*) SB has similar properties to rubbers, but it does not need any vulcanization and it can be reprocessed, making it more versatile during the manufacturing step. (*403*) The graphene-SB composites are producing by mixing the graphene powder produced by wet jet milling and the powder of pristine SB. Then, the mixed powders are extruded by means of a twin-screw extruder and the obtained wires are pelletized. The samples are manufactured through two different methods, compression moulding and injection moulding, to study the effect of the techniques on the mechanical properties and the thermal conductivity of the composites. The graphene-SB composites are prepared using a loading ranging from 1 wt % to 15 wt %, so, for example, the composite SB-15FLG$_{WJM}$ contains 15 wt % of filler. The tensile testing is carried out on dog-bone shaped samples, while the thermal conductivity is measured on disk-shaped samples, across the two sides of the disks.

The Young's modulus and the tensile strength of both the samples produced with injection (IM) and compression (CM) moulding increase with the FLG$_{WJM}$ loading. This trend indicates that the flakes have a homogeneous distribution even at a relatively high percentage of filler, *i.e.,* 15 wt %, as aggregation causes the tensile strength to decrease. (*410*, *411*) The tensile strength has an improvement of 30 % with respect to the pristine polymer, using 15 wt % of FLG$_{WJM}$, for both IM and CM samples. The composite SB-15FLG$_{WJM}$ shows an enhancement in the Young's modulus of 40 % and 60 % for the CM and the IM samples, respectively, compared to the unloaded polymer (**Fig 6a**). This phenomenon may be due to the difference in the orientation of the filler in the matrix, caused by the different manufacturing technique, which affects the mechanical properties as explained in the introduction.

The thermal conductivity of the composites IM and CM raises with the increasing of the percentage of FLG$_{WJM}$, in agreement with literature. (*406*, *407*) The CM and IM samples reach an improvement of 170 % and 110 %, respectively, with 15 wt % of FLG compared to the SB polymer (**Fig. 6b**). The CM samples show a better performance with respect to the IM samples, probably owing to the different orientation of the flakes in the disk samples.

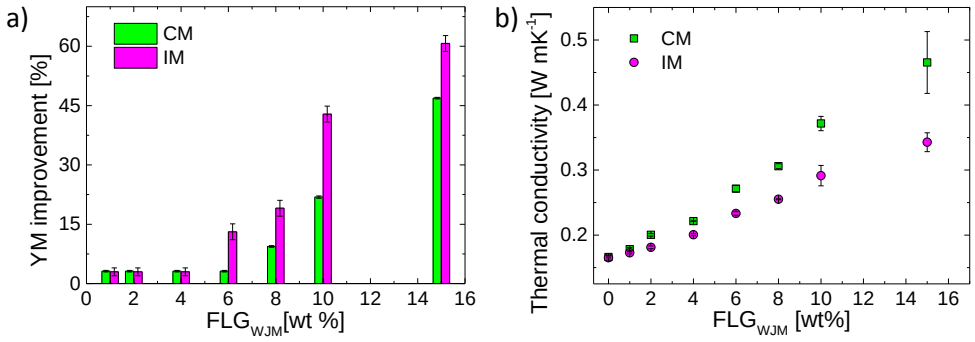

Figure 6 *- Comparison of a) the Young's modulus improvement and b) the thermal conductivity of the composites produced through compression moulding (CM) (green) and injection moulding (IM) (magenta)*

The morphological analysis is performed on the cross-section of the dog-bone samples and the disk-shaped samples, in order to explain the results obtained in the mechanical and thermal characterization. In the injection moulded dog-bone samples (IM), the FLG_{WJM} are oriented along the direction of the load applied during the mechanical testing. (**Fig. 7a**) In fact the FLG_{WJM} are aligned following the flow of the molted composite during the injection moulding process. Instead, the compression moulded dog-bone samples contain FLG_{WJM}, which are randomly aligned and FLG_{WJM} aligned. The SEM analysis of the dog-bone samples confirms the results obtained in the tensile testing. Instead, the SEM analysis on the disk-shaped samples reveals that in the injection moulded samples contain FLG_{WJM}, which are oriented orthogonally to the direction used to test the thermal conductivity. This orientation is induced by the flow of the molten composites into the mould during the injection moulding process. While, in the compression moulded disks (CM), the FLG_{WJM} are more oriented along the testing direction with respect to the injection moulded samples, facilitating the heat transfer. (**Fig. 7b**)

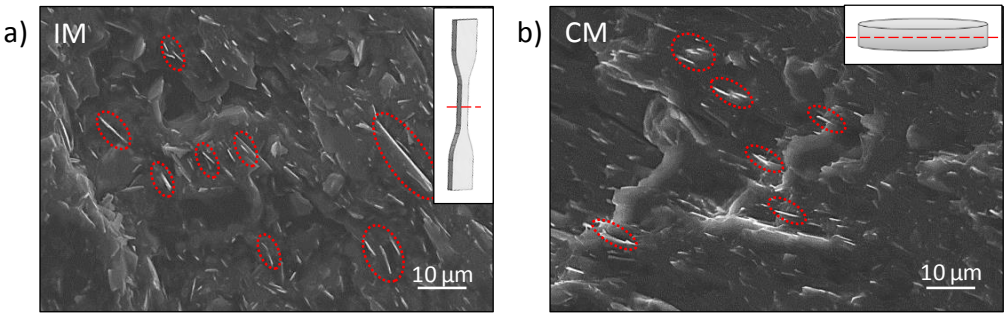

Figure 7 *- SEM images of the cross-section of the samples of composite SB-15FLG: a) dog-bone sample IM and b) disk sample CM, the analyzed cross-section is shown by the red line on the disk in the inset.*

The heat transfer of the composite containing 15 wt % of FLG_{WJM} is studied, in order to demonstrate the suitability of the graphene-SB composite for the application of heat sink material in electronic packaging. The sample used to perform the thermal imaging is prepared by hot-pressing the CM disk shaped sample, due to the fact that its thermal conductivity is the highest among the tested samples. **Fig. 8a** shows the average temperature of the pristine SB and the composite SB-$15FLG_{WJM}$ evaluated during the heating of the samples at 50 °C in two minutes. After two minutes the pristine material reaches ~ 36 °C, while the average temperature of the SB-$15FLG_{WJM}$ composite is around 46 °C. (**Fig. 8b-c**) These results suggest that the composite SB-$15FLG_{WJM}$ can transfer better the heat with respect to the pristine SB.

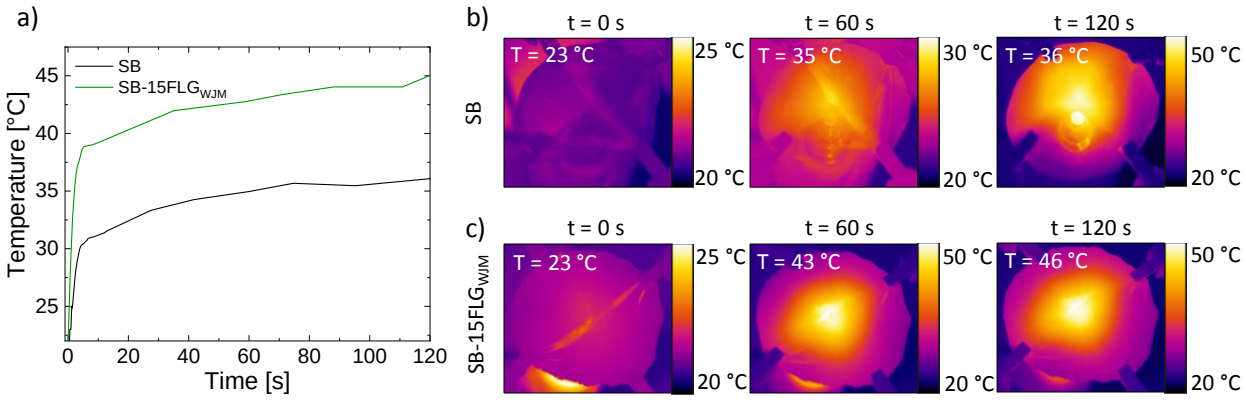

Figure 8 *- a) Average temperature in function of time of the samples SB and SB 15FLGWJM, thermal images of b) SB, and c) SB 15FLG$_{WJM}$.*

Bibliography

1. A. Hirsch, The era of carbon allotropes. *Nat. Mater.* **9**, 868–871 (2010).
2. S. Philip, T. Keshavarz, I. Roy, Carbon allotropes:beyond graphite and diamond. *J. Chem. Technol. Biotechnol.* **82**, 524–531 (2007).
3. S. Zhang *et al.*, Penta-graphene: A new carbon allotrope. *Proc. Natl. Acad. Sci. U. S. A.* **112**, 2372–2377 (2015).
4. N. Karousis, I. Suarez-Martinez, C. P. Ewels, N. Tagmatarchis, Structure, Properties, Functionalization, and Applications of Carbon Nanohorns. *Chem. Rev.* **116**, 4850–4883 (2016).
5. A. R. Oganov, R. J. Hemley, R. M. Hazen, A. P. Jones, Structure, bonding, and mineralogy of carbon at extreme conditions. *Rev. Mineral. Geochemistry*. **75**, 47–77 (2013).
6. V. Georgakilas, J. A. Perman, J. Tucek, R. Zboril, Broad Family of Carbon Nanoallotropes: Classification, Chemistry, and Applications of Fullerenes, Carbon Dots, Nanotubes, Graphene, Nanodiamonds, and Combined Superstructures. *Chem. Rev.* **115**, 4744–4822 (2015).
7. M. D. Stoller, S. Park, Y. Zhu, J. An, R. S. Ruoff, Graphene-Based Ultracapacitors. *Nano Lett.* **8**, 3498–3502 (2008).
8. A. K. Geim, K. S. Novoselov, The rise of graphene. *Nat. Mater.* **6**, 183–191 (2007).
9. A. A. Balandin, S. Ghosh, W. Bao, I. Calizo, Superior Thermal Conductivity of single layer graphene. *Nano*. **8**, 902–907 (2008).
10. C. Lee, X. Wei, J. W. Kysar, J. Hone, Measurement of the Elastic properties and intrinsic strength of Monolayer Graphene. *Science*. **321**, 385–388 (2008).
11. Y. Gogotsi, *Nanomaterials Handbook* (CRC Press, 2006).
12. I. Baker, *Fifty Materials That Make the World* (Springer, 2018).
13. S. Kasap, P. Capper, *Springer Handbook of Electronic and Photonic Materials* (2017).
14. A. Banerjee *et al.*, Ultralarge elastic deformation of nanoscale diamond. *Science*. **360**, 300–302 (2018).
15. R. H. Crabtree, *Energy Production and Storage: Inorganic Chemical Strategies for a Warming World* (John Wiley., 2013).
16. A. Afzal, A. Kausar, M. Siddiq, Perspectives of Polystyrene Composite with Fullerene, Carbon Black, Graphene, and Carbon Nanotube: A Review. *Polym. - Plast. Technol. Eng.* **55**, 1988–2011 (2016).
17. A. Matsumuro, Y. Takada, Y. Takahashi, I. Kondo, M. Senoo, Mechanical Properties of C60 Bulk Materials Synthesized at High Pressure. *Rev. High Press. Sci. Technol. No Kagaku To Gijutsu*. **7**, 823–825 (1998).
18. A. Peigney, C. Laurent, E. Flahaut, R. R. Bacsa, A. Rousset, Specific surface area of carbon nanotubes and bundles of carbon nanotubes. *Carbon*. **39**, 507–514 (2001).

19. S. Liu, V. S. Chevali, Z. Xu, D. Hui, H. Wang, A review of extending performance of epoxy resins using carbon nanomaterials. *Compos. Part B Eng.* **136**, 197–214 (2018).

20. H. Qiu, J. Yang, in *Industrial applications of carbon nanotubes*, P. Huisheng, L. Qingwen, C. Tao, Eds. (2017), pp. 47–69.

21. B. Peng *et al.*, Measurements of near-ultimate strength for multiwalled carbon nanotubes and irradiation-induced crosslinking improvements. *Nat. Nanotechnol.* **3**, 626–631 (2008).

22. D. Kondej, T. R. Sosnowski, Interactions of Carbon Nanotubes and Carbon Nanohorns with a Model Membrane Layer and Lung Surfactant in Vitro. *J. Nanomater.* (2019), doi:10.1155/2019/9457683.

23. Y. Tao *et al.*, Conductive and mesoporous single-wall carbon nanohorn/organic aerogel composites. *Langmuir*. **23**, 9155–9157 (2007).

24. Y. Nan, B. Li, X. Zhao, X. Song, L. Su, Probing the mechanical properties of carbon nanohorns subjected to uniaxial compression and hydrostatic pressure. *Carbon*. **125**, 236–244 (2017).

25. Z. He *et al.*, Enhanced power-conversion efficiency in polymer solar cells using an inverted device structure. *Nat. Photonics*. **6**, 591–595 (2012).

26. M. Yoon, S. Yang, E. Wang, Z. Zheng, Charged fullerenes as high-capacity hydrogen storage media. *Nano Lett.* **7**, 2578–2583 (2007).

27. R. Partha, J. L. Conyers, Biomedical applications of functionalized fullerene-based nanomaterials. *Int. J. Nanomedicine*. **4**, 261–275 (2009).

28. I. Jeon, R. Xiang, A. Shawky, Y. Matsuo, S. Maruyama, Single-Walled Carbon Nanotubes in Emerging Solar Cells: Synthesis and Electrode Applications. *Adv. Energy Mater.* **9**, 1–27 (2018).

29. Z. Yang *et al.*, Carbon nanotube- and graphene-based nanomaterials and applications in high-voltage supercapacitor: A review. *Carbon*. **141**, 467–480 (2019).

30. I. V. Zaporotskova, N. P. Boroznina, Y. N. Parkhomenko, L. V. Kozhitov, Carbon nanotubes: Sensor properties. A review. *Mod. Electron. Mater.* **2**, 95–105 (2016).

31. J. Xu *et al.*, Single wall carbon nanohorn as a drug carrier for controlled release. *Chem. Phys. Lett.* **461**, 189–192 (2008).

32. K. Ajima *et al.*, Carbon nanohorns as anticancer drug carriers. *Mol. Pharm.* **2**, 475–480 (2005).

33. X. Liu, L. Shi, W. Niu, H. Li, G. Xu, Amperometric glucose biosensor based on single-walled carbon nanohorns. *Biosens. Bioelectron.* **23**, 1887–1890 (2008).

34. L. Shi *et al.*, Hydrogen peroxide biosensor based on direct electrochemistry of soybean peroxidase immobilized on single-walled carbon nanohorn modified electrode. *Biosens. Bioelectron.* **24**, 1159–1163 (2009).

35. F. Yang *et al.*, Highly sensitive impedimetric immunosensor based on single-walled carbon nanohorns as labels and bienzyme biocatalyzed precipitation as enhancer for cancer biomarker detection. *Biosens. Bioelectron.* **55**, 360–365 (2014).

36. D. Wen *et al.*, A biofuel cell with a single-walled carbon nanohorn-based bioanode

operating at physiological condition. *Biosens. Bioelectron.* **25**, 1544–1547 (2010).

37. K. S. Novoselov *et al.*, Electric Field Effect in Atomically Thin Carbon Films. *Science*. **306**, 666–669 (2004).

38. P. R. Wallace, The band theory of graphite. *Phys. Rev.* **71**, 622–634 (1947).

39. A. Krishnan *et al.*, Graphitic cones and the nucleation of curved carbon surfaces. *Nature*. **388**, 451–454 (1997).

40. A. K. Geim, K. S. Novoselov, The rise of graphene. *Nat. Mater.* **6**, 183–191 (2007).

41. R. R. Nair *et al.*, Fine Structure Constant Defines Visual Transparency of Graphene. *Science*. **320**, 1308–1308 (2008).

42. Y. Gao, Graphene and Polymer Composites for Supercapacitor Applications: a Review. *Nanoscale Res. Lett.* **12** (2017), doi:10.1186/s11671-017-2150-5.

43. A. Nag, A. Mitra, S. C. Mukhopadhyay, Graphene and its sensor-based applications: A review. *Sensors Actuators, A Phys.* **270**, 177–194 (2018).

44. G. Shi *et al.*, Graphene Platelets and Their Polymer Composites: Fabrication, Structure, Properties, and Applications. *Adv. Funct. Mater.* **28**, 1706705 (2018).

45. X. Li, L. Zhi, Graphene hybridization for energy storage applications. *Chem. Soc. Rev.* **47**, 3189–3216 (2018).

46. D. G. Papageorgiou, I. A. Kinloch, R. J. Young, Mechanical properties of graphene and graphene-based nanocomposites. *Prog. Mater. Sci.* **90**, 75–127 (2017).

47. C. S. Ruiz-Vargas *et al.*, Softened elastic response and unzipping in chemical vapor deposition graphene membranes. *Nano Lett.* **11**, 2259–2263 (2011).

48. R. J. T. Nicholl *et al.*, The effect of intrinsic crumpling on the mechanics of free-standing graphene. *Nat. Commun.* **6** (2015), doi:10.1038/ncomms9789.

49. R. J. Young, D. Lu, R. J. Day, W. F. Knoff, H. A. Davis, Relationship between structure and mechanical properties for aramid fibres. *J. Mater. Sci.* **27**, 5431–5440 (1992).

50. T. Deák, T. Czigány, Chemical Composition and Mechanical Properties of Basalt and Glass Fibers: A Comparison. *Text. Res. J.* **79**, 645–651 (2009).

51. M. L. Minus, S. Kumar, The processing, properties, and structure of carbon fibers. *J. Miner. Met. Mater. Soc.* **57**, 52–58 (2005).

52. X. Chen, C. M. Dmuchowski, C. Park, C. C. Fay, C. Ke, Quantitative Characterization of Structural and Mechanical Properties of Boron Nitride Nanotubes in High Temperature Environments. *Sci. Rep.* **7**, 1–9 (2017).

53. L. Qingkun, S. Yi, L. Zhiyuan, Z. Yu, Lonsdaleite - A material stronger and stiffer than diamond. *Scr. Mater.* **65**, 229–232 (2011).

54. X. Dong, Y. C. Shin, Multiscale Modeling for Predicting the Mechanical Properties of Silicon Carbide Ceramics. *J. Am. Ceram. Soc.* **99**, 1006–1014 (2016).

55. S. M. Beden, S. Abdullah, A. K. Ariffin, Fatigue Life Prediction of Different Steel Materials with Variable Amplitude Fatigue Life Prediction of Different Steel Materials with Variable

Amplitude Loadings (2008), doi:10.13140/2.1.1930.0167.

56. E. Pop, V. Varshney, A. K. a. K. Roy, Thermal properties of graphene: Fundamentals and applications. *Therm. Prop. graphene Fundam. Appl.* **37** (2012).

57. S. Chen *et al.*, Raman measurements of thermal transport in suspended monolayer graphene of variable sizes in vacuum and gaseous environments. *ACS Nano*. **5**, 321–328 (2011).

58. A. A. Balandin, Thermal properties of graphene and nanostructured carbon materials. *Nat. Mater.* **10**, 569–581 (2011).

59. N. Stojanovic, J. M. Berg, D. H. S. Maithripala, M. Holtz, Direct measurement of thermal conductivity of aluminum nanowires. *Appl. Phys. Lett.* **95**, 93–96 (2009).

60. G. P. Akishin *et al.*, Thermal conductivity of beryllium oxide ceramic. *Refract. Ind. Ceram.* **50**, 465–468 (2009).

61. J. Zhong, D. Liu, Z. Li, X. Sun, High thermal conductivity materials and their application on the electronic products. *2012 IEEE Asia-Pacific Conf. Antennas Propagation, APCAP 2012 - Proc.*, 173–175 (2012).

62. A. Franco Júnior, D. J. Shanafield, Thermal conductivity of polycrystalline aluminum nitride (AlN) ceramics. *Cerâmica*. **50**, 247–253 (2004).

63. J. R. Davis, *Copper and copper alloys* (2001).

64. Q. Cai *et al.*, High thermal conductivity of high-quality monolayer boron nitride and its thermal expansion. *Sci. Adv.* **5** (2019), doi:10.1126/sciadv.aav0129.

65. S. Y. Zhou *et al.*, Substrate-induced bandgap opening in epitaxial graphene. *Nat. Mater.* **6**, 770–775 (2007).

66. T. Ando, The electronic properties of graphene and carbon nanotubes. *NPG Asia Mater.* **1**, 17–21 (2009).

67. N. W. Ashcroft, D. N. Mermin, *Solid state physics* (Academic Press, 1976).

68. K. S. Novoselov *et al.*, Two-dimensional gas of massless Dirac fermions in graphene. *Nature*. **438**, 197–200 (2005).

69. F. C. Walsh, Electrode reactions in metal finishing. *Trans. Inst. Met. Finish.* **69**, 4–7 (1991).

70. S. S. Dihrab, K. Sopian, A. Zaharim, Membrane and Bipolar Plates Materials for Regenerative Fuel Cells. *Smo 08 Proc. 8th Wseas Int. Conf. Simul. Model. Optim.*, 183–188 (2008).

71. U. K. Muhammad, S. Umar, Experimental Performance Investigations and Evaluation of Base Metals Thermocouples. *Int. J. Mod. Appl. Phys.* **3**, 26–37 (2013).

72. F. Bonaccorso *et al.*, Production, Processing and Placement of Graphene and Two Dimensional Crystals. *Mater. Today*. **15**, 564–589 (2012).

73. A. C. Ferrari *et al.*, Science and technology roadmap for graphene, related two-dimensional crystals, and hybrid systems. *Nanoscale*. **7**, 4598–4810 (2015).

74. G. E. Acheson, United States Patent Office. *United States Pat. Off.* (1896), , doi:10.1145/178951.178972.

75. A. Charrier *et al.*, Solid-state decomposition of silicon carbide for growing ultra-thin heteroepitaxial graphite films. *J. Appl. Phys.* **92**, 2479–2484 (2002).

76. N. Mishra, J. Boeckl, N. Motta, F. Iacopi, Graphene growth on silicon carbide: A review. *Phys. Status Solidi Appl. Mater. Sci.* **213**, 2277–2289 (2016).

77. K. V. Emtsev, F. Speck, T. Seyller, L. Ley, J. D. Riley, Interaction, growth, and ordering of epitaxial graphene on SiC{0001} surfaces: A comparative photoelectron spectroscopy study. *Phys. Rev. B - Condens. Matter Mater. Phys.* **77**, 1–10 (2008).

78. L. F. S. Alves *et al.*, in *Brazilian Power Electronics Conference (COBEP)* (2017), pp. 1–8.

79. M. Beshkova, L. Hultman, R. Yakimova, Device applications of epitaxial graphene on silicon carbide. *Vacuum*. **128**, 186–197 (2016).

80. C. Yu *et al.*, Quasi-free-standing bilayer epitaxial graphene field-effect transistors on 4H-SiC (0001) substrates. *Appl. Phys. Lett.* **108** (2016), doi:10.1063/1.4939591.

81. O. Habibpour, Z. S. He, W. Strupinski, N. Rorsman, H. Zirath, Wafer scale millimeter-wave integrated circuits based on epitaxial graphene in high data rate communication. *Sci. Rep.* **7**, 1–8 (2017).

82. M. Chen, R. C. Haddon, R. Yan, E. Bekyarova, Advances in transferring chemical vapour deposition graphene: A review. *Mater. Horizons*. **4**, 1054–1063 (2017).

83. H. Okamoto, *Desk handbook: Phase Diagrams for Binary Alloys* (ASM International, 2000).

84. A. Reina *et al.*, Growth of large-area single- and Bi-layer graphene by controlled carbon precipitation on polycrystalline Ni surfaces. *Nano Res.* **2**, 509–516 (2009).

85. S. Amini, J. Garay, G. Liu, A. A. Balandin, R. Abbaschian, Growth of large-area graphene films from metal-carbon melts. *J. Appl. Phys.* **108** (2010), doi:10.1063/1.3498815.

86. J. H. Gao *et al.*, Graphene growth on a Pt(111) substrate by surface segregation and precipitation. *Nanotechnology*. **23** (2012), doi:10.1088/0957-4484/23/5/055704.

87. M. I. Kairi, M. Khavarian, S. A. Bakar, B. Vigolo, A. R. Mohamed, Recent trends in graphene materials synthesized by CVD with various carbon precursors. *J. Mater. Sci.* **53**, 851–879 (2018).

88. C. Mattevi, H. Kim, M. Chhowalla, A review of chemical vapour deposition of graphene on copper. *J. Mater. Chem.* **21**, 3324–3334 (2011).

89. X. Li *et al.*, Large-area synthesis of high-quality and uniform graphene films on copper foils. *Science*. **324**, 1312–1314 (2009).

90. G. A. López, E. J. Mittemeijer, The solubility of C in solid Cu. *Scr. Mater.* **51**, 1–5 (2004).

91. X. Li *et al.*, Transfer of large-area graphene films for high-performance transparent conductive electrodes. *Nano Lett.* **9**, 4359–4363 (2009).

92. S. Deng, V. Berry, Wrinkled, rippled and crumpled graphene: An overview of formation mechanism, electronic properties, and applications. *Mater. Today*. **19**, 197–212 (2016).

93. X. Liang *et al.*, Toward clean and crackless transfer of graphene. *ACS Nano*. **5**, 9144–9153 (2011).

94. F. Bonaccorso, Z. Sun, T. Hasan, A. C. Ferrari, Graphene photonics and optoelectronics. *Nat. Photonics*. **4**, 611–622 (2010).

95. C. O. Kim *et al.*, High photoresponsivity in an all-graphene p–n vertical junction photodetector. *Nat. Commun.* **5**, 3249 (2014).

96. Y. Huang *et al.*, Highly transparent light emitting diodes on graphene encapsulated Cu nanowires network. *Sci. Rep.* **8** (2018), doi:10.1038/s41598-018-31903-7.

97. J. Pu *et al.*, Chemical vapor deposition growth of few-layer graphene for transparent conductive films. *RSC Adv.* **5**, 44142–44148 (2015).

98. E. O. Polat *et al.*, Synthesis of Large Area Graphene for High Performance in Flexible Optoelectronic Devices. *Sci. Rep.* **5** (2015), doi:10.1038/srep16744.

99. M. Uz *et al.*, Fabrication of High-resolution Graphene-based Flexible Electronics via Polymer Casting. *Sci. Rep.* **9** (2019), doi:10.1038/s41598-019-46978-z.

100. X. Lu, M. Yu, H. Huang, R. S. Ruoff, Tailoring graphite with the goal of achieving single sheets. *Nanotechnology*. **10**, 269–272 (1999).

101. K. S. Novoselov *et al.*, Two-dimensional atomic crystals. *Proc. Natl. Acad. Sci. U. S. A.* **102**, 10451–10453 (2005).

102. F. Bonaccorso *et al.*, Production, Processing and Placement of Graphene and Two Dimensional Crystals. *Mater. Today*. **15**, 564–589 (2012).

103. X. Lu, M. Yu, H. Huang, R. S. Ruoff, Tailoring graphite with the goal of achieving single sheets. *Nanotechnology*. **10**, 269–272 (1999).

104. C. Casiraghi *et al.*, Rayleigh Imaging of Graphene and Graphene Layers. *Nanoletters*. **7**, 2711–2717 (2007).

105. Y. Xu, H. Cao, Y. Xue, B. Li, W. Cai, Liquid-phase exfoliation of graphene: An overview on exfoliation media, techniques, and challenges. *Nanomaterials*. **8** (2018), doi:10.3390/nano8110942.

106. W. Yang, C. Wang, Graphene and the related conductive inks for flexible electronics. *J. Mater. Chem. C*. **4**, 7193–7207 (2016).

107. P. G. Karagiannidis *et al.*, Microfluidization of Graphite and Formulation of Graphene-Based Conductive Inks. *ACS Nano*. **11**, 2742–2755 (2017).

108. L. G. B. Machuno *et al.*, Multilayer graphene films obtained by dip coating technique. *Mater. Res.* **18**, 775–780 (2015).

109. J. Liu, L. Hua, S. Li, M. Yu, Graphene dip coatings: An effective anticorrosion barrier on aluminum. *Appl. Surf. Sci.* **327**, 241–245 (2015).

110. E. B. Secor, P. L. Prabhumirashi, K. Puntambekar, M. L. Geier, M. C. Hersam, Inkjet printing of high conductivity, flexible graphene patterns. *J. Phys. Chem. Lett.* **4**, 1347–1351 (2013).

111. F. Torrisi *et al.*, Inkjet-Printed Graphene Electronics. *ACS Nano*. **6**, 2992–3006 (2012).

112. A. Capasso *et al.*, Ink-jet printing of graphene for fl exible electronics : An environmentally-friendly approach (2015), doi:10.1016/j.ssc.2015.08.011.

113. T. Carey, C. Jones, F. Le Moal, D. Deganello, F. Torrisi, Spray-Coating Thin Films on Three-Dimensional Surfaces for a Semitransparent Capacitive-Touch Device. *ACS Appl. Mater. Interfaces*. **10**, 19948–19956 (2018).

114. J. N. Israelachvili, *Intermolecular and surface forces* (Academic Press, ed. 3, illustr, 2015).

115. C. M. Hansen, *Hansen solubility parameters: a user's handbook* (Taylor & Francis group, 2007).

116. Y. Hernandez, M. Lotya, D. Rickard, S. D. Bergin, J. N. Coleman, Measurement of Multicomponent Solubility Parameters for Graphene Facilitates Solvent Discovery. *Langmuir*. **26**, 3208–3213 (2010).

117. J. N. Coleman, Liquid exfoliation of defect-free graphene. *Acc. Chem. Res.* **46**, 14–22 (2012).

118. Y. Hernandez *et al.*, High-yield production of graphene by liquid-phase exfoliation of graphite. *Nat. Nanotechnol.* **3**, 563–568 (2008).

119. W. W. Liu, B. Y. Xia, X. X. Wang, J. N. Wang, Exfoliation and dispersion of graphene in ethanol-water mixtures. *Front. Mater. Sci.* **6**, 176–182 (2012).

120. S. Liang *et al.*, In-situ exfoliated graphene for high-performance water-based lubricants. *Carbon*. **96**, 1181–1190 (2016).

121. S. Wang, M. Yi, Z. Shen, X. Zhang, S. Ma, Adding ethanol can effectively enhance the graphene concentration in water/surfactant solutions. *RCS Adv.* **4**, 25374–25378 (2014).

122. R. J. Smith, M. Lotya, J. N. Coleman, The importance of repulsive potential barriers for the dispersion of graphene using surfactants. *New J. Phys.* **12**, 125008–125019 (2010).

123. M. Lotya *et al.*, Liquid Phase Production of Graphene by Exfoliation of Graphite in Surfactant / Water Solutions. *J. Am. Chem. Soc.* **131**, 3611–3620 (2009).

124. S. Vadukumpully, J. Paul, S. Valiyaveettil, Cationic surfactant mediated exfoliation of graphite into graphene flakes. *Carbon*. **47**, 3288–3294 (2009).

125. Z. Sun *et al.*, High-yield exfoliation of graphite in acrylate polymers: A stable few-layer graphene nanofluid with enhanced thermal conductivity. *Carbon*. **64**, 288–294 (2013).

126. S. Perumal, H. M. Lee, I. W. Cheong, High-concentration graphene dispersion stabilized by block copolymers in ethanol. *J. Colloid Interface Sci.* **497**, 359–367 (2017).

127. Y. T. Liang, M. C. Hersam, Highly concentrated graphene solutions via polymer enhanced solvent exfoliation and iterative solvent exchange. *J. Am. Chem. Soc.* **132**, 17661–17663 (2010).

128. J. W. Lee *et al.*, In-situ preparation of graphene/poly(styrenesulfonic acid-graft-polyaniline) nanocomposite via direct exfoliation of graphite for supercapacitor application. *Carbon*. **105**, 191–198 (2016).

129. H. Sun *et al.*, Binder-free graphene as an advanced anode for lithium batteries. *J. Mater. Chem. A*. **4**, 6886–6895 (2016).

130. X. Tong, C. Xie, L. Si, J. Che, Y. Xiao, Transparent and highly conductive liquid-phase exfoliated graphite films treated with low-temperature air-annealing. *Mater. Chem. Phys.* **143**, 85–92 (2013).

131. A. Al Shboul, C. Trudeau, S. Cloutier, M. Siaj, J. P. Claverie, Graphene dispersions in alkanes: Toward fast drying conducting inks. *Nanoscale*. **9**, 9893–9901 (2017).

132. L. Guardia *et al.*, High-throughput production of pristine graphene in an aqueous dispersion assisted by non-ionic surfactants. *Carbon*. **49**, 1653–1662 (2011).

133. Z. Shen, J. Li, M. Yi, X. Zhang, S. Ma, Preparation of graphene by jet cavitation. *Nanotechnology*. **22** (2011), doi:10.1088/0957-4484/22/36/365306.

134. U. Khan, A. O'Neill, M. Lotya, S. De, J. N. Coleman, High-concentration solvent exfoliation of graphene. *Small*. **7**, 864–871 (2010).

135. K. R. Paton *et al.*, Scalable production of large quantities of defect-free few-layer graphene by shear exfoliation in liquids. *Nat. Mater.* **13**, 624–630 (2014).

136. S. Sajid, A. Shah, H. Nasir, Liquid-Phase Exfoliation of Few-Layer Graphene and Effect of Sonication Time on Concentration of Produced Few Layer Graphene. *Nano Hybrids Compos.* **14**, 17–24 (2017).

137. H. Zhao, Y. Qiao, Y. Zang, Q. Zhang, Preparation of few-layer graphene by liquid-phase exfoliation and its tribological properties as deionized water additive. *J. Chinese Chem. Soc.* **43**, 437–444 (2015).

138. A. O'Neill, U. Khan, P. N. Nirmalraj, J. Boland, J. N. Coleman, Graphene dispersion and exfoliation in low boiling point solvents. *J. Phys. Chem. C*. **115**, 5422–5428 (2011).

139. S. L. Zhang, Z. Zhang, W. C. Yang, High-yield exfoliation of graphene using ternary-solvent strategy for detecting volatile organic compounds. *Appl. Surf. Sci.* **360**, 323–328 (2016).

140. Y. Çelik *et al.*, A comparative study on few-layer graphene production by exfoliation of different starting materials in a low boiling point solvent. *FlatChem*. **1**, 74–88 (2017).

141. U. Khan *et al.*, Solvent-exfoliated graphene at extremely high concentration. *Langmuir*. **27**, 9077–9082 (2011).

142. J. Lyklema, The surface tension of pure liquids. *Colloids Surf., A*. **156**, 413–421 (1999).

143. H. M. Solomon *et al.*, 1-methyl-2-pyrrolidone (nmp): reproductive and developmental toxicity study by inhalation in the rat. *Drug Chem. Toxicol.* **18**, 271–293 (2008).

144. J. J. Jasper, The Surface Tension of Pure Liquid Compounds. *J. Phys. Chem. Ref. Data*. **1**, 841–1010 (1972).

145. T. Carey *et al.*, Fully inkjet-printed two-dimensional material field- effect heterojunctions for wearable and textile electronics. *Nat. Commun.* **8**, 1202 (2017).

146. J. Baker, D. Deganello, D. T. Gethin, T. M. Watson, Flexographic printing of graphene nanoplatelet ink to replace platinum as counter electrode catalyst in flexible dye sensitised solar cell. *Mater. Res. Innov.* **18**, 86–90 (2014).

147. V. H. Pham *et al.*, Fast and simple fabrication of a large transparent chemically-converted graphene film by spray-coating. *Carbon*. **48**, 1945–1951 (2010).

148. J. Christesen, thesis, College of William and Mary (2011).

149. A. G. D'Aloia *et al.*, Electrical, mechanical and electromechanical properties of graphene-

thermoset polymer composites produced using acetone-DMF solvents. *Polymers (Basel).* **10**, 82 (2018).

150. L. Zhang, Z. Miao, Z. Hao, J. Liu, Exfoliating and dispersing few-layered graphene in low-boiling-point organic solvents towards solution-processed optoelectronic device applications. *Chem. - An Asian J.* **11**, 1441–1446 (2016).

151. D. A. C. Brownson, J. P. Metters, D. K. Kampouris, C. E. Banks, Graphene electrochemistry: Surfactants inherent to graphene can dramatically effect electrochemical processes. *Electroanalysis*. **23**, 894–899 (2011).

152. M. Lotya, P. J. King, U. Khan, S. De, J. N. Coleman, High-concentration, surfactant-stabilized graphene dispersions. *ACS Nano*. **4**, 3155–3162 (2010).

153. P. Turner, M. Hodnett, R. Dorey, J. D. Carey, Controlled Sonication as a Route to in-situ Graphene Flake Size Control. *Sci. Rep.* **9**, 1–8 (2019).

154. A. E. Del Rio Castillo *et al.*, High yield production of 2D crystals by wet-jet milling. *Mater. Horizons*. **5**, 890–904 (2018).

155. T. S. Tran, J. Park, S. Yoo, T. Lee, High shear-induced exfoliation of graphite into high quality graphene by Taylor–Couette flow. *RSC Adv.* **6**, 12003–12008 (2016).

156. A. Ambrosi, M. Pumera, Electrochemically Exfoliated Graphene and Graphene Oxide for Energy Storage and Electrochemistry Applications. *Chem. - A Eur. J.* **22**, 153–159 (2016).

157. F. Jiang, Y. Yu, Y. Wang, A. Feng, L. Song, A novel synthesis route of graphene via microwave assisted intercalation-exfoliation of graphite. *Mater. Lett.* **200**, 39–42 (2017).

158. A. M. Abdelkader, A. J. Cooper, R. A. W. Dryfe, I. A. Kinloch, How to get between the sheets: A review of recent works on the electrochemical exfoliation of graphene materials from bulk graphite. *Nanoscale*. **7**, 6944–6956 (2015).

159. B. D. Ossonon, D. Bélanger, Functionalization of graphene sheets by the diazonium chemistry during electrochemical exfoliation of graphite. *Carbon*. **111**, 83–93 (2017).

160. K. Muthoosamy, S. Manickam, State of the art and recent advances in the ultrasound-assisted synthesis, exfoliation and functionalization of graphene derivatives. *Ultrason. Sonochem.* **39**, 478–493 (2017).

161. K. S. Suslick, D. J. Flannigan, Inside a Collapsing Bubble : Sonoluminescence and the Conditions During Cavitation. *Ann. Rev. Phys. Chem.* **59**, 659–683 (2008).

162. J. Jablonská, M. Kozubková, in *AIP Conference Proceedings* (2016), vol. 1768.

163. A. A. McKillop, W. L. Dunkley, R. L. Brockmeyer, R. L. Perry, The cavitation theory of homogenization. *J. Dairy Sci.* **38**, 273–283 (1955).

164. C. E. Brennen, *Cavitation and Bubble Dynamics* (1995).

165. M. Yi, Z. Shen, J. Zhu, A fluid dynamics route for producing graphene and its analogues. *Chinese Sci. Bull.* **59**, 1794–1799 (2014).

166. J. Gallego-Juárez, K. F. Graff, *Power ultrasonics* (Woodhead publishing, 2015).

167. M. Malaki, A. Maleki, R. S. Varma, MXenes and ultrasonication. *J. Mater. Chem. A*. **7**, 10843–

10857 (2019).

168. A. Ciesielski, P. Samorì, Graphene via sonication assisted liquid-phase exfoliation. *Chem. Soc. Rev.* **43**, 381–398 (2014).

169. J. Hassoun *et al.*, An Advanced Lithium-Ion Battery Based on a Graphene Anode and a Lithium Iron Phosphate Cathode. *Nano Lett.* **14**, 4901–4906 (2014).

170. A. Capasso *et al.*, Ink-jet printing of graphene for flexible electronics: An environmentally-friendly approach. *Solid State Commun.* **224**, 53–63 (2015).

171. Z. Baig *et al.*, Investigation of tip sonication effects on structural quality of graphene nanoplatelets (GNPs) for superior solvent dispersion. *Ultrason. Sonochem.* **45**, 133–149 (2018).

172. X. Cai, Z. Jiang, X. Zhang, X. Zhang, Effects of Tip Sonication Parameters on Liquid Phase Exfoliation of Graphite into Graphene Nanoplatelets. *Nanoscale Res. Lett.* **13** (2018), doi:10.1186/s11671-018-2648-5.

173. J. L. Capelo-Martínez, *Ultrasound in Chemistry: Analytical Applications* (Wiley-VCH Verlag GmbH & Co. KGaA, 2008).

174. K. Kouroupis-Agalou *et al.*, Fragmentation and exfoliation of 2-dimensional materials: A statistical approach. *Nanoscale*. **6**, 5926–5933 (2014).

175. J. Schumacher, Relation between shear parameter and Reynolds number in statistically stationary turbulent shear flows (2014), doi:10.1063/1.1764431.

176. O. Reynolds, An Experimental Investigation of the Circumstances Which Determine Whether the Motion of Water Shall Be Direct or Sinuous, and of the Law of Resistance in Parallel Channels. *Philos. Trans. R. Soc. London*. **174**, 935–982 (1883).

177. M. Rao, S. Khandekar, in *Proceedings of 19th National and 8th ISHMT-ASME Heat and Mass Transfer Conference* (1883).

178. S. Liang *et al.*, Effects of Processing Parameters on Massive Production of Graphene by Jet Cavitation. *J. Nanosci. Nanotechnol.* **15**, 2686–2694 (2015).

179. Y. Arao, Y. Mizuno, K. Araki, M. Kubouchi, Mass production of high-aspect-ratio few-layer-graphene by high-speed laminar flow. *Carbon*. **102**, 330–338 (2016).

180. K. R. Paton, J. Anderson, A. J. Pollard, T. Sainsbury, Production of few-layer graphene by microfluidization. *Mater. Res. Express*. **4** (2017), doi:10.1088/2053-1591/aa5b24.

181. T. J. Nacken, C. Damm, J. Walter, A. Ruger, W. Peukert, Delamination of Graphite in a high pressure homogenizer. *RCS Adv.* **5**, 57328–57338 (2015).

182. S. B. Awad, R. Nagarajan, in *Developments in Surface Contamination and Cleaning - Particle Deposition, Control and Removal* (Elsevier, 2010), pp. 225–280.

183. T. Leighton, *The acoustic bubble* (Academic P., 2012).

184. T. Svedberg, K. O. Pedersen, The Ultracentrifuge. *J. Phys. Chem.* **44**, 952–953 (1940).

185. A. A. Green, M. C. Hersam, Solution phase production of graphene with controlled thickness via density differentiation. *Nano Lett.* **9**, 4031–4036 (2009).

186. G. Pickels, Sedimentation in the angle centrifuge. *J. Gen. Physiol.* **26**, 341–359 (1943).

187. A. Esau *et al.*, Solution processed black phosphorus in low boiling point solvents as efficient anodes for Li-ion battery, 8563 (2016).

188. G. Kakavelakis *et al.*, Size-Tuning of WSe2 Flakes for High Efficiency Inverted Organic Solar Cells. *ACS Nano*. **11**, 3517–3531 (2017).

189. H. Sun *et al.*, How much does size really matter ? Exploring the limits of graphene as Li ion battery anode material. *Solid State Commun.* **251**, 88–93 (2017).

190. C. Lee, X. Wei, J. W. Kysar, J. Hone, Measurement of the elastic properties and elastic strength of monolayer graphene. *Science*. **321**, 385–388 (2008).

191. B. Z. Jang, A. Zhamu, Processing of nanographene platelets (NGPs) and NGP nanocomposites: A review. *J. Mater. Sci.* **43**, 5092–5101 (2008).

192. H. Lammer, Sporting goods with graphene material (2013).

193. E. J. Siochi, Graphene in the sky and beyond. *Nat. Publ. Gr.* **9**, 745–747 (2014).

194. A. Elmarakbi, W. L. Azoti, in *10th International Conference on Composite Science and Technology* (Lisbon, Portugal, 2015), pp. 2-4 September.

195. H. Company, Head - Graphenext, (available at https://www.head.com/it-IT/racquetsports/technology/graphene-xt/).

196. Vittoria, Vittoria - Graphene 2.0, (available at https://www.vittoria.com/us/graphene-technology).

197. Graphene flagship, The Leading Edge: Graphene Flagship leads the way in graphene composites for aerospace applications, (available at https://graphene-flagship.eu/news/Pages/The-Leading-Edge-Graphene-Flagship-leads-the-way-in-graphene-composites-for-aerospace-applications.aspx).

198. Graphene-info.com, Ford to release graphene-enhanced cars by the end of 2018, (available at https://www.graphene-info.com/ford-release-graphene-enhanced-cars-end-2018).

199. Fadel, Fadel - freshoes, (available at http://freshoes.it/).

200. Momo, Momo design products, (available at https://www.momodesign.com/products/fgtr-graphene-1-0?_pos=1&_sid=5af46632c&_ss=r).

201. Y. Chen, Y. Qingwei, Advances in graphene-based polymer composites with high thermal conductivity. *Veruscript Funct. Nanomater.* (2018), doi:10.22261/OOSB06.

202. Fadel, IIT and FADEL unveil graphene-enhanced shoes, (available at https://www.graphene-info.com/iit-and-fadel-unveil-graphene-enhanced-shoes).

203. J. S. Bunch *et al.*, Impermeable atomic membranes from graphene sheets. *Nanoletters*. **8**, 2458–2462 (2008).

204. L. Tsetseris, S. T. Pantelides, Graphene: An impermeable or selectively permeable membrane for atomic species? *Carbon*. **67**, 58–63 (2014).

205. C. Ataca, H. Şahin, S. Ciraci, Stable, single-layer MX 2 transition-metal oxides and dichalcogenides in a honeycomb-like structure. *J. Phys. Chem. C*. **116**, 8983–8999 (2012).

206. S. Nazarpour, W. R. Waite, *Graphene Technology: From Laboratory to Fabrication* (2016).

207. D. Berman, A. Erdemir, A. V Sumant, Graphene : a new emerging lubricant. *Mater. today*. **17**, 31–42 (2014).

208. A. K. Kasar, P. L. Menezes, Synthesis and recent advances in tribological applications of graphene. *Int. J. Adv. Manuf. Technol.* **97**, 3999–4019 (2018).

209. P. K. Mallick, *Processing of Polymer Matrix Composites: Processing and Applications* (2017).

210. J. Kumar, S. Katiyar, V. Bhattacharya, K. Patel, K. Vikram, *Automotive tribology* (2019).

211. Pacmachinery - nozzle vacuum sealers, (available at https://www.pacmachinery.com/packagingaids/product_category/nozzle-vacuum-sealers/).

212. Gear synchro, (available at https://x-engineer.org/automotive-engineering/drivetrain/transmissions/gear-synchro/).

213. J. R. Potts, D. R. Dreyer, C. W. Bielawski, R. S. Ruoff, Graphene-based polymer nanocomposites. *Polymer*. **52**, 5–25 (2011).

214. S. Colonna *et al.*, Effect of processing conditions on the thermal and electrical conductivity of poly (butylene terephthalate) nanocomposites prepared via ring-opening polymerization. *Mater. Des.* **119**, 124–132 (2017).

215. V. Mittal, S. Kim, S. Neuhofer, C. Paulik, Polyethylene / graphene nanocomposites : effect of molecular weight on mechanical , thermal , rheological and morphological properties. *Colloid Polym Sci*. **294**, 691–704 (2016).

216. H. Roghani-mamaqani, V. Haddadi-asl, Edge-functionalized graphene nanoplatelets with polystyrene by atom transfer radical polymerization : grafting through carboxyl. *Polym. Int.* **63**, 1912–1923 (2014).

217. P. M. Nedorezova *et al.*, Composite Materials Based on Graphene Nanoplatelets and Polypropylene Derived via In Situ Polymerization. *Nanotechnologies Russ.* **8**, 69–80 (2013).

218. Y. B. Luo, J. S. Cheng, Q. Ma, Y. Q. Feng, J. H. Li, Graphene-polymer composite: Extraction of polycyclic aromatic hydrocarbons from water samples by stir rod sorptive extraction. *Anal. Methods*. **3**, 92–98 (2011).

219. M. A. Aldosari, A. A. Othman, E. H. Alsharaeh, Synthesis and characterization of the in situ bulk polymerization of PMMA containing graphene sheets using microwave irradiation. *Molecules*. **18**, 3152–3167 (2013).

220. K. K. Patel, R. Purohit, Improved shape memory and mechanical properties of microwave-induced thermoplastic polyurethane / graphene nanoplatelets composites. *Sensors Actuators A. Phys.* **285**, 17–24 (2019).

221. Y. Gao, F. Müller-Plathe, Increasing the Thermal Conductivity of Graphene-Polyamide-6,6 Nanocomposites by Surface-Grafted Polymer Chains: Calculation with Molecular Dynamics and Effective-Medium Approximation. *J. Phys. Chem. B*. **120**, 1336–1346 (2016).

222. Y. Wang *et al.*, Effect of Covalent Functionalization on Thermal Transport across Graphene-Polymer Interfaces. *J. Phys. Chem. C*. **119**, 12731–12738 (2015).

223. J. Gu *et al.*, Thermal Percolation Behavior of Graphene Nanoplatelets/Polyphenylene Sulfide Thermal Conductivity Composites. *Polym. Compos.* **35**, 1087–1092 (2015).

224. E. Lago, P. S. Toth, G. Pugliese, V. Pellegrini, F. Bonaccorso, Solution blending preparation of polycarbonate/graphene composite: Boosting the mechanical and electrical properties. *RSC Adv.* **6**, 97931–97940 (2016).

225. Q. Wang, Q. Meng, T. Wang, W. Guo, High-performance antistatic ethylene–vinyl acetate copolymer/high-density polyethylene composites with graphene nanoplatelets coated by polyaniline. *J. Appl. Polym.* **45303**, 1–9 (2017).

226. E. L. Papadopoulou *et al.*, Nylon 6,6/graphene nanoplatelet composite films obtained from a new solvent. *RCS Adv.* **6**, 6823–6831 (2016).

227. P. Tambe, G. M. Joshi, Effect of sodium alginate modification of graphene (by ‘ anion- π ’ type of interaction) on the mechanical and thermal properties of polyvinyl alcohol (PVA) nanocomposites. *Compos. interfaces*. **21**, 487–506 (2014).

228. P. Cataldi, L. Ceseracciu, S. Marras, A. Athanassiou, I. S. Bayer, Electrical conductivity enhancement in thermoplastic polyurethane-graphene nanoplatelet composites by stretch-release cycles. *Appl. Phys. Lett.* **110** (2017), doi:10.1063/1.4978865.

229. K. Kalaitzidou, H. Fukushima, L. T. Drzal, A new compounding method for exfoliated graphite – polypropylene nanocomposites with enhanced flexural properties and lower percolation threshold. *Compos. Sci. Technol.* **67**, 2045–2051 (2007).

230. G. Kaur, R. Adhikari, P. Cass, M. Bown, P. Gunatillake, Electrically conductive polymers and composites for biomedical applications. *RCS Adv.* **5**, 37553–37567 (2015).

231. T. Batakliev *et al.*, Effects of Graphene Nanoplatelets and Multiwall Carbon Nanotubes on the Structure and Mechanical Properties of Poly (lactic acid) Composites: a comparative study. *Appl. Sci.* **9** (2019), doi:10.3390/app9030469.

232. M. Castro, J. A. Morris, R. Ríos, A. Ans, Tribological and mechanical properties of graphene nanoplatelet/PEEK composites. *Carbon*. **141**, 107–122 (2019).

233. S. He, J. Zhang, Investigation of the conductive network formation of polypropylene / graphene nanoplatelets composites for different platelet sizes. *J. Mater. Sci.* **52**, 13103–13119 (2017).

234. S. Dul *et al.*, Effect of graphene nanoplatelets structure on the properties of acrylonitrile-butadiene-styrene composites. *Polym. Compos.* **40**, E285–E300 (2019).

235. H. Kim *et al.*, Graphene/polyethylene nanocomposites: Effect of polyethylene functionalization and blending methods. *Polymer*. **52**, 1837–1846 (2011).

236. W. Liu, I.-H. Do, H. Fukushima, L. T. Drzal, Influence of Processing on Morphology, Electrical Conductivity and Flexural Properties of Exfoliated Graphite Nanoplatelets-Polyamide Nanocomposites. *Carbon Lett.* **11**, 279–284 (2010).

237. J. Gómez *et al.*, Processing influence on dielectric, mechanical, and electrical properties of reduced graphene oxide–TPU nanocomposites. *J. Appl. Polym. Sci.* **136**, 1–11 (2019).

238. Y. Liu, B. Fan, A. H. Delong, H. Jinbo, Thickness effect on the tensile and dynamic mechanical properties of graphene nanoplatelets-reinforced polymer nanocomposites. *Graphene*

Technol. **2**, 21–27 (2017).

239. Q. Beuguel, A. Mija, B. Vergnes, E. Peuvrel-Disdier, Structural, thermal, rheological and mechanical properties of polypropylene/graphene nanoplatelets composites: Effect of particle size and melt mixing conditions. *Polym. Eng. Sci.* **58**, 1937–1944 (2018).

240. Y. Gao, O. T. Picot, E. Bilotti, T. Peijs, Influence of filler size on the properties of poly(lactic acid) (PLA)/graphene nanoplatelet (GNP) nanocomposites. *Eur. Polym. J.* **86**, 117–131 (2017).

241. C. Vallés, A. M. Abdelkader, R. J. Young, I. A. Kinloch, Few layer graphene–polypropylene nanocomposites: the role of flake diameter. *Faraday Discuss.* **173**, 379–390 (2014).

242. C. Vallés, A. M. Abdelkader, R. J. Young, I. A. Kinloch, The effect of flake diameter on the reinforcement of few-layer graphene-PMMA composites. *Compos. Sci. Technol.* **111**, 17–22 (2015).

243. D. Verma, K. L. Goh, in *Functionalized Graphene Nanocomposites and their Derivatives* (2019), pp. 219–243.

244. A. Rane, K. Kanny, V. K. Abitha, S. Thomas, in *Synthesis of inorganic nanomaterials* (2018), pp. 121–139.

245. Pharmaceutical hot melt extrusion market, (available at https://thefinancetime.com/pharmaceutical-hot-melt-extrusion-market-major-technology-giants-in-buzz-again-milacron-holdings-coperion-gmbh-gabler-gmbh &co-kg-and-many-more/6018/).

246. T. Sabu, J. Kuruvilla, S. K. Malhotra, K. Goda, M. S. Sreekala, *Polymer Composites, Macro- and Microcomposites* (2012).

247. D. V. Rosato, M. G. Rosato, *Injection molding handbook* (2012).

248. K. Kalaitzidou, H. Fukushima, L. T. Drzal, in *20th Technical Conference of the American Society for Composites* (2005), pp. 1829–1848.

249. H. Wu, L. T. Drzal, Graphene nanoplatelet-polyetherimide composites: Revealed morphology and relation to properties. *J. Appl. Polym. Sci.* **130**, 4081–4089 (2013).

250. K. Kalaitzidou, H. Fukushima, L. T. Drzal, Multifunctional polypropylene composites produced by incorporation of exfoliated graphite nanoplatelets. *Carbon*. **45**, 1446–1452 (2007).

251. Y. Qiu *et al.*, Thermoplastic polyester elastomer nanocomposites filled with graphene: Mechanical and viscoelastic properties. *Compos. Sci. Technol.* **132**, 108–115 (2016).

252. H. C. B. Raheleh H. Pour, Azman Hassan, Mohammad Soheilmoghaddam, Mechanical, Thermal, and Morphological Properties of Graphene Reinforced Polycarbonate/Acrylonitrile Butadiene Styrene Nanocomposites. *Polym. Polym. Compos.* **16**, 101–113 (2014).

253. The injection molding process, (available at https://www.aireplastics.com/basic-injection-molding-process/).

254. S. G. Advani, E. M. Sozer, *Process Modeling in Composites Manufacturing* (CRC Press, 2002).

255. P. N. Khanam *et al.*, Melt processing and properties of linear low density polyethylene-

graphene nanoplatelet composites. *Vacuum*. **130**, 63–71 (2016).

256. M. Adel, O. El-Shazly, E. W. F. El-Wahidy, A. El-Maghraby, M. A. A. Mohamed, Eco-friendly produced lightweight structural graphene/polyamide 12 nanocomposite: Mechanical performance and the controlling microstructural mechanisms. *Polym. Eng. Sci.* **58**, 1201–1212 (2018).

257. D. Zhu *et al.*, Thermal and mechanical properties of polyamide 12/graphene nanoplatelets nanocomposites and parts fabricated by fused deposition modeling. *J. Appl. Polym. Sci.* **134**, 1–13 (2017).

258. Compression molding, (available at https://www.sciencedirect.com/topics/agricultural-and-biological-sciences/compression-molding).

259. T. D. Ngo, A. Kashani, G. Imbalzano, K. T. Q. Nguyen, D. Hui, Additive manufacturing (3D printing): A review of materials , methods , applications and challenges. *Compos. Part B*. **143**, 172–196 (2018).

260. T. et al. Campbell, Could 3D Printing Change the World? Technologies, Potential, and Implications of Additive Manufacturing. *Strateg. foresight Rep.* (2011).

261. B. Berman, 3-D printing: the new industrial revolution. *Bus. Horiz.* **55**, 155–162 (2012).

262. I. J. Petrick, T. W. Simpson, 3D Printing Disrupts Manufacturing: How Economies of One Create New Rules of Competition. *Res. Technol. Manag.* **56** (2013), doi:10.5437/08956308X5606193.

263. T. Noraihan, A. Tuan, A. M. Abdullah, H. Akil, Recent Developments in Fused Deposition Modeling-Based 3D Printing of Polymers and Their Composites. *Polym. Rev.* **59**, 589–624 (2019).

264. S. Dul, L. Fambri, A. Pegoretti, Fused deposition modelling with ABS-graphene nanocomposites. *Compos. Part A*. **85**, 181–191 (2016).

265. X. Wei *et al.*, 3D Printable Graphene Composite. *Sci. Rep.* **5**, 11181 (2015).

266. K. Gnanasekaran *et al.*, 3D printing of CNT- and graphene-based conductive polymer nanocomposites by fused deposition modeling. *Appl. Mater. Today*. **9**, 21–28 (2017).

267. K. Prashantha, F. Roger, Multifunctional properties of 3D printed poly (lactic acid)/ graphene nanocomposites by fused deposition modeling. *J. Macromol. Sci. Part A Pure Appl. Chem.* **54**, 24–29 (2017).

268. J. W. Stansbury, M. J. Idacavage, 3D printing with polymers : Challenges among expanding options and opportunities. *Dent. Mater.* **32**, 54–64 (2015).

269. O. A. Mohamed, S. H. Masood, J. L. Bhowmik, A. E. Somers, Investigation on the tribological behavior and wear mechanism of parts processed by fused deposition additive manufacturing process. *J. Manuf. Process.* **29**, 149–159 (2017).

270. R. J. Young *et al.*, The mechanics of reinforcement of polymers by graphene nanoplatelets. *Compos. Sci. Technol.* **154**, 110–116 (2018).

271. Y. Gao, O. T. Picot, W. Tu, E. Bilotti, T. Peijs, Multilayer coextrusion of graphene polymer nanocomposites with enhanced structural organization and properties. *J. Appl. Polym. Sci.*

135 (2018), doi:10.1002/app.46041.

272. A. Ye *et al.*, Poly(ethylene oxide)-promoted dispersion of graphene nanoplatelets and its effect on the properties of poly(lactic acid)/poly(butylene adipate-co-terephthalate) based nanocomposites. *Mater. Lett.* **253**, 34–37 (2019).

273. Y. Jun, J. G. Um, G. Jiang, A. Yu, A study on the effects of graphene nano-platelets (GnPs) sheet sizes from a few to hundred microns on the thermal , mechanical , and electrical properties of polypropylene (PP)/ GnPs composites. *Express Polym. Lett.* **12**, 885–897 (2018).

274. S. K. Yadav, J. W. Cho, Functionalized graphene nanoplatelets for enhanced mechanical and thermal properties of polyurethane nanocomposites. *Appl. Surf. Sci.* **266**, 360–367 (2013).

275. T. Ramanathan *et al.*, Functionalized graphene sheets for polymer nanocomposites. *Nat. Nanotechnol.* **3**, 327–331 (2008).

276. B. Das, K. Eswar Prasad, U. Ramamurty, C. N. R. Rao, Nano-indentation studies on polymer matrix composites reinforced by few-layer graphene. *Nanotechnology*. **20** (2009), doi:10.1088/0957-4484/20/12/125705.

277. Z. Guo, S. Ran, Z. Fang, Promoting dispersion of graphene nanoplatelets in polyethylene and chlorinated polyethylene by Friedel-Crafts reaction. *Compos. Sci. Technol.* **86**, 157–163 (2013).

278. W. J. Yao, B. Y. Cao, Triggering wave-domain heat conduction in graphene. *Phys. Lett. Sect. A Gen. At. Solid State Phys.* **380**, 2105–2110 (2016).

279. W. J. Yao, B. Y. Cao, Thermal wave propagation in graphene studied by molecular dynamics simulations. *Chinese Sci. Bull.* **59**, 3495–3503 (2014).

280. C. L. Choy, Thermal Conductivity of Polymers. *Polymer*. **18**, 984–1004 (1977).

281. A. Li, C. Zhang, Y.-F. Zhang, Thermal Conductivity of Graphene-Polymer Composites: Mechanisms, Properties, and Applications. *Polymers (Basel).* **9**, 437 (2017).

282. N. Burger *et al.*, Review of thermal conductivity in composites: Mechanisms, parameters and theory. *Prog. Polym. Sci.* **61**, 1–28 (2016).

283. M. Ajorloo, M. Fasihi, M. Ohshima, K. Taki, How are the thermal properties of polypropylene/graphene nanoplatelet composites affected by polymer chain configuration and size of nanofiller? *Mater. Des.* **181**, 108068 (2019).

284. H. S. Kim, H. S. Bae, J. Yu, S. Y. Kim, Thermal conductivity of polymer composites with the geometrical characteristics of graphene nanoplatelets. *Sci. Rep.* **6**, 1–9 (2016).

285. H. Jung *et al.*, High Through-Plane Thermal Conduction of Graphene Nanoflake Filled Polymer Composites Melt-Processed in an L-Shape Kinked Tube. *ACS Appl. Mater. Interfaces*. **7**, 15256–15262 (2015).

286. M. Saeidijavash *et al.*, High thermal conductivity through simultaneously aligned polyethylene lamellae and graphene nanoplatelets. *Nanoscale*. **9**, 12867–12873 (2017).

287. Z. Xu *et al.*, Relationship between the structure and thermal properties of polypropylene/graphene nanoplatelets composites for different platelet-sizes. *Compos. Sci.*

Technol. **183**, 107826 (2019).

288. L. Burk *et al.*, Mechanochemically Carboxylated Multilayer Graphene for Carbon/ABS Composites with Improved Thermal Conductivity. *Polymers (Basel).* **10**, 1088 (2018).

289. Y. Cui, S. I. Kundalwal, S. Kumar, Gas barrier performance of graphene/polymer nanocomposites. *Carbon*. **98**, 313–333 (2016).

290. M. T. Müller *et al.*, Effect of graphite nanoplate morphology on the dispersion and physical properties of polycarbonate based composites. *Materials*. **10** (2017), doi:10.3390/ma10050545.

291. D. Hofmann, M. Keinath, R. Thomann, R. Mulhaupt, Thermoplastic carbon/polyamide 12 composites containing functionalized graphene, expanded graphite, and carbon nanofillers. *Macromol. Mater. Eng.* **299**, 1329–1342 (2014).

292. K. Gaska, R. Kádár, A. Rybak, A. Siwek, S. Gubanski, Gas barrier, thermal, mechanical and rheological properties of highly aligned graphene-LDPE nanocomposites. *Polymers (Basel).* **9**, 294 (2017).

293. K. J. Berean *et al.*, Enhanced gas permeation through graphene nanocomposites. *J. Phys. Chem. C*. **119**, 13700–13712 (2015).

294. J. Jin, R. Rafiq, Y. Q. Gill, M. Song, Preparation and characterization of high performance of graphene/nylon nanocomposites. *Eur. Polym. J.* **49**, 2617–2626 (2013).

295. K. Friedrich, Polymer composites for tribological applications. *Adv. Ind. Eng. Polym. Res.* **1**, 3–39 (2018).

296. K. Friedrich, *Friction and Wear of Polymer Composites* (2012).

297. F. Mindivan, Effect of Graphene Nanoplatelets (GNPs) on Tribological and Mechanical Behaviors of Polyamide 6 (PA6). *Tribol. Ind.* **39**, 277–282 (2017).

298. M. T. Masood, E. L. Papadopoulou, I. S. Bayer, A. Athanassiou, L. Ceseracciu, Graphene and polytetrafluoroethylene synergistically improve the tribological properties and adhesion of nylon 66 coatings. *Carbon*. **123**, 26–33 (2017).

299. H. Wang, G. Xie, Z. Zhu, Z. Ying, Y. Zeng, Enhanced tribological performance of the multi-layer graphene filled poly (vinyl chloride) composites. *Compos. Part A*. **67**, 268–273 (2014).

300. B. J. Briscoe, S. K. Sinha, Wear of polymers. *Proc. Inst. Mech. Eng. Part J J. Eng. Tribol.* **216**, 401–413 (2002).

301. J. Ye, D. Burris, T. Xie, A Review of Transfer Films and Their Role in Ultra-Low-Wear Sliding of Polymers. *Lubricants*. **4**, 1–15 (2016).

302. T. Liu, B. Li, B. Lively, A. Eyler, W. Zhong, Enhanced wear resistance of high-density polyethylene composites reinforced by organosilane-graphitic nanoplatelets. *Wear*. **309**, 43–51 (2014).

303. C. Backes *et al.*, Production of Highly Monolayer Enriched Dispersions of Liquid-Exfoliated Nanosheets by Liquid Cascade Centrifugation. *ACS Nano*. **10**, 1589–1601 (2016).

304. A. C. Ferrari *et al.*, The Raman Fingerprint of Graphene. *Phys. Rev. Lett.* **97**, 187401 (2006).

305. A. C. Ferrari, D. M. Basko, Raman spectroscopy as a versatile tool for studying the properties of graphene. *Nat. Nanotechnol.* **8**, 235–246 (2013).

306. R. Beams, L. G. Canc, L. Novotny, Raman characterization of defects and dopants in graphene. *J. Phys. Condens. Matter*. **27**, 083002 (2015).

307. A. C. Ferrari, Raman spectroscopy of graphene and graphite: Disorder, electron-phonon coupling, doping and nonadiabatic effects. *Solid State Commun.* **143**, 47–57 (2007).

308. L. Liu, M. Qing, Y. Wang, S. Chen, Defects in Graphene: Generation, Healing, and Their Effects on the Properties of Graphene: A Review. *J. Mater. Sci. Technol.* **31**, 599–606 (2015).

309. A. Rajabpour, S. Kimiagar, F. Tavazoee, Effect of defects on mechanical properties of graphene under shear loading using molecular dynamic simulation. *Phys. Chem. Res.* **3**, 299–304 (2015).

310. N. Jing *et al.*, Effect of defects on Young's modulus of graphene sheets: A molecular dynamics simulation. *RSC Adv.* **2**, 9124–9129 (2012).

311. A. C. Ferrari, J. Robertson, Interpretation of Raman spectra of disordered and amorphous carbon. *Phys. Rev. B*. **61**, 14095–14107 (2000).

312. L. G. Cancado *et al.*, Quantifying defect in graphene via raman at different excitation energies. *Nano Lett.* **11**, 3190–3196 (2011).

313. M. V Bracamonte, G. I. Lacconi, S. E. Urreta, L. E. F. Foa Torres, On the Nature of Defects in Liquid-phase Exfoliated Graphene. *J. Phys. Chem. C*. **118**, 15455–15459 (2014).

314. C. Casiraghi, S. Pisana, K. S. Novoselov, A. K. Geim, A. C. Ferrari, Raman fingerprint of charged impurities in graphene. *Appl. Phys. Lett.* **91**, 2007–2009 (2007).

315. J. M. Englert *et al.*, Soluble graphene: Generation of aqueous graphene solutions aided by a perylenebisimide-based bolaamphiphile. *Adv. Mater.* **21**, 4265–4269 (2009).

316. C. J. Shih *et al.*, Understanding surfactant/graphene interactions using a graphene field effect transistor: Relating molecular structure to hysteresis and carrier mobility. *Langmuir*. **28**, 8579–8586 (2012).

317. S. S. Sukumaran, K. B. Jinesh, K. G. Gopchandran, Liquid phase exfoliated graphene for electronic applications. *Mater.Res.Express.* **4**, 095017 (2017).

318. A. C. Ferrari *et al.*, Raman spectrum of graphene and graphene layers. *Phys. Rev. Lett.* **97**, 1–4 (2006).

319. A. Das, B. Chakraborty, A. K. Sood, Raman spectroscopy of graphene on different substrates and influence of defects. *Bull. Mater. Sci.* **31**, 579–584 (2008).

320. A. E. Del Rio Castillo *et al.*, High-yield production of 2D crystals by wet-jet milling. *Mater. Horizons*. **5**, 890–904 (2018).

321. K. Kouroupis-agalou *et al.*, Fragmentation and exfoliation of 2-dimensional materials: a statistical approach. *Nanoscale*. **6**, 5926–5933 (2014).

322. T. G. Mezger, *The Rheology Handbook: For Users of Rotational and Oscillatory Rheometers* (2006).

323. C. E. Stauffer, The measurement of surface tension by pendant drop method. *J. Phys. Chem.* **69**, 1933–1938 (1965).

324. J. D. Berry, M. J. Neeson, R. R. Dagastine, D. Y. C. Chan, R. F. Tabor, Measurement of surface and interfacial tension using pendant drop tensiometry. *J. Colloid Interface Sci.* **454**, 226–237 (2015).

325. B. Sharma, S. Shekhar, P. Malik, P. Jain, Study of mechanism involved in synthesis of graphene oxide and reduced graphene oxide from graphene nanoplatelets. *Mater. Res. Express*. **5** (2018), doi:10.1088/2053-1591/aac650.

326. X. Wang *et al.*, In situ polymerization of graphene nanosheets and polyurethane with enhanced mechanical and thermal properties. *J. Mater. Chem.* **21**, 4222–4227 (2011).

327. J. R. Davis, *Tensile Testing, 2nd Edition* (ASM International, 2004).

328. H. Y. Hui, *Handbook of Food Science, Technology and Engineering, Volume 3* (Taylor & Francis, 2006).

329. E. Jiménez, B. Cabañas, G. Lefebvre, *Environment, Energy and Climate Change I: Environmental Chemistry of Pollutants and Wastes* (Springer, 2015).

330. G. Rabilloud, *High-performance Polymers: Chemistry and Applications* (Editions Technip, 1997).

331. U.S. Environmental Protection Agency, *Toxicological review of acetone* (EPA, 2001).

332. M. Crabbe-Mann, D. Tsaoulidis, M. Parhizkar, M. Edirisinghe, Ethyl cellulose, cellulose acetate and carboxymethyl cellulose microstructures prepared using electrohydrodynamics and green solvents. *Cellulose*. **25**, 1687–1703 (2018).

333. A. Arostegui, M. Sarrionandia, J. Aurrekoetxea, I. Urrutibeascoa, Effect of dissolution-based recycling on the degradation and the mechanical properties of acrylonitrile-butadiene-styrene copolymer. *Polym. Degrad. Stab.* **91**, 2768–2774 (2006).

334. P. Slobodian, A. Lenganova, P. Saha, M. Slouf, Poly(methyl methacrylate)/Multi-wall Carbon Nanotubes Composites Prepared by Solvent Cast Technique: Composites Electrical Percolation Threshold. *J. Reinf. Plast. Compos.* **26**, 1705–1712 (2007).

335. A. E. Del Río Castillo, C. D. Reyes-Vazquez, L. E. Rojas-Martinez, V. Pellegrini, F. Bonaccorso, Single-step exfoliation and functionalization of few-layers black phosphorus and its application for polymer composites. *FlatChem*. **18**, 100131 (2019).

336. J. Xie, H. Ye, Q. Zhang, L. Li, M. Jiang, Studies on polymer blends with moderate specific interactions. 2. Phase structure of blends SAN/TPU and SAN/TPU/EVA. *Polym. Int.* **44**, 35–40 (1997).

337. S. Sankaranarayanan, J. Hermosilla, F. Acevedo, R. Navia, The influences of solvents on the electrospun of whole Scenedesmus almeriensis and poly (ethylene oxide) for the preparation of composite nano fi bers. *Compos. Commun.* **10**, 18–24 (2018).

338. A. V. Puga, R. Garcia-Valls, S. Fernández-Prieto, J. Smets, D. York, Dual xanthan gum/poly(vinyl acetate) or alkyl-functionalized poly(vinyl alcohol) films as models for advanced coatings. *J. Appl. Polym. Sci.* **131**, 40870 (2014).

339. S. Yano, K. Nakamura, M. Kodomari, N. Yamauchi, Preparation and Properties of Poly (vinyl acetate)/Silica-Gel Microhybrids. *J. Appl. Polym. Sci.* **54**, 163–176 (1994).

340. P. May, U. Khan, J. M. Hughes, J. N. Coleman, Role of solubility parameters in understanding the steric stabilization of exfoliated two-dimensional nanosheets by adsorbed polymers. *J. Phys. Chem. C.* **116**, 11393–11400 (2012).

341. A. S. Wajid *et al.*, Polymer-stabilized graphene dispersions at high concentrations in organic solvents for nanocomposite production. *Carbon*. **50**, 526–534 (2012).

342. M. T. Popescu *et al.*, Colloidal stabilization of graphene sheets by ionizable amphiphilic block copolymers in various media. *RSC Adv.* **5**, 89447–89460 (2015).

343. Arkema, www.arkema.com.

344. D. G. Poitout, *Biomechanics and Biomaterials in Orthopedics* (Springer-Verlag London, 2016).

345. A. Paydayesh, A. Arefazar, A. Jalaliarani, A morphological study on the migration and selective localization of graphene in the PLA/PMMA blends. *J. Appl. Polym. Sci.* **133**, 43799 (2016).

346. S. K. Swain, G. Prusty, A. S. Ray, L. Behera, Dispersion of nanoplatelets of graphite on PMMA matrix by in situ polymerisation technique. *J. Exp. Nanosci.* **9**, 240–248 (2014).

347. S. Mohamadi, N. Sharifi-sanjani, A. Foyouhi, Evaluation of graphene nanosheets influence on the physical properties of PVDF/PMMA blend. *J. Polym. Res.* **20**, 46 (2013).

348. N. Belhaneche-Bensemra, B. Belaabed, A. Bedda, Study of the miscibility and the thermal degradation of PVC/PMMA blends. *Macromol. Symp.* **180**, 203–215 (2002).

349. M. M. Abutalib, Insights into the structural , optical , thermal , dielectric , and electrical properties of PMMA / PANI loaded with graphene oxide nanoparticles. *Phys. B (Amsterdam, Neth.)*. **552**, 19–29 (2019).

350. S. Jabeen, S. Gul, A. Kausar, B. Muhammad, F. Muhammad, An Innovative Approach to the Synthesis of PMMA/PEG/Nanobifiller Filled Nanocomposites with Enhanced Mechanical and Thermal Properties. *Polym. Plast. Technol. Eng.* **58**, 427–442 (2018).

351. I. A. Disher Al-Hydary, L. M. Manocha, P. M. George, Preparation and characterization of PMMA-ABS blend. *IQJMME*. **12**, 709–722 (2012).

352. B. K. Kim, G. S. Shin, Y. J. Kim, T. S. Park, Miscible and Immiscible Blends of ABS with PMMA . II . Mechanical and Surface Properties. *J. Appl. Polym. Sci.* **47**, 1581–1587 (1993).

353. J. A. Pathak, R. H. Colby, S. Y. Kamath, S. K. Kumar, R. Stadler, Rheology of Miscible Blends : SAN and PMMA. *Macromolecules*. **31**, 8988–8997 (1998).

354. G. N. Kumaraswamy, C. Ranganathaiah, M. V Deepa Urs, H. B. Ravikumar, Miscibility and phase separation in SAN / PMMA blends investigated by positron lifetime measurements. *Eur. Polym. J.* **42**, 2655–2666 (2006).

355. N. T. Qazvini, E. Chehrazi, Glass Transition Behavior and Dynamic Fragility of PMMA-SAN Miscible Blend. *J. Macromol. Sci., Part B Phys.* **50**, 2165–2177 (2011).

356. K. Naito, G. E. Johnson, D. L. Allara, T. K. Kwei, Compatibility in Blends of Poly (methyl

methacrylate) and Poly (styrene-co-acrylonitrile).1.Physical Properties. *Macromolecules*. **11**, 1260–1265 (1978).

357. A. Paydayesh, A. A. Azar, A. J. Arani, A. Kabir, M. Campus, Investigation on the effect of Graphene on The Morphology , Mechanical and Thermal properties of PLA/PMMA Blends. *Ciência e Nat.* **37**, 15–22 (2015).

358. P. Lin, J. Wu, W. Liu, Green and facile synthesis of few- layer graphene via liquid exfoliation process for Lithium-ion batteries. *Sci. Rep.* **8**, 9766 (2018).

359. A. Reina *et al.*, Large Area , Few-Layer Graphene Films on Arbitrary Substrates by Chemical Vapor Deposition. *Nano Lett.* **9**, 30–35 (2009).

360. A. Gupta, G. Chen, P. Joshi, S. Tadigadapa, P. C. Eklund, Raman scattering from high-frequency phonons in supported n-graphene layer films. *Nano Lett.* **6**, 2667–2673 (2006).

361. Y. K. Koh, M. Bae, D. G. Cahill, E. Pop, Reliably Counting Atomic Planes of Few-Layer Graphene (n > 4). *ACS Nano*. **5**, 269–274 (2011).

362. H. Sanaeepur *et al.*, A novel acrylonitrile-butadiene-styrene/poly(ethylene glycol) membrane: Preparation, characterization, and gas permeation study. *Polym. Adv. Technol.* **23**, 1207–1218 (2011).

363. J. Y. Shur, B. Ranby, Gas Permeation of Polymer Blends. IV. Poly(vinyl Chloride) (PVC)/Acrylonitrile-Butadiene-Styrene (ABS) Terpolymer. *J. Appl. Polym. Sci.* **20**, 3121–3131 (1976).

364. H. Sanaeepur, A. E. Amooghin, A. Moghadassi, A. Kargari, Preparation and characterization of acrylonitrile–butadiene–styrene/poly(vinyl acetate) membrane for CO2 removal. *Sep. Purif. Technol.* **80**, 499–508 (2011).

365. W. J. Work, K. Horie, M. Hess, R. F. T. Stepto, W. J. Work, Definitions of terms related to polymer blends , composites , and multiphase polymeric materials. *Pure Appl. Chem.* **76**, 1985–2007 (2004).

366. S. Dul, A. Pegoretti, L. Fambri, Effects of the Nanofillers on Physical Properties of Acrylonitrile-Butadiene-Styrene Nanocomposites: Comparison of Graphene Nanoplatelets and Multiwall Carbon Nanotubes. *Nanomaterials*. **8**, 674 (2018).

367. Q. Waheed, A. N. Khan, R. Jan, Investigating the reinforcement effect of few layer graphene and multi-walled carbon nanotubes in acrylonitrile-butadiene-styrene. *Polymer*. **97**, 496–503 (2016).

368. C. Heo, M. Hyun-Gon, Y. Choon Sup, C. Jin-Hae, ABS Nanocomposite Films Based on Functionalized-Graphene Sheets. *J. Appl. Polym. Sci.* **124**, 4663–4670 (2012).

369. L. Poláková *et al.*, Poly(meth)acrylate nanocomposite membranes containing in situ exfoliated graphene platelets: Synthesis, characterization and gas barrier properties. *Eur. Polym. J.* **94**, 431–445 (2017).

370. S. N. Tripathi, G. S. S. Rao, A. B. Mathur, R. Jasra, Polyolefin/graphene nanocomposites: a review. *RSC Adv.* **7**, 23615–23632 (2017).

371. K. Pearson, Note on Regression and Inheritance in the Case of Two Parents. *Proc. R. Soc. London*. **58**, 240–242 (1895).

372. H. L. Cox, The elasticity and strength of paper and other fibrous materials. *Br. J. Appl. Phys.* **3**, 72–79 (1952).

373. S. Ahmed, F. R. Jones, A review of particulate reinforcement theories for polymer composites. *J. Mater. Sci.* **25** (1990), pp. 4933–4942.

374. R. M. Jones, *Mechanics of composite materials* (Taylor & Francis, 1998).

375. P. May, U. Khan, A. O'Neill, J. N. Coleman, Approaching the theoretical limit for reinforcing polymers with graphene. *J. Mater. Chem.* **22**, 1278–1282 (2012).

376. I. B. Page, *Polyamides as Engineering Thermoplastic Materials* (2000).

377. A. E. Del Rio Castillo *et al.*, *Mater. Horizons*, in press, doi:10.1039/C8MH00487K.

378. T. Swan, https://thomas-swan.co.uk/chemical_products/elicarb/.

379. Avanzare, http://www.avanzarematerials.com/divisions/graphene/.

380. Nanesa, http://nanesa.com/.

381. G. Supermarket, https://graphene-supermarket.com/.

382. X. Science, https://xgsciences.com/.

383. Versarien, https://www.nanene.com/.

384. X. Fu, Y. Liu, X. Zhao, D. Zhao, G. Yang, A commercial production route to prepare polymer-based nanocomposites by unmodified multilayer graphene. *J. Appl. Polym. Sci.* **132**, 1–12 (2015).

385. C. Li, M. Xiang, L. Ye, Intercalation structure and highly enhancing tribological performance of monomer casting nylon-6/graphene nano-composites. *Compos. Part A*. **95**, 274–285 (2017).

386. X. Fu *et al.*, A facile route to prepare few-layer graphene/ polyamide 6 nanocomposites by liquid reactive extrusion. *RSC Adv.* **5**, 77316–77323 (2015).

387. B. Mayoral *et al.*, Melt processing and characterisation of polyamide 6/graphene nanoplatelet composites. *RSC Adv.* **5**, 52395–52409 (2015).

388. P. Wei, S. Cui, S. Bai, In situ exfoliation of graphite in solid phase for fabrication of graphene/polyamide-6 composites. *Compos. Sci. Technol.* **153**, 151–159 (2017).

389. Z. Liu, J. Shi, Y. Wang, in *13th International Manufacturing Science and Engineering Conference* (2018), pp. 1–8.

390. L. Mészáros, J. Szakács, in *NANOCON 2013 - Conference Proceedings, 5th International Conference* (2013), pp. 9–13.

391. S. H. Hwang *et al.*, Effects of process parameters and surface treatments of graphene nanoplatelets on the crystallinity and thermomechanical properties of polyamide 6 composite fibers. *Compos. Part B Eng.* **100**, 220–227 (2016).

392. M. Kim *et al.*, Modeling, processing, and characterization of exfoliated graphite nanoplatelet-nylon 6 composite fibers. *Compos. Part B Eng.* **66**, 511–517 (2014).

393. X. Fu, Y. Liu, X. Zhao, D. Zhao, G. Yang, A commercial production route to prepare polymer-based nanocomposites by unmodified multilayer graphene. *J. Appl. Polym. Sci.* **132** (2015), doi:10.1002/app.42742.

394. X. Fu *et al.*, A facile route to prepare few-layer graphene/ polyamide 6 nanocomposites by liquid reactive extrusion. *RSC Adv.* **5**, 77316–77323 (2015).

395. X. Feng, S. Kwon, J. Y. Park, M. Salmeron, Superlubric sliding of graphene nanoflakes on graphene. *ACS Nano*. **7**, 1718–1724 (2013).

396. F. Wang, J. Mao, Double layer aligned-graphene nanosheets/styrene-butadiene rubber composites:Tribological and mechanical properties. *Appl. Polym. Sci.* **136**, 46939 (2019).

397. Avraham H., *Bearing design in machinery: engineering tribology and lubrication* (2002).

398. W. Yu, H.-Q. Xie, L.-F. Chen, X.-F. Zhou, Graphene nanoplatelets/nylon 6 composites with high thermal conductivity. *J. Eng. Thermophys.* **34**, 1749–1751 (2013).

399. B. Xu, Z. Lin, J. Chen, J. Lin, Preparation and Characterization of GNP/nylon composites. *Appl. Mech. Mater.* **556**, 339–342 (2014).

400. X. Cui *et al.*, Thermal Conductive and Mechanical Properties of Polymeric Composites Based on Solution-Exfoliated Boron Nitride and Graphene Nanosheets: A Morphology-Promoted Synergistic Effect. *ACS Appl. Mater. Interfaces*. **7**, 19068–19075 (2015).

401. N. Song, J. Yang, P. Ding, S. Tang, L. Shi, Effect of polymer modifier chain length on thermal conductive property of polyamide 6/graphene nanocomposites. *Compos. Part A Appl. Sci. Manuf.* **73**, 232–241 (2015).

402. K. E. Kear, *Developments in Thermoplastic Elastomers* (iSmithers., 2003).

403. J. G. Drobny, *Handbook of thermoplastic elastomers* (2014).

404. U. Khan, P. May, A. O'Neill, J. N. Coleman, Development of stiff, strong, yet tough composites by the addition of solvent exfoliated graphene to polyurethane. *Carbon*. **48**, 4035–4041 (2010).

405. M. Liu *et al.*, Micromechanics of reinforcement of a graphene-based thermoplastic elastomer nanocomposite. *Compos. Part A Appl. Sci. Manuf.* **110**, 84–92 (2018).

406. M. Haghnegahdar, G. Naderi, M. H. R. Ghoreishy, Electrical and thermal properties of a thermoplastic elastomer nanocomposite based on polypropylene/ethylene propylene diene monomer/graphene. *Soft Mater.* **15**, 82–94 (2017).

407. S. Azizi, E. David, M. F. Fréchette, P. Nguyen-Tri, C. M. Ouellet-Plamondon, Electrical and thermal conductivity of ethylene vinyl acetate composite with graphene and carbon black filler. *Polym. Test.* **72**, 24–31 (2018).

408. D. Pierleoni *et al.*, Selective Gas Permeation in Graphene Oxide-Polymer Self-Assembled Multilayers. *ACS Appl. Mater. Interfaces*. **10**, 11242–11250 (2018).

409. D. Pierleoni *et al.*, Graphene-based coatings on polymer films for gas barrier applications. *Carbon*. **96**, 503–512 (2016).

410. M. Soheilmoghaddam *et al.*, Development of Ethylene-Vinyl Acetate Composites Reinforced with Graphene Platelets. *Macromol. Mater. Eng.* **302** (2017),

doi:10.1002/mame.201600260.

411. K. Hong *et al.*, Mechanical and piezo-resistive properties of styrene–butadiene–styrene copolymer covalently modified with graphene/styrene–butadiene–styrene composites. *J. Appl. Polym. Sci.* **135**, 1–11 (2018).